Technische Universität München
Lehrstuhl für Technische Physik

Y-Substituted Barium Zirconate, a Proton Conducting Electrolyte for Applications at Intermediate Temperatures

Sophie Duval

Vollständiger Abdruck der von der Fakultät für Chemie der Technischen Universität München zur Erlangung des akademischen Grades eines

Doktors der Naturwissenschaften (Dr. rer. nat.)

genehmigten Dissertation.

Vorsitzender: Univ.-Prof. Dr. Th. Fässler
Prüfer der Dissertation:
1. Univ.-Prof. Dr. U. Stimming
2. Univ.-Prof. Dr. R. Niewa

Die Dissertation wurde am 13.03.2008 bei der Technischen Universität München eingereicht und durch die Fakultät für Chemie am 30.06.2008 genommen.

Summary

Materials with high and pure proton conductivities are candidates for electrolytes in sensors, batteries, fuel cells, and electrolysers. The typical proton conductors developed a couple of decades ago were mainly acidic or hydrous inorganic compounds. Later, entirely different classes of materials gained increasing interest as proton conductors such as: polymers, oxide ceramics, and intercalation compounds. Ceramics, particularly perovskites, have shown potential advantages in terms of operating temperature, mechanical strength, chemical, thermal and physical stability.

$BaZr_{0.9}Y_{0.1}O_{3-\delta}$ (BZY10) appears to be a promising electrolyte, since it was recently demonstrated that this material was both a thermodynamically stable material and a fast proton conductor (conductivity $\geq 10^{-2}$ S.cm^{-1} at 400°C). However, experimental so far results show obvious discrepancies and a very low total conductivity (**chapter 1**).

In order to better understand these features, the present thesis focuses on processing and charactering of BZY10 prepared by different synthesis routes, sintering/annealing temperatures, and by the addition of small amounts of metal ions.

Techniques and instruments required for the characterisation of BZY10 are described in **chapter 2**.

A comprehensive characterisation (e.g. microstructure, crystallography and electrochemistry) of BZY10 prepared by the conventional solid-state reaction method is given in **chapter 3**. The results from impedance spectroscopy measurements showed that if the grain interior (also called bulk) is highly conductive, the grain boundaries are highly resistive and limit the overall conductivity.

Some parameters of the synthesis and the sintering were systematically varied in the following chapters. First, the influence of different synthesis routes using different precursors was studied in **chapter 4**. In addition to the conventional solid-state reaction route from chapter 3, BZY10 was prepared by spray drying and spray pyrolysis. The resulting pellets had various grain sizes and porosities. However, the microstructure was not found to be the major factor influencing the bulk conductivity. Instead, the crystallographic properties were correlated with the electrical properties: the bigger the lattice parameter, the lower the activation energy. The second modification of the synthesis is presented in **chapter 5** and consisted of adding metal

ions to BZY10 prepared by the standard solid-state reaction method. TiO_2, MgO, Al_2O_3, Mo and Bi_2O_3 were introduced in small quantities in BZY10 powder. The conductivities of the bulk and the grain boundaries were decreased by these additions. The correlation between the lattice parameter and the activation energy, pointed out in chapter 4, was verified.

The influence of a high sintering temperature on the electrical properties is shown in **chapter 6**. BZY10 was prepared by the standard solid-state reaction method and annealed at ~ 2200°C in an optical floating zone furnace. Grain boundary conductivity increased of about 2 orders of magnitude after annealing, whereas the bulk conductivity remained unchanged.

Finally, the overall results on transport properties are discussed in **chapter 7**. A summary, conclusions and strategies for further research are proposed in **chapter 8**.

Zusammenfassung

Materialien hoher Protonenleitfähigkeit finden Einsatzmöglichkeiten in Sensoren, Batterien, Brennstoffzellen und Elektrolyseuren. Heute werden dafür hauptsächlich Protonenleiter auf Grundlage basisch und sauer reagierender anorganischer Verbindungen verwendet, die bereits vor Jahrzehnten entwickelt wurden. Erst relativ spät rückte eine vollständig andere Materialklasse in den Mittelpunkt des Interesses: Oxidkeramiken und Interkalationsverbindungen. Keramiken, insbesondere Metalloxide wie Perowskite, erweisen sich als vorteilhaft hinsichtlich der Betriebstemperaturen, ihrer mechanischen Belastbarkeit, physikalisch-chemischer Eigenschaften und Temperaturbeständigkeit. $BaZr_{0.9}Y_{0.1}O_{3-\delta}$ (BZY10) ist aufgrund seiner thermodynamischen Stabilität und Protonenleitfähigkeit $\geq 10^{-2}$ S.cm^{-1} bei 400°C ein vielversprechender Elektrolytwerkstoff. Allerdings konnten die erwarteten Leitfähigkeiten experimentell bislang nicht erreicht werden mit teils widersprüchlichen Ergebnissen.

An diesem Punkt setzt die vorliegende Arbeit an und konzentriert sich auf die Verarbeitung und Charakterisierung von BZY10 Elektrolytschichten, die über verschiedene Pulversyntheseverfahren, Wärmebehandlungs- und Sinterschritte und unter Verwendung von Sinterhilfsmitteln hergestellt wurden. Mögliche Zusammenhänge zwischen Mikrostruktur, Kristallographie und Leitfähigkeit werden diskutiert. Die zur Charakterisierung von BZY10 verwendeten experimentellen Verfahren werden in **Kapitel 2** beschrieben.

In **Kapitel 3** werden Mikrostruktur, Kristallographie und die elektrochemische Charakterisierung von BZY10 beschreiben, das über die konventionelle Festoxidreaktion hergestellt wurde. Mit Hilfe der Impedanzspektroskopie wird gezeigt, dass eine hohe Volumenleitfähigkeit im Material vorliegt, die Korngrenzen jedoch hohe Widerstände aufweisen und so die Gesamtleitfähigkeit begrenzen. Volumen- und Korngrenzeneigenschaften werden bei der systematischen Untersuchung von Prozessschritten zur Herstellung der Elektrolyte weiterhin unterschieden.

Zuerst werden in **Kapitel 4** verschiedene Verfahren zur Pulversynthese verglichen und ihr Einfluss auf die Volumeneigenschaften untersucht. Dies sind neben der Festoxidroute die Sprühtrocknung und Sprühpyrolyse, wovon Pulverpresslinge nach

anschliessender Sinterung Proben unterschiedlicher Porositäten und Korngrössen ergaben. Allerdings bestimmen diese Struktureigenschaften nur unwesentlich die Leitfähigkeit der verschiedenen Proben. Als wesentlicher Einflussparameter für die Volumenleitfähigkeit wurde der interatomare Abstand im BZY10 Kristallgitter identifiziert: je grösser der Gitterparameter, desto geringer ist die Aktivierungsenergie für den Protonentransport.

In einem zweiten Schritt wurde der Einfluss von Metallelementen zur Verbesserung der Sinterung (Sinterhilfsmittel) untersucht (**Kapitel 5**). TiO_2, MgO, Al_2O_3, Mo und Bi_2O_3 wurden in geringen Mengen (einige %) BZY10 –Pulver zugegeben. Dies führt zu einer generellen Verringerung der Leitfähigkeit, was sowohl für das Volumen als auch für die Korngrenzen gilt. Die Volumenleitfähigkeit konnte hier wiederum mit einer Verkleinerung des Gitterparameters (wie schon in Kapitel 4 beschrieben) korreliert werden.

Desweiteren wurde die Korngrenzenleitfähigkeit untersucht. **Kapitel 6** beschriebt den Einfluss hoher Sintertemperaturen auf die Leitfähigkeit. BZY10, das über die Festoxidroute hergestellt wurde, konnte mit Hilfe des Zonenschmelzverfahren bei Temperaturen von ~ 2200°C (wie auch für Einkristalle angewandt) weiter verdichtet werden. Dadurch erhöht sich die Korngrenzenleitfähigkeit um bis zu zwei Grössenordnungen, nicht jedoch die Volumenleitfähigkeit.

Die Ergebnisse werden in **Kapitel 7** abschiessend diskutiert. **Kapitel 8** fasst die Schlussfolgerungen und offene wiss. Fragestellungen in einem Ausblick zusammen.

Résumé

Les matériaux conducteurs du proton (valeurs de la conductivité supérieures à 10^{-2} S.cm^{-1} à 400°C) sont utilisés comme électrolytes pour des capteurs, batteries, piles à combustible, électrolyseurs, et autres convertisseurs d'énergie électrochimique. Les premiers électrolytes développés il y a quelques années étaient des composés inorganiques ayant des fonctions acides. Plus récemment, d'autres classes de matériaux ont suscité l'intérêt : les polymères, les céramiques, et les composés d'intercalation. Les céramiques, en particulier les perovskites, présentent des avantages en terme de stabilité thermique, mécanique, et thermodynamique.

Le zirconate de baryum substitué par de l'yttrium est apparu comme un candidat intéressant, car il a été montré récemment grâce à des considérations théoriques que ce matériau devrait être stable thermodynamiquement et présenter une bonne conductivité du proton. Or jusqu'à présent, les résultats expérimentaux diffèrent considérablement et les valeurs de la conductivité totale de $BaZr_{0.9}Y_{0.1}O_{3-\delta}$ (BZY10) sont très basses (**chapitre 1**). Afin de préparer un matériau performant, nos recherches se sont concentrées sur l'étude des paramètres qui fonctionnalisent BZY10 ainsi que sur la compréhension des propriétés physico-chimiques fondamentales et des mécanismes de transport ionique dans ce matériau.

Le **chapitre 2** présente les techniques de caractérisation utilisées pendant le travail de thèse.

Puis, le **chapitre 3** décrit les caractéristiques générales comme la microstructure, la cristallographie et l'électrochimie de BZY10 préparé par la méthode standard de réaction à l´état solide. En particulier, il est montré par spectroscopie d'impédance que si l'intérieur du grain (aussi appelé bulk) est conducteur, les joints de grains sont particulièrement résistifs et limitent la conductivité totale.

La nature des précurseurs, la température de calcination et de frittage, ainsi que l'atmosphère de synthèse sont autant de paramètres qui affectent les caractéristiques cristallographiques, microstructurales et électriques du matériau. Par conséquent, la variation de certains de ces paramètres est étudiée de manière systématique dans les chapitres qui suivent.

L´influence de la méthode de synthèse et des précurseurs est étudiée dans le **chapitre 4**. Ainsi, BZY10 est préparé par la méthode de réaction à l´état solide, de

séchage (spray drying) et de pyrolyse (spray pyrolysis) par pulvérisation. Différentes tailles de grains et de pores sont obtenus, mais il apparaît qu´elles n´influencent pas particulièrement la conductivité. Par contre, les propriétés cristallographiques ont pu être corrélées avec les propriétés électriques : plus le paramètre de maille est grand, plus l´énergie d´activation est faible.

Le **chapitre 5** présente l´influence d´impuretés métalliques intentionnellement ajoutées à BZY10. La corrélation entre le paramètre de maille et l´énergie d´activation est aussi vérifiée dans ce chapitre.

Le **chapitre 6** présente l´influence d´une très haute température de frittage. BZY10 préparé par la méthode de réaction à l´état solide est recuit à ~ 2200°C dans un four optique à zone flottante. La conductivité des joints de grains de l´échantillon recuit est améliorée de deux ordres de grandeur, alors que la conductivité du bulk reste inchangée.

Si de manière générale, le mécanisme de conduction du proton est globalement connu, ces investigations n´ont jamais porté sur BZY10. Dans le **chapitre 7**, le mécanisme de transport du proton est discuté en fonction des résultats des différents chapitres.

Pour finir, les résultats sont résumés dans le **chapitre 8**. Différentes pistes de recherches et stratégies d´optimisation des performances BZY10 et des conducteurs du proton sont présentées.

Table of Contents

Foreword and Acknowledgements

This work was performed at Empa – Swiss Federal Laboratories for Material Testing and Research - at the Laboratory for High Performance Ceramics in Dübendorf (CH) in the period February 2004 to April 2007. The financial support of the Swiss Federal Office of Energy is gratefully acknowledged.

Turning backwards 3 years ago, I had to face the sensitive question: "to be or not to be a Ph.D student". Strongly willing to continue with science, I was also obsessed by the cliché of the Ph.D student hidden behind fake barriers: thick glasses and heavy books, just for being cut off from the reality of the epicurien life! Nevertheless I was curious about it and went further with my investigations on this outgoing way-of-life… What a better place than acknowledgments of thesis to poll the atmosphere! After a state-of-the-art, I found acknowledgements, which precisely disproved my cliché! Feeling more confident then, I was ready to jump into the Ph.D adventure! During my Ph.D, I met by chance the author of these decisive acknowledgements. He had not to argue further to convince me: I am happy to admit that the real life among Ph.D students was diametrically opposite to this cliché. Now at the end of my Ph.D, words fall short as I extend my acknowledgements to all people who make me feel fortunate for where I stand today.

The work was directed by *Prof. Dr. Ulrich Stimming*. He is acknowledged for giving me the freedom to perform this work. I thank *Prof. Dr. Niewa* for accepting to review this work as well as *Prof. Dr. Fässler* for chairing the Ph.D defense.
My sincere thanks go to *Dr. Thomas Graule*, who enabled me to join the Laboratory for High Performance Ceramics and who reminds me about the chemical point of view of every feature!
I kindly thank *Dr. Peter Holtappels* for supervising this work and for having essential scientific inputs. I appreciated much his good advises and his spirit of optimism on me!
I warmly thank *Dr. Ulrich Vogt* for supervising the material processing part of this work and always adding fresh perspective with an unconditional generous support.

Part of the work was performed with the assistance, the knowledge and the equipment of other groups. In this respect, I would like to thank *Prof. Truls Norby*, University Oslo (NO), for teaching me about impedance measurements, *Dr. Fanni Juranyi, Dr Jan Embs* and *Dr Thierry Strässle*, PSI (CH), for QENS measurement, *Dr. Kazimierz Conder* and *Dr. Ekaterina Pomjakushina*, PSI (CH), for the annealing by optical floating zone, and *Dr. Guilhem Dezanneau*, Ecole Centrale Paris (F), for high pressure compaction.

My thanks go to:

- *Defne Bayraktar*, *Jörg Richter*, and *Peter Ried*, as the "co-fuel cells" Ph.D students, for the friendship atmosphere and their kind help in the lab and in the office!
- *Dr.'s Artur Braun*, *Christian Soltmann*, *Joseph Sfeir*, and *Markus Wegmann* for their expertise in physics and QENS measurements, crystallography, fuel cells, and $BaTiO_3$, respectively and for their advice about the Ph.D in general always given without reserve and without sparing humour.
- *Dr. Juliane Heiber* for the XRD measurements.
- *Brigitte Schatzmann*, *Hansjürgen Schindler, Maik Thuenemann*, and *Roland Bächtold* for helping me any time and always finding the best solutions.
- *Dr. Gurdial Blugan* for boosting my written English in sensitive situations.
- *Dr. Andri Vital*, that the chance made me identify more than 1 ½ years after the start of my Ph.D as the author of the so special acknowledgments mentioned above! I appreciated his support about processing and his jokes!
- *Salvatore Fuso* for its contagious enthusiasm organizing our french/german lunches on Thursday.
- My past and present officemates: *Elisabeth Barna* and *Srdan Vasic*, who were the pillar of the KE013 for the 3 last years, but also *Marc Delporte*, *Tamara Wippich*, *Lubomir Hric*, *Jean-Philippe Dellemann* and *Katarzyna Michalow* for the decoration of the room, the good music, the food supply, the telephone jokes, the futile discussions and simply the friendly atmosphere!

Hearty thanks go to the surrounding of my family and friends for their constant and joyful support!

List of Symbols, Abbreviations and Acronyms

A	Electrode area
Å	Ångstrøm, 1 Å = 10^{-10}m
b	Bulk
BET	Brunauer-Emmet-Teller (surface area analysis)
C	Capacitance
D	Diffusion coefficient
E	Energy
e	Elementary charge, 1 e = 1.60219x10^{-19} C
Ea	Activation energy
Emf	Electro-motive force
eV	Electron-Volt, 1 eV = 1.60219x10^{-19} J
FWHM	Full Width at Half Maximum
GB	Grain boundary
ħ	Reduced Plank´s constant, ħ = h/2π = 6.58211915x10^{-16} eV.s
IS	Impedance spectroscopy
JCPDS	Joint Committee on Powder Diffraction Standards
K	Reaction constant
k_B	Boltzmann constant, k_B = 1.38066x10^{-23} J.K^{-1}
L	Sample length
MFC	Mass flow controllers
MS	Mass spectroscometry
PEMFC	Polymer Electrolyte Membrane Fuel Cells
px	Partial pressure of gas x
Q	Constant phase element
$\vec{Q}$	Wave vector
QENS	Quasielastic neutron scattering
R	Resistance
SEM	Scanning electron microscopy
SOFC	Solid Oxide Fuel Cell
Sp. b	Specific bulk

Sp. GB	Specific grain boundary
T	Temperature
TEM	Transmission electron microscopy
TGA-DTA	Differential thermo-analysis
XRD	X-ray diffraction
Z'	Real
Z''	Imaginary
ε	Dielectric constant
ε_0	Dielectric constant of the vacuum, $\varepsilon_0 = 8.85419 \times 10^{-12}\ J^{-1}.C^2.m^{-1}$
λ	Wavelength
μ	Mobility
ν	Stretching frequency
ρ	Density
σ	Conductivity
τ	Transport number
ω	Frequency

CHAPTER 1

About Protons in Oxides

1.1 The promise of solid oxide proton conductors for applications in electrochemical energy conversion devices

With diminishing fossil fuel reserves, energy prices are increasing. Beside financial issues, European countries are concerned about their degree of dependence on imported energy and have to deal with climate associated challenges. In this context, the focus is increasingly shifting towards renewable forms of energy. The hydrogen related technologies are very promising. For these reasons, controlling the production, the storage and the utilisation of hydrogen is a crucial issue.

Steam electrolysers [1, 2], sensors [3], batteries and fuel cells [4] are operating with hygrogen fuel. Since the proton (i.e. hydrogen ion) is small and mobile, materials with high and pure proton conductivity [5, 6] are foreseen as promising electrolytes for these devices. Among proton conducting materials, ceramics have shown potential advantages in terms of operating temperature, mechanical strength, chemical, thermal and physical stability.

An example of taking advantages of using ceramic proton conductor can be easily illustrated for fuel cell applications [4, 7]. The state-of-the-art for fuel cells is dominated by two different technologies [8, 9] (Fig. 1-1): the Solid Oxide Fuel Cells

(SOFC) and the Polymer Electrolyte Membrane Fuel Cells (PEMFC). The first ones are operating at high temperatures (800°C to 1200°C) and the second ones at low temperatures (room temperature to 200°C). Reducing SOFC operating temperatures could increase their lifetime by reducing damaging reactions at the interfaces. It could also make them much less expensive, since metal interconnectors can be used instead of costly ceramic ones. Moreover, SOFC's main advantages, namely speed of electrochemical reactions, use of carbon monoxide as a fuel, possibility of incorporating direct reforming and absence of costly catalysts, would not be undermined at operating temperatures between 600°C and 800°C. On the other hand, increased operating temperatures could increase efficiency and competitiveness of PEMFC systems. Both technologies are therefore gaining grounds towards the targeted intermediate temperature range (400°C - 600°C).

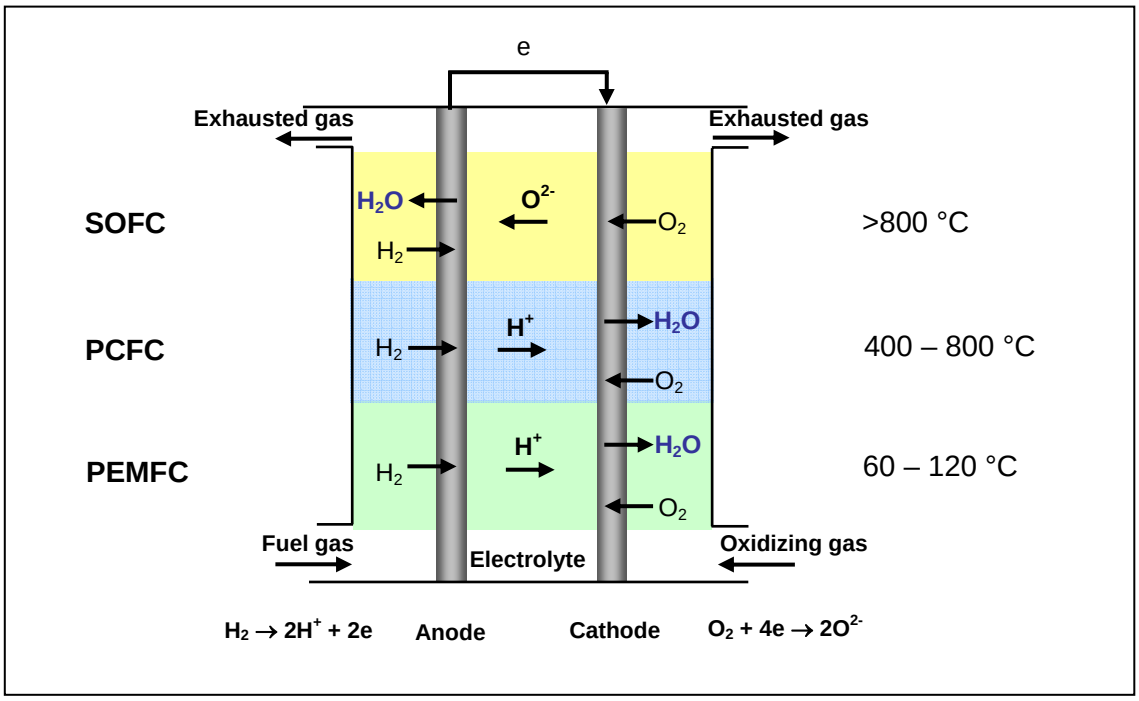

Fig. 1-1 Comparison between the operational principles of SOFC, PCFC and PEMFC.

The major difference between SOFC and PEMFC lies in the nature of the electrolyte as illustrated in Fig. 1-1. SOFC operate with oxide electrolytes, which conduct the oxygen ion, whereas PEMFC use polymer electrolytes, which enable the

proton transport. A rather new fuel cell category based on the proton conducting oxides is called the Proton Conducting Fuel Cells (PCFC). In competition to the intermediate temperature range, the advantages of PCFC [10] over existing technologies are:

- the fuel is not diluted, because water is produced at the cathode, where it can be easily swept away by air,
- ambipolar steam permeation from the cathode to the anode can provide the steam for direct reforming of hydrocarbons, so external steam injection is not required [2]. Therefore, high system efficiency is achieved and coking is not a problem.

Brainstorming on PCFC and on numerous other applications of solid oxide proton conductors has always stimulated researchers. The first one was the French writer Jules Verne, who mentioned the potential of hydrogen as an energy source in his novel "20 000 leagues under the sea" published at the beginning of the 19th century. Nowadays, part of the 6th European Union Research Framework program as well as many projects funded by the Swiss Federal Office of Energy are devoted to research about electrochemical energy conversion devices. More specifically, the interest on solid oxide proton conductors is continuously growing since 25 years, even if only few laboratories are fully committed to research on this topic.

1.2 History of research on solid oxide proton conducting electrolytes

In 1966, Wagner et al. [11] discussed for the first time the existence of protons in CuO, Cu_2O, NiO and in some stabilized zirconias at temperatures above several hundred degrees Celsius in the presence of water vapour. Some years later, Shores et al. [12] reported the proton transport through thoria-based compounds. Several investigations also focused on proton conductivity in SiO_2 and in some hydroxyapatites like $M_{10}(PO_4)_6(OH)_2$ (M = Ca, Sr, Ba, Cd, Pb) [13].

But it is only in the early 80´s that electromotive force (emf) measurements gave the first clear evidence on proton conduction [1]. Iwahara et al. [1] performed these measurements on a new class of proton conductors, namely the substituted

perovskites. A typical perovskite structure of general formula $A^{2+}(B^{4+}_{1-x}B'^{3+}_{x})O_{3-\delta}$ is shown in Fig. 1-2. These materials appeared to be much more promising than previously tested oxides. They show fast proton conduction, up to 10^{-2} S/cm. The best performances are observed between 400°C and 600°C.

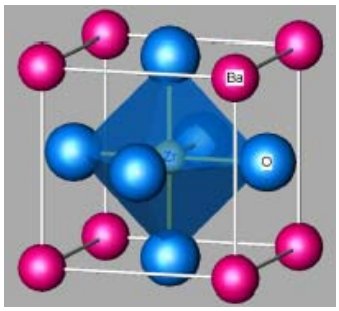

Fig. 1-2 Typical perovskite structure of $BaZrO_3$ (figure reproduced from [14]).

Among them, $BaCe_{0.9}Y_{0.1}O_{3-\delta}$ (BCY10) and $BaZr_{0.9}Y_{0.1}O_{3-\delta}$ (BZY10) are the most studied ones. BCY10 shows the highest proton conductivity observed so far [15]. However, serious concerns about its stability in CO_2 containing atmosphere are emitted [16]. Besides, BZY10 is found to be very stable, but shows a lower conductivity [17].

During the following 10 years, a wide range of substituted perovskites was tested with respect to their ability for proton conduction. Many results stirred up controversy. For instance, conductivity data were found to vary over several orders of magnitude for the same material. In 1995, Iwahara et al. estimated that it was high time to review the progresses and to present the prospects for proton conductors [7]. In particular, they noted the "status quo" of research about proton conductors. The previous studies had provided lots of data, but the remaining open issue was still to understand the reasons for the latent controversial points. Especially, the understanding of proton transport mechanism remains approximate.

In the same year, a new class of proton conductors was discovered by Nowick et al. [18]. This class of proton conductors is called complex or mixed perovskite-related materials. They are of the general formula $A^{2+}_{2}(B'^{3+}_{1+x}B''^{5+}_{1-x})O_{6-\delta}$ and

$A^{2+}_3(B'^{2+}_{1+x}B''^{5+}_{2-x})O_{9-\delta}$. $Ba_3(Ca_{1+x}Nb_{2-x})O_{9-\delta}$ (BCN) is one of the most studied one of this class [19, 20]. For these materials, the protons are not compensated by discrete localized charges like in the simple perovskites, but by a statistical deviation of the number of B′ and B′′ ions from the stoichiometric values. This may avoid the possibility of having immobile O-vacancies or protonic defects, which may happen in a simple perovskite. Additionally, these complex perovskites offer the possibility of ordering B-sites. These investigations boosted again the development on new materials.

1.3 Criteria for the selection of promising solid oxide proton conducting electrolytes

The primary components of an electrochemical device are an electrolyte and two electrodes i.e. a cathode and an anode, as shown schematically in Fig. 1-1. In the simplest example for fuel cell applications, a fuel such as hydrogen is brought into the anode compartment and an oxidant, typically oxygen, into the cathode compartment. Half cell reactions occur at the electrodes. At the cathode, oxygen is reduced. At the anode, hydrogen is oxidized. The potential difference between the half cell reactions is the overall driving force for the oxygen and the hydrogen to react and produce water.
The electrolyte is a central and essential part of the electrochemical cell. For efficient operation, the electrolyte has generally to match the following requirements:

- a high ionic conduction, which allows fast ion diffusion and minimize the cell impedance, and a little or no electronic conduction to minimize the leakage current,
- a high density, in order to be gas tight and serve as gas diffusion barrier,
- a chemical, thermodynamical and mechanical stability in both oxidizing and reducing conditions.

Some criteria derived from previous experiments [21] and from theoretical considerations [21] can be defined to select compositions *a priori*. Except for the stability with acidic gases, which is almost independent of the choice of the A-cation of the perovskite, all relevant properties are superior for an A-site occupation by barium compared to other alkaline earth ions. The choice of the B-cation of the

perovskite requires some compromises. It should be of medium size with an amphoteric nature and should form no significant covalent bonds with its oxygen ligands. High packing densities as a result of small B-cations reduce the water solubility, whereas large B-cations reduce the thermodynamic stability. The occupation of the B-site with different ions of different acid/base properties is expected to further increase the thermodynamic stability. Zirconium and cerium based perovskites substituted by yttrium are the most commonly used materials.

1.4 Defect chemistry of proton conducting electrolytes

1.4.1 Protonic defect formation

Proton conductivity is based on unique properties of the oxide electrolytes. The simple perovskite structures have extrinsic vacancies (e.g. $Ba(Zr_{1-x}Y_x)O_{3-\delta}$). The perovskite structure ABO_3 is substituted by undervalent atoms in the B-site and gives the general formula $AB_{1-x}M_xO_{3-\delta}$ (with A divalent earth alkaline element, B a tetravalent element, and M a trivalent element) - in Kröger Vink notation - according to Eq. 1-1.

$$B_B^x + 1/2\,O_O^x + 1/2\,M_2O_3 \Leftrightarrow M_B^{'} + 1/2\,V_O^{\bullet\bullet} + BO_2 \qquad \text{Eq. 1-1}$$

The substituted perovskite takes protons from water vapour or hydrogen molecules in ambient gas via incorporation of protons by the dissociative absorption of water [22]. In other words, the protons do not originate from host constituents, but the incorporation of the protons occurs via the extrinsic oxygen vacancies [6]. Water from the gas phase dissociates into a hydroxide ion and a proton; the hydroxide ion fills an oxygen ion vacancy, and the proton forms a covalent bond with the oxygen lattice. In the Kröger-Vink notation this reaction is given as Eq. 1-2:

$$H_2O(g) + V_O^{\bullet\bullet} + O_O^x \Leftrightarrow 2OH_O^{\bullet} \qquad \text{Eq. 1-2}$$

where the protonic defects ($OH^{\bullet}$) diffused into the bulk accompanied by the counter diffusion of the oxide ion vacancies ($V_O^{\bullet\bullet}$).

1.4.2 Proton mobility

Two processes can be considered for the transport of protonic defects across the electrolyte [5]. A first mechanism is the "free migration mechanism" or "Grotthus-type mechanism", the proton moves by hopping between stationary host oxygen ions as symbolized by Eq. 1-3:

$$(OH)_O^{\bullet} \cdots O_O^x \Rightarrow O_O^x \cdots (OH)_O^{\bullet} \qquad \text{Eq. 1-3}$$

Another process is the "vehicle mechanism". The proton moves as a passenger on a larger ion like O^{2-} forming OH^- or H_3O^+. Even if the hydrogen pathway in perovskite structures is not understood so far, the proton hopping is often favoured [23].

The proton transfer in oxides is frequently believed to be coupled with the local oxygen dynamics, because of the large distances between nearest neighbour oxygen ions and the strong localisation of the proton within the valence electron density of the oxygen. The proton needs the dynamics of the host oxygen ion sublattice to jump to the neighbouring oxygen ion when the $OH^{\cdots}O$ momentarily is shortened. The elementary mechanism has been described by numerical simulation for barium cerate [24]. As illustrated in Fig. 1-3, the principal features of the transport mechanism are:

- rotational diffusions of the protonic defect,
- proton transfers towards a neighbouring oxide ion i.e. only the protons show long-range diffusion, whereas oxygens reside on their crystallographic positions.

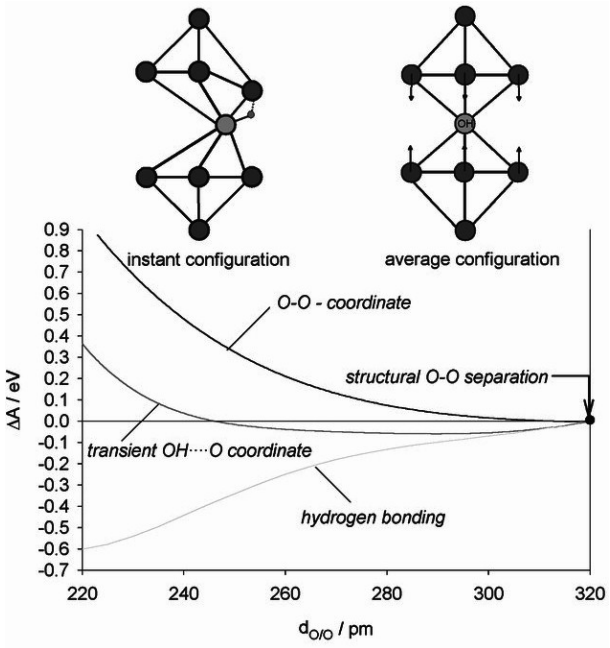

Fig. 1-3 Dynamical hydrogen bonding in $BaCeO_3$. Instant and average configuration; Helmholtz energy difference of the system as a function of the O/O and the OH/O separation (figure reproduced from [24]).

1.4.3 Defect equilibrium

The charge carrier concentration is related to external factors such as temperature, partial pressure and other thermodynamic parameters (i.e. Gibbs energy…) [22, 25].

When proton conduction is dominating, it is apparent from Eq. 1-2, that, under equilibrium conditions, the conductivity, σ, is independent on the partial pressure of oxygen. However, in absence of protons, proton conducting materials can exchange oxygen with the surrounding atmosphere leading to different ionic or electronic contributions to the conductivity.

At high pO_2, the oxygen vacancies can be filled by oxygen producing holes as shown by Eq. 1-4:

$$1/2\,O_2(g) \;+\; V_O^{\bullet\bullet} \;\Leftrightarrow\; O_O^x \;+\; 2h^{\bullet} \qquad \text{Eq. 1-4}$$

which leads to:

$$\sigma \;\approx\; \sigma_{h^{\bullet}} \;\propto\; [V_O^{\bullet\bullet}]p_{O_2}^{1/4} \;\propto\; p_{O_2}^{1/n}$$

with n about 4-6.

At low pO_2, more vacancies are created and electron charge carriers are produced as shown by Eq. 1-5:

$$O_O^x \Leftrightarrow 1/2\,O_2(g) + V_O^{\bullet\bullet} + 2e' \qquad \text{Eq. 1-5}$$

which leads to:

$$\sigma \approx \sigma_{e'} \propto \frac{1}{[V_O^{\bullet\bullet}]p_{O_2}^{1/4}} \propto p_{O_2}^{-1/n}$$

with n as above.

Proton transport can also occur in a hydrogen rich atmosphere in absence of water. The reaction described by Eq. 1-6 would suffice to generate protons:

$$1/2\,H_2(g) + O_O^x \Leftrightarrow OH_O^{\bullet} + e' \qquad \text{Eq. 1-6}$$

1.5 Literature review, aim and approach of the thesis

1.5.1 State-of-the-art of $BaZr_{1-x}Y_xO_{3-\delta}$

Among proton conductors, $BaZr_{0.9}Y_{0.1}O_{3-\delta}$ (BZY10) is one of the most investigated material. Data on the electrical conductivity of BZY10 reported so far are plotted as a function of the inverse temperature in Fig. 1-4. Two interesting features can be observed on this figure.

On the one hand, BZY10 has a low overall proton conductivity [17, 26-29]. Based on data on the formation and the mobility of protonic charge carriers combined with structural information, Kreuer et al. showed in 2001 [30], that the total conductivity of BZY10 is dominated by the resistive grain boundary. Conductivity values of the bulk of BZY10 are even expected to compete with the values for BCY10 [15]. This result was confirmed experimentally shortly after by Schober et al. [25], who measured the grain interior (also called bulk) and the grain boundary contributions separately by impedance spectroscopy. The underlying causes of the blocking grain boundaries remain unclear so far.

On the other hand, Fig. 1-4 highlights discrepancies superior to one order of magnitude in measurements in BZY10 bulk conductivities between the results from Snijkers et al. [31] and Schober et al. [25]. In absence of convincing arguments to explain precisely these discrepancies, the preparation conditions were often pointed out [26, 30-33]. In [31], this is tentatively related to the Ba-content (and the formation of BaO second phase), which depends on the processing method. The processing method (temperature, raw materials…) may influence the amount of $BaCO_3$. This assumption seems to be very important for substituted-barium zirconate regarding that $BaCO_3$ is very volatile and the commonly used solid-state reaction synthesis requires a very high sintering temperature (melting point of $BaZrO_3$ ~ 2600°C (Fig. 1-5)).

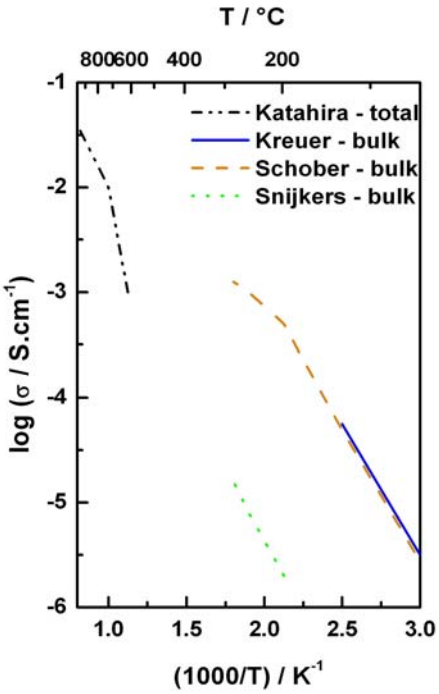

Fig. 1-4 Summary of conductivity measurements for BZY10 in wet atmosphere [31].

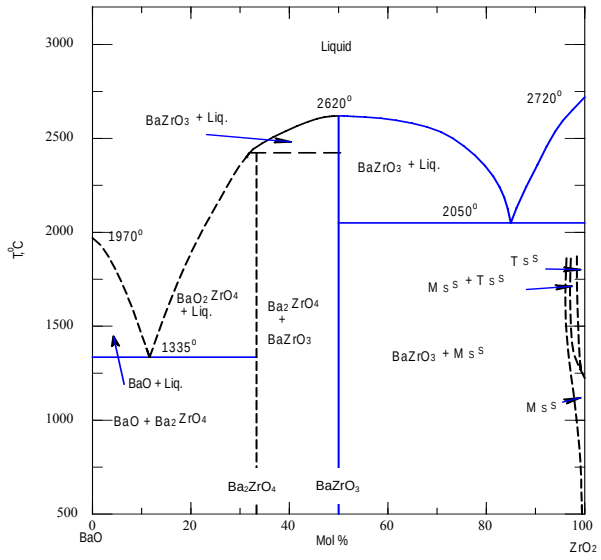

Fig. 1-5 Phase diagram of $BaZrO_3$ [34].

Up to now, the solid-state reaction is the only preparation route which was extensively studied for barium zirconate [35-37]. Moreover many parameters that may control the preparation route (e.g. sintering temperature, use of sintering aids, green body compaction characteristics…) have not been investigated systematically. The spray pyrolysis seems to be an interesting alternative route [38, 39], because this method produces powders with smaller and more reproducible grain sizes compared to the solid-state reaction route. This method is also economical and has a potential for large scale production.

1.5.2 Aim and approach of the thesis

$BaZr_{0.9}Y_{0.1}O_{3-\delta}$ (BZY10) appears to be a very versatile and promising material. The processing has been identified as a crucial step leading to obvious controversies on the material performances. A better correlation of the resulting materials properties, as the microstructure, crystallography and conductivity properties seems to be needed in order to gain a better understanding of the proton conductivity and the proton

transport mechanism. Therefore, this thesis will address the processing and the characterisation of BZY10.

This work is entitled “Y-Substituted Barium Zirconate, an Electrolyte for Applications at Intermediate Temperatures”. After giving the basics for preparation, instruments and methods for characterisation of proton conductors in **chapter 2**, the thesis will focus on $BaZr_{1-x}Y_xO_{3-\delta}$. The investigations are oriented towards 2 main axis discussed over 4 chapters.

The first step aims to prepare Y-substituted barium zirconate in a standard way and to provide the main characteristics (microstructural, crystallographic and electrical) of the powders and the dense specimens. It has become obvious that the investigation of defect phenomena and atomistic diffusion mechanisms underpins the fundamental understanding of the macroscopic behaviour [40]. Since the microstructure and phase of BZY10 have not been entirely investigated either so far [36], the inconsistency in the bulk conductivities from the literature cannot be understood [17, 25, 26, 31]. Therefore, **chapter 3** provides a comprehensive set of data i.e. microstructure, crystallography, and conductivity for yttrium-substituted barium zirconate. The results are compared to the literature values.

The second step of the thesis is to gain a better understanding of the influence of the sample morphology and phase on the conductivity. To achieve this aim, the synthesis of BZY10 was modified by using:

- different synthesis routes in **chapter 4**,
- sintering aids in **chapter 5**,
- an exceptionally high annealing temperature ~ 2200°C in **chapter 6**.

The resulting effect on the conductivity is investigated and analysed independently for the grain interior and the grain boundaries.

A global discussion on mass and charge transport takes place in **chapter 7**. The final **chapter 8** summarizes the main results and conclusions and gives an outlook.

CHAPTER 2

Preparation and Characterisation of $BaZr_{1-x}Y_xO_{3-\delta}$

This chapter gives, first, information about the preparation of ceramic powders and dense specimens. It also describes how the specimens from this work have been prepared.

The second part of this chapter introduces instruments and methods needed to characterise the obtained samples. The applied methods for investigation of microstructural, compositional, thermal and electrical properties are described. Then, the techniques dedicated to operation in humid atmospheres are reported.

2.1 Powder synthesis and further processing

A conventional technique for the synthesis of multicomponent ceramic powders is the solid-state reaction between oxide and/or carbonate precursors. The general preparation consists of mixing and milling the precursors to facilitate the solid-state reaction. The disadvantages of this method are the large grain sizes due to the high firing temperatures and the poor chemical homogeneity [41]. Chemical routes have the potential for achieving improved homogeneity on the crystallite scale. Among these chemical routes, the spray drying and the spray pyrolysis are of special interest. During spray drying, a salt solution is converted into a dry powder. For the pyrolysis, a fuel is added in order to provide the energy required for the decomposition of the salt

solution. As the droplets are burst during the process, these chemical routes allow the production of submicrometer powders.

For all the preparation methods mentioned above a calcination step is required in order to obtain a phase pure material. The obtained desirable phase pure materials are then formed into bars or disks by pressing. The as shaped specimens are further processed. The sintering is a crucial step, which depends on the powder characteristics. Powders with small grain sizes have a higher surface energy and, in consequence, a higher sinter activity. Classically, two different approaches are used additionally to improve the densification: the addition of metal ions, so called sintering aids, and the high pressure compaction.

All the previously described methods lead to polycrystalline materials. Since grain boundaries can have significant effects on the physical and electrical properties of a material, single crystals are of special interest to study the bulk properties. The Czochralski method is a common way to process single crystals. This method is based on the controlled re-crystallisation of a melted "seed crystal". In order to grow a single crystal with this method, an optical floating zone furnace can be used, for instance. This method has become a preferred growth method for various classes of oxides and intermetallics, especially for those showing extreme melt reactivity and high melting temperatures. Commercial facilities use ellipsoid mirrors for focusing of the light emitted from halogen or xenon lamps. A radiation source is located in one focal point of the ellipsoid of revolution, and the molten zone in the other focal point.

In the present work, the solid-state method is considered as a standard method. The specimens obtained using a spray pyrolysis, spray drying, zone annealing and solid-state reaction method with addition of minor elements are compared to the ones prepared by the solid-state reaction method. Table 2-1 summarizes the sample name code used in the different chapters. The methods are described in more details in the following and are sketched in Fig. 2-1.

Table 2-1 Sample name code.

Modification	Sample name code	Chapter n°
Synthesis protocol	Method followed by the sintering temperature e.g. SS1720	4
High annealing temperature by optical floating zone	ZA2200	6
Addition of minor element	[+ Element]	5
High pressure compaction	BZY10 (pressure)	3
Variation of the Y content ($BaZr_{1-x}Y_xO_{3-\delta}$ with x=0, 0.5, 0.10, 0.15, 0.20)	BZYx with x=0, 5, 10, 15, 20	3

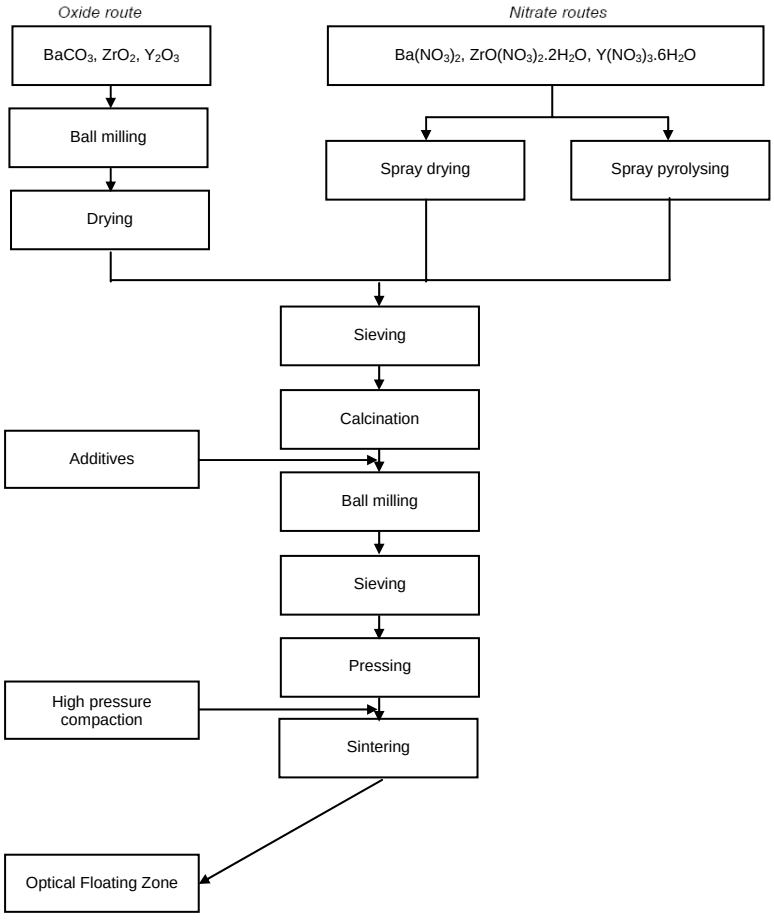

Fig. 2-1 Protocol scheme of the different synthesis routes.

2.1.1 Solid-state reaction method

$BaZr_{1-x}Y_xO_{3-\delta}$ with x = 0, 5, 10, 15, 20 (henceforth known as BZYx) was prepared by the solid-state reaction method (SS) as described below.

The oxide precursors are barium carbonate, $BaCO_3$ (Fluka, purity: 99%), zirconium dioxide, ZrO_2 (Tosoh, purity: 99.9%) and yttrium oxide, Y_2O_3 (Stanford Materials, purity: 99.9%). In order to obtain an exact stoichiometry, the adsorbed water has to be removed. For this purpose, the precursors are dried in a drying cupboard at 290°C. Fig. 2-2 shows that no further mass loss occurs after 1.5 hours of drying i.e. all the adsorbed water is removed and the precursors are dried. The precursors were dried for 3 hours at 290°C for the following experiments.

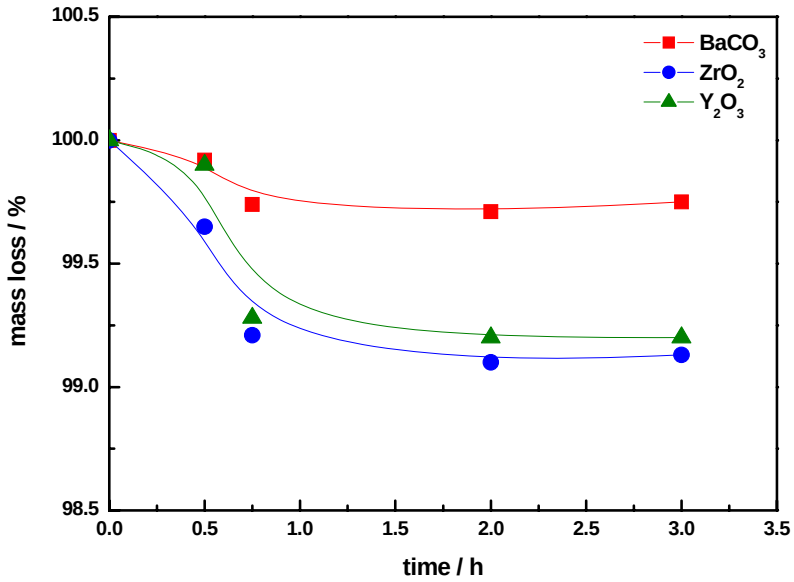

Fig. 2-2 Mass loss of barium carbonate, zirconium dioxide and yttrium oxide versus time in the drying cupboard at 290°C. The mass loss corresponds to the evaporation of the adsorbed water.

After 15 min cooling at room temperature, stoichiometric amounts of each dried precursors were weighted. Then, they were mixed and ball milled in isopropanol with ZrO_2 balls of 3 mm diameter. The balls were removed and the powder was then dried

at 70°C and calcined at 1200°C for 10 hours. Table 2-2 shows that the main mass loss occurs during calcination. This mass loss corresponds within the experimental uncertainty to the mass loss as expected from the reaction.

It is important that carbonates are removed before sintering, since CO_2 evaporation would prevent the densification of the sample [42]. Consequently, the powder was again dry ball milled with ZrO_2 balls of 3 mm diameter during 2 days, in order to homogenise the powder and facilitate any reaction. Finally, the powder was calcined again at 1400°C for 10 hours (henceforth known as SSCAL). The mass loss was then insignificant of ~ 0.8% as shown in Table 2-2.

Table 2-2 Mass loss after calcination at different temperatures and after sintering for BZY5, BZY10, and BZY20.

Mass loss (in %) for	Calcination at 1200°C	Calcination at 1200°C + 1400°C	Sintering at 1720°C	Theoritical mass loss
BZY5	14.0 ± 0.2	0.8 ± 0.3	4.0 ± 0.5	14.3
BZY10	13.8 ± 0.2	0.8 ± 0.3	4.1 ± 0.5	13.7
BZY20	14.9 ± 0.2	0.7 ± 0.3	4.1 ± 0.5	13.8

The obtained powders were further processed. The calcined powders were milled in a planetary mill (200 rpm) for 3 hours. A ZrO_2 container and ZrO_2 balls of 3 mm diameter were used. The powders were axially pressed (10 MPa) into a pellet. The pre-formed pellets were then cold isostatically pressed (200 MPa). Further loads (500 MPa, 625 MPa, 750 MPa, 875 MPa and 998 MPa) were applied in order to study the influence of the isostatic compaction pressure. This experiment was performed at *Ecole Centrale Paris, Laboratoire Structures, Propriétés et Modélisation des Solides, Paris (F).*

The pellets were then sintered at 1720°C for 24 hours (henceforth known as SS1720) in a powder bed of already sintered Y-substituted barium zirconate powder. During sintering at 1720°C, ~ 4% of mass loss is observed (Table 2-2). For comparison, the pellets were also sintered at 1500°C for 10 hours. The specimens are henceforth known as SS1500.

2.1.2 Spray drying

Spray dried BZY10 powder was prepared from an aqueous solution of barium nitrate, zirconium oxynitrate and yttrium nitrate. $Ba(NO_3)_2$ (Fluka, purity: 99%), $ZrO(NO_3)_2.2H_2O$ (Auer Remy, purity: 99%) and $Y(NO_3)_3.6H_2O$ (Auer Remy, purity: 99.99%) were dissolved in distilled water so that the concentration of Ba reaches 0.1 mol/l. A laboratory spray dryer, Büchi 190, atomised the solution in a chamber of hot (~ 220°C) swirling air. The dried and partially decomposed salts were carried in the air stream through the outlet of the chamber (~ 150°C) and collected in a glass container according to [36]. The resulting powder was then calcined at 1200°C for 10 hours. The calcined powder was then planetary milled, pressed and sintered in a similar way than for the solid-state reaction method. The specimens sintered at 1500°C and 1720°C are henceforth known as SD1500 and SD1720, respectively.

2.1.3 Spray pyrolysis

The spray pyrolysis method uses the same aqueous solution as the SD route. To this solution, 17 w.% of citric acid and 17 v.% of nitric acid were added. The solution was sprayed in an oven (at 550°C) according to [43]. After spraying, a dwell of 14 hours at 550°C was applied in order to remove residual NO_x gases. The powder was calcinated at 800°C for 4 and 8 hours or at 1200°C for 10 hours. The powder was then planetary milled, pressed and sintered in a similar way as for the solid-state reaction method. The specimens sintered at 1500°C and 1720°C are henceforth known as SP1500 and SP1720, respectively.

2.1.4 “Sintering aids”

Minor elements in different quantities as listed in Table 2-3 are ball milled in isopropanol with calcined BZY10 powder prepared by the solid-state reaction method. The as prepared mixture is then dried at 70°C for 14 hours. The obtained powder is pressed and sintered at 1500°C for 10 hours. Additionally, the prepared mixture containing 1 mol.% of MgO, TiO_2, Bi_2O_3, 4 mol.% of Al_2O_3 or 0.3 mol.% of Mo were sintered with the standard sintering program (at 1720°C for 24 hours).

Table 2-3 List of the different minor elements and their concentration.

N°	Additive	Amount		
1	$BaCe_{0.9}Y_{0.1}O_{3-\delta}$	1 mol.%		
2	$BaMo_{0.33}Y_{0.67}O_3$ (oxides precursors)	1 mol.%	4 mol.%	10 mol.%
3	$BaMoO_4$	1 mol.%		
4	MoO_3	1 mol.%	4 mol.%	
5	Mo	0.28 mol.% *(=0.1 w.%)*		
6	$MgAl_2O_4$ (oxides precursors)	1 mol. %	4 mol.%	
7	$MgAl_2O_4$ (calcined at 1200 °C for 2H)		4 mol.%	
8	SiO_2	1 mol.%		
9	TiO_2	1 mol.%		
10	MgO	0.05 mol.%	1 mol.%	2 mol.% *(=0.3 w.%)*
11	$La(OH)_3$	0.7 mol.% *(=0.2 w.%)*		
12	Al_2O_3		4 mol.%	
13	Al-phosphate (AlO_4P)	0.23 mol.% *(=0.1 w.%)*		
14	B-phosphate (BO_4P)	0.26 mol.% *(=0.1 w.%)*		
15	$Ba_2Zr_{0.8}Y_{0.2}O_4$			
16	$BaZr_{0.89}Y_{0.1}Mg_{0.01}O_3$			
17	$Ba(NO_3)_2$	1 mol.%		10 mol.%
18	Bi_2O_3	1.1 mol.% *(=1 w.%)*		

2.1.5 Zone annealing

A BZY10 standard specimen (SS1720) is prepared by the solid-state reaction method as described above. The high temperature annealing is then performed at *PSI, Laboratory for Neutron Scattering, Villigen (CH)*. The specimen is annealed in an optical floating zone furnace (FZ-T-10000-H-IV-VP-PC, Crystal System Corp., Japan) using four 1000 W halogen lamps as a heat source (displayed in Fig. 2-3). The focused light is moved along the sample (back-and-forth) with a rate of 5 mm/h. The maximum temperature in the hot zone is ~2200°C. The annealing is performed in oxidizing atmosphere (5% O_2 in Ar) at a pressure of 2 bars and a gas flow of 250 ml/min. The sample after annealing in the optical floating zone furnace is henceforth known as the ZA2200 (where ZA stands for Zone Annealing).

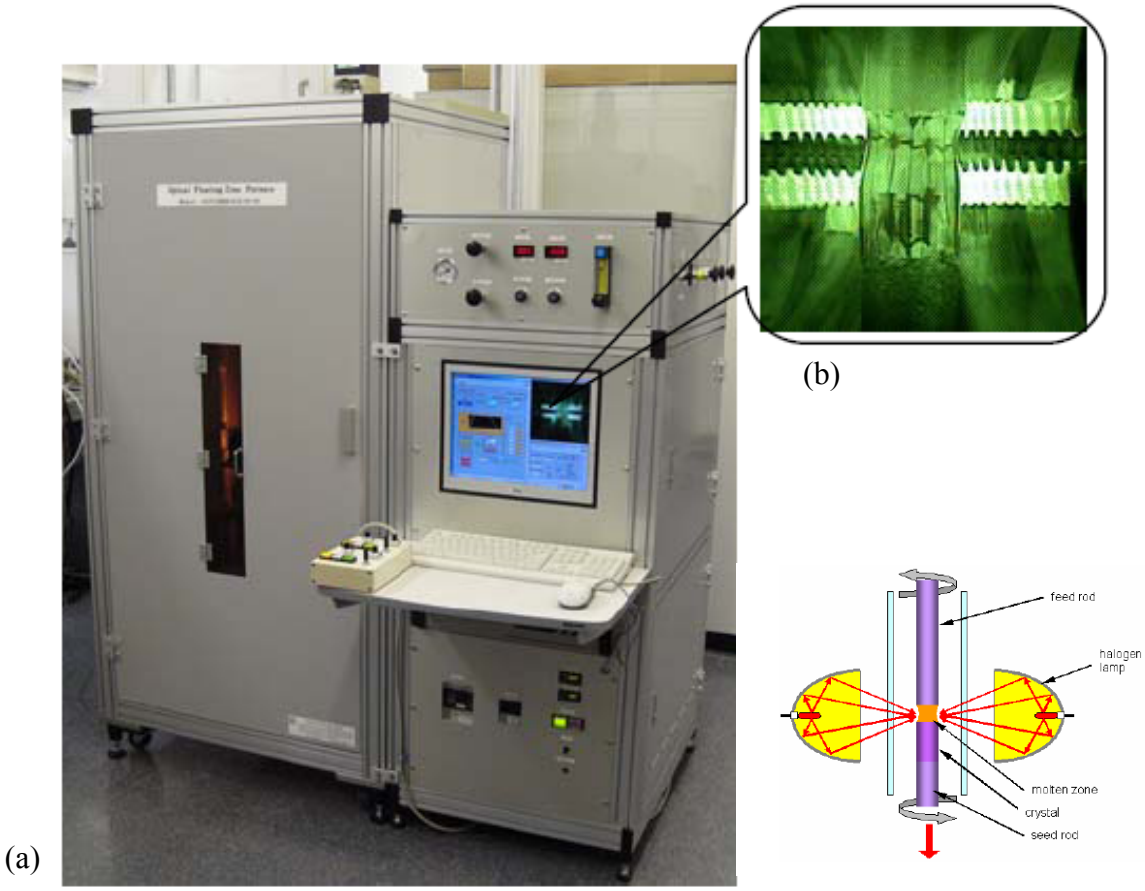

Fig. 2-3 Optical Floating Zone Furnace FZ-T-10000-H-VI-VP-PC (Crystal Systems Corp.) is displayed in (a). A picture of the sample is illustrated in (b). The principle is reported in (c). The pictures are reproduced from http://ldm.web.psi.ch/.

2.2 Morphology and microstructure

2.2.1 Grain size distribution by granulometry

The distribution of grain sizes is measured with a particle size analyzer, Malvern Mastersizer X, Malvern Instrumentation Ltd. The principle is based on laser-granulometry. If the particles are assumed to be spherical, the optical properties as the size of particles dispersed in a solution determine how the incident light is scattered. Detection of the scattered light at distinct portions allows determining the particle size distribution by using an appropriated model. In the present work, the powder is dispersed in isopropanol using an ultrasonic bath in order to destroy the eventual agglomerates.

2.2.2 Surface area by Brunauer-Emmet-Teller method

The surface area of powders is measured with a Beckman Coulter SA3100^{TM}, Coulter SA, and determined from the BET (Brunauer-Emmet-Teller) model. The principle is based on the isothermal adsorption/desorption of helium. The model is valid for meso and macroporous specimens (pore size above 2 nm).
Prior to the measurements, the powder is dried during at least 3 hours at 200°C under an argon flow.

2.2.3 Microstructure by scanning electron microscopy

Scanning electron microscopy (SEM) is used to analyse powders, fracture surfaces and polished cross-sections of sintered specimens. The grain size of sintered samples is evaluated by taking the mean diameter of 10 representative grains.
The microstructure is examined with a scanning electron microscope, Zeiss Leo 1530, Zeiss. Samples for SEM investigations are mounted on aluminium sample holders using a carbon conductive paste and sputtered with a conductive layer of gold.

2.2.4 Imaging by transmission electron microscopy

Transmission electron microscopy (TEM) is performed on dense sintered specimen. The specimens are prepared by mechanical thinning, dimple grinding and subsequent ion milling with Ar ions (4.3 keV, angle of incidence: 4°) of the layers. The TEM micrographs are taken in a transmission electron microscope FEI F30, FEI Company, at 300 kV.

2.2.5 Density

The apparent density, d, of massive specimens is determined out of the sample geometry according to Eq. 2-1 and compared to the theoretical density, which is ~ 6.2 g/cm^3 for $BaZr_{0.9}Y_{0.1}O_{3-\delta}$ [31]:

$$d = \frac{m}{S \times l} \qquad \text{Eq. 2-1}$$

where m is the mass of the specimen, S the surface and l the length.

2.3 Crystallography by x-ray diffraction

Phase analysis of powders and massive samples is performed using x-ray diffraction (XRD) with a PANanalytical, X´Pert PRO using a Ni-filtered Cu Kα (λ = 0.15405 nm). Intensities are obtained in the 2θ range between 5° and 80° with a step of 0.02°. The lattice parameters are determined with the software X´Pert using pseudo-Voigt as fit functions.

2.4 Thermal analysis by thermogravimetry

The formation of Y-substituted barium zirconate from carbonates or nitrates precursors is studied by thermogravimetric analysis and differential temperature analysis (TGA-DTA). The test samples are mixed oxides and carbonates prepared following the solid-state reaction method, spray dried and spray pyrolysed powders. The measurements are performed with a Netzsch STA 409, Netzsch, under synthetic

air (He (80) / O_2 (20) with a flow rate of 50 ml/min), with a heating rate of 5°C/min. In order to determine which species evaporate, the thermoanalyzer is in certain cases hyphenated with a mass-spectrometer (MS), Aëolos, using an electronic impact ionisation and a quadrupole detection.

2.5 Electrical conductivity by impedance spectroscopy

Electrical conductivity is a measure of a material's ability to transport electrical charges. When an electrical potential difference is placed across a conductor, the movement of the mobile charge carriers determines the electrical current. A measurement technique often used to investigate the electrical properties of ceramics is the impedance spectroscopy (IS) [44]. Generally, the conductivity is monitored for different atmospheres and temperatures.

2.5.1 Instrumentation

The equipment used for measuring impedance is shown in Fig. 2-4 [45].

In the Probostat A^{TM} cell [46], the sample is placed on a long support alumina tube as schemed in Fig. 2-5. The sample is contacted with 2 electrodes made out of platinum. A spring-loaded alumina assembly holds the sample and electrodes in place. A thermocouple is used to measure the temperature close to the sample position. Electrical connections are made via standard multiconnectors, coax cables suitable for standard impedance spectrometer connectors, and standard thermocouple compensation cables. Gases can be fed in single or dual chamber mode directly onto electrodes.

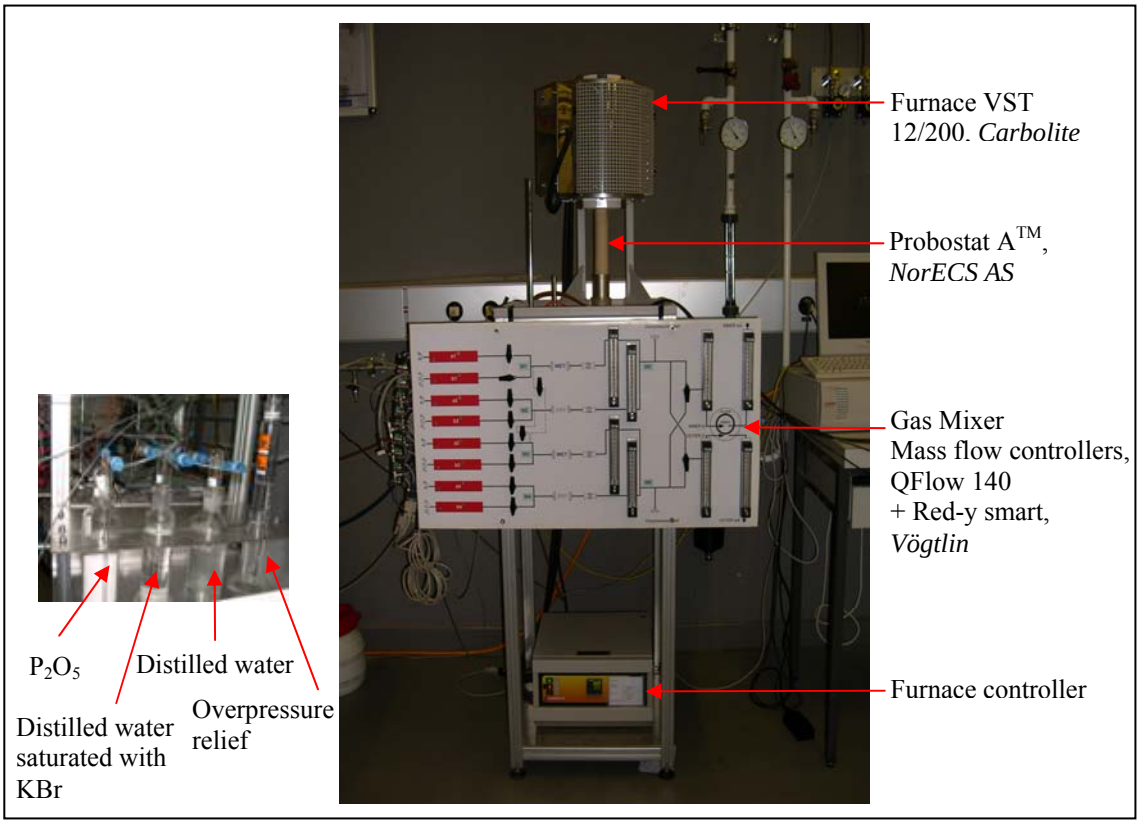

Fig. 2-4 The set-up for conductivity measurement built at Empa.

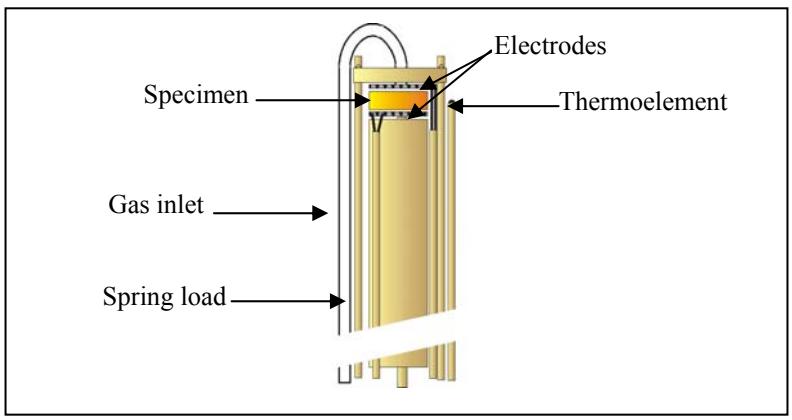

Fig. 2-5 Scheme of the specimen placed in the Probostat A™ cell (figure reproduced from www.norecs.com).

The furnace sets the temperature around the sample. It is a vertical tubular furnace, which covers the closed outer tube of the Probostat A^{TM}. The sample position is located in the centre of the hot zone of the oven.

The gas mixer has been designed in order to control the atmosphere(s) around the sample [47-50]. The flowchart is displayed in Fig. 2-6. Computer controlled mass flow controllers (MFC) regulate the gas flow rate. A wide range of gas partial pressures, pO_2, pH_2 or pD_2, is achieved by adjusting the flow rate of these gases and the flow rate of Ar or N_2. Table 2-4 presents the mixing ranges of the different gases. A wide range of water partial pressures, pH_2O, can be set independently of the partial pressure of the gas.

One line of the gas mixer is dedicated to the humidification of the gas (Fig. 2-6). It is achieved by bubbling the gas into deionized water at 25°C in order to saturate the gas up to $32x10^2$ Pa. Then, the gas is passed through deionised water saturated by KBr at 25°C in order to reduce the partial pressure of water down to $22x10^2$ Pa (referred as "wet" conditions in the following) [51]. A parallel line serves for drying the gas (Fig. 2-6). It is achieved by having the gas passed through phosphorous pentoxide (P_2O_5) with colour indicator (Fluka, Sicapent). It leads to a water partial pressure of 10 Pa (referred as "dry" conditions in the following). Intermediate partial pressure can be achieved by adjusting the flow rate of the "wet" and the "dry" gases. Prior to the conductivity tests under dry conditions, the samples are conditioned under dry oxygen at 900°C for 14 hours.

In order to ensure an overpressure of $10x10^2$ Pa in the cell, an overpressure relief system has been installed. A column with oil (di-butylphtalate, Fluka) is preferred as the cheapest and most reliable method to ensure this low overpressure.

Table 2-4 Mixing ranges.

Parameter range	Working range
Total flow rate	2.5 to 250 ml/min
Partial pressure of water	10 to 2200 Pa
Gas mixing	O_2 - Ar (or N_2) $(1.10^{-7}$ - 1 $)x10^5$ Pa
	H_2 - Ar (or N_2) $(1.10^{-7}$ - 1$)x10^5$ Pa
	D_2 - Ar (or N_2) $(1.10^{-7}$ - 1$)x10^5$ Pa

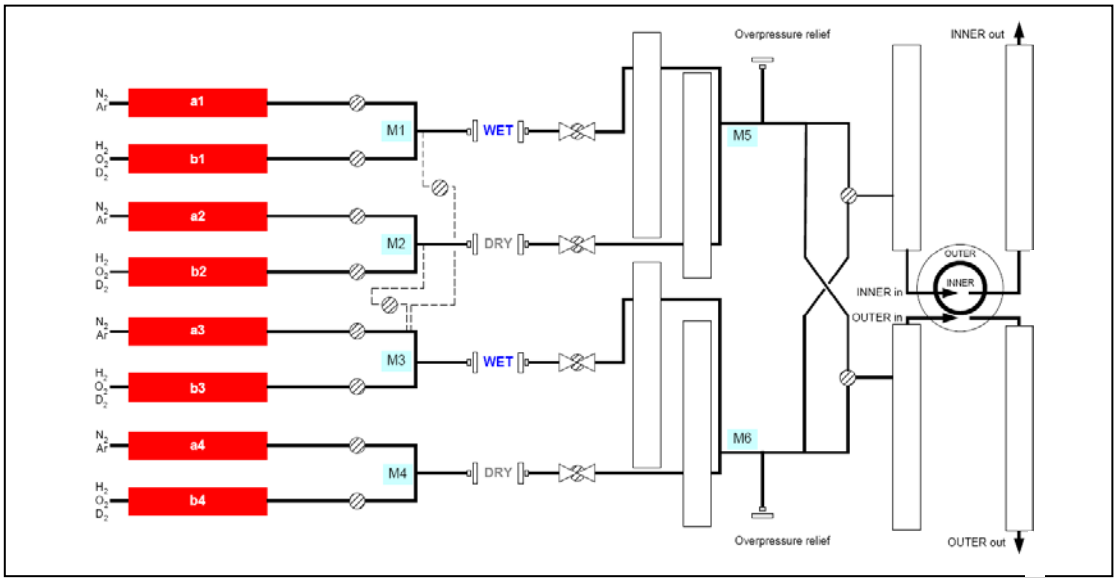

Fig. 2-6 Flowchart of the gas mixer.

2.5.2 Sample, sample preparation and method for conductivity measurements

2.5.2.1 Electrolyte and electrode preparation

The samples have a disk shape of ~ 10 mm diameter and ~ 1.5 mm thickness. The samples are contacted with a Pt-paste from Metalor A4338A, which does not contain any flux in order to prevent from any contamination. The samples are painted with the Pt-paste on both sides, on the whole sample surface, preferably, or on a defined surface area. The Pt-paste is dried at 150°C for 15 min; this procedure was repeated 3 times and subsequently fired at 1000°C for 1 hour (Fig. 2-7. a). For the measurements, Pt-current collectors are contacted to the painted electrodes (Fig. 2-7. b).

(a) (b)

Fig. 2-7 The sample coated with Pt (a) and the Pt-current collector (b).

2.5.2.2 Sample environment and measurement protocol

The measurements are performed either isobarically or isothermally. Performing isobarical measurements consists of monitoring the conductivity under a constant partial pressure of gas for different temperatures. The present work focuses on different gaseous atmospheres:

- the wet oxidizing atmosphere (pH_2O = 2200 Pa, $pO_2 = 10^5$ Pa) and the dry oxidizing atmosphere (pH_2O < 10 Pa , $pO_2 = 10^5$ Pa). The influence of the partial pressure of water under oxidizing atmosphere can be then investigated over temperature.
- the hydrogen isotopes containing atmosphere. The measurements were performed under Ar, which is either deuterated up to pD_2O = 2700 Pa [51] or wetted up to pH_2O = 2200 Pa or dried up to pH_2O < 10 Pa. The influence of the isotopes can be then investigated over temperature.

The data acquisition is, first, performed under wet atmosphere, pH_2O = 2200 Pa, at 900°C and every 50°C down to 100°C. Prior to monitoring the conductivity under dry conditions, pH_2O < 10 Pa, the specimens are pre-treated at 900°C during 14 hours under dry gas flow.

Isothermal measurements are performed as a function of the partial pressure of water or of oxygen at a constant temperature [52, 53]. The sample is equilibrated first under atmosphere with pH_2O = 2200 Pa and successively under lower partial pressures of water until pH_2O < 10 Pa is reached. The sample is always equilibrated under wet conditions before changing the temperature. These measurements give information on the behaviour of the specimens over temperature under different atmospheres.

In all cases, successive IS measurements were recorded every 30 min. As soon as a constant value is obtained, steady state conditions are assumed.

2.5.3 Impedance data acquisition and interpretation

2.5.3.1 Parameter set for the frequency response analyser

The conductivity is measured by IS using the frequency response analyser (FRA) Solartron 1260. The frequency sweep is set to the range 1 Hz to 3 MHz with an integration time of 1 s.

Electrochemical systems are non linear system (i.e. when doubling the voltage, the current is not necessarily doubled). However, Fig. 2-8. a shows how electrochemical systems can be considered pseudo-linear when a small portion of a cell's current versus voltage curve is linear. Fig. 2-8. b presents the Nyquist plots monitored with several oscillation amplitudes for a typical BZY10 sample (the detail description is given in chapter 6). The Nyquist plots are invariant with the oscillation amplitude. Therefore, it can be concluded that an input signal in the range 0.1 to 1 V is small enough to confine it to a pseudo-linear segment of the cell's current versus voltage curve. In addition, the response of the electrolyte is linear since it is an ohmic behaviour. Hence, an input oscillation amplitude of 1 V is used in the present work in order to study the electrolyte behaviour.

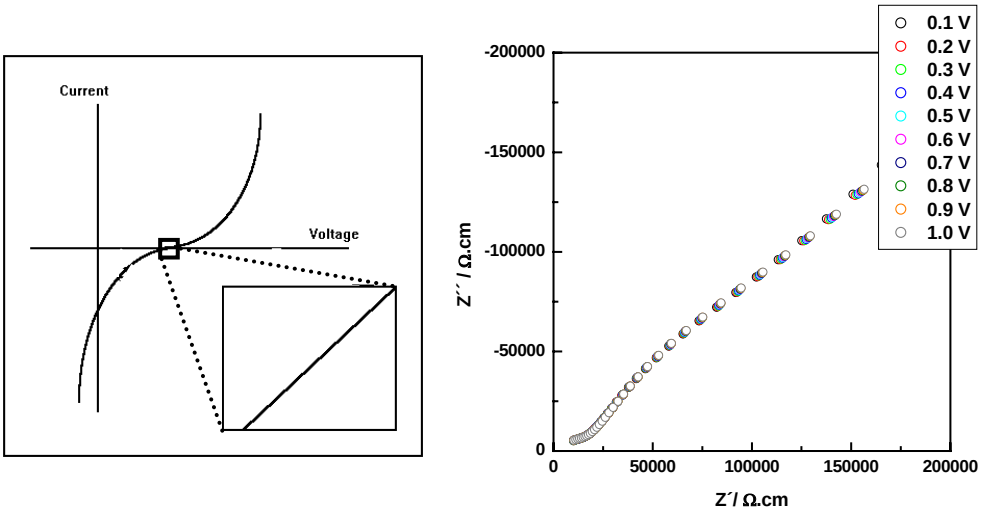

(a) (b)

Fig. 2-8 Current versus voltage curve showing pseudo-linearity (figure reproduced from www.gamry.com) (a). Nyquist plot at 200°C under wet O_2, pH_2O = 2200 Pa, with different oscillation amplitudes (b). The experiment was performed on the specimen annealed at high temperature sample, ZA2200 (chapter 6).

2.5.3.2 Deconvolution and fitting of impedance spectra

The deconvolution of measured impedance spectrum aims to identify possible equivalent electrical circuits that reproduce the spectrum reasonably well.
The fitting procedure follows a subtraction routine [54]. Recognizable parts of the overall spectra are modelled with simple subcircuits over a limited frequency range. Subtracting the selected subcircuit will reveal contributions of other subcircuits that are not observable by visual inspection of the measured data. This routine leads to a possible equivalent circuit, while, at the same time, optimized parameter estimates are obtained for the subsequent full fit. In the present work, the measured impedance spectra are analysed by using the ZView software (Scribner Associates, Inc.).

2.5.3.3 Equivalent circuits and physical systems

A parallel circuit of a resistor and a capacitor is a typical representation of a solid ionic conductor with a not too high conductivity. A resistor is an element with long range transport of charge carriers. A capacitor comprises an ideal insulator between two conductors. In non ideal systems, a constant phase element, Q, is used instead of a capacitance, C and can be described by Eq. 2-2:

$$Z_Q = (Y(j\omega)^n)^{-1} \qquad \text{Eq. 2-2}$$

where j=√-1, ω=angular frequency, and Y and n ($0 \le n \le 1$) are constant [40], and the related capacitance is characterized by Eq. 2-3:

$$C = Y^{1/n} R^{1/n-1} \qquad \text{Eq. 2-3}$$

If n=0, the constant phase element represents a pure conductor (resistor) and if n=-1, it is a pure inductance. A conductor may also contain an inherent inductor, since current through the sample may induce electromagnetic fields.

In many cases, the resistances due to the grain interior (also called bulk in the following) and the grain boundaries are different and can be separated. The “brick layer model” [40, 44, 55] is the simplest model to determine the conductivity of a

polycrystalline material. It simplifies the real microstructure of the samples as sketched in Fig. 2-9. a, by an "ideal" microstructure assuming that all grain sizes are similar and cubic as illustrated on Fig. 2-9. b. The impedance data can be then modelled by an equivalent circuit, which takes into account the resistance of the grain interior, R_b, the geometrical capacitance of the sample, C_b, and the grain boundary resistance, R_{GB}, and grain boundary capacitance, C_{GB}. As the grain size, d_g, is much larger than the grain boundary thickness, d_{GB}, and as the permittivity of the grain interior is generally assumed to be equal to the one of the grain boundary, the capacitance of the bulk is much lower than the capacitance of the grain boundaries [55].

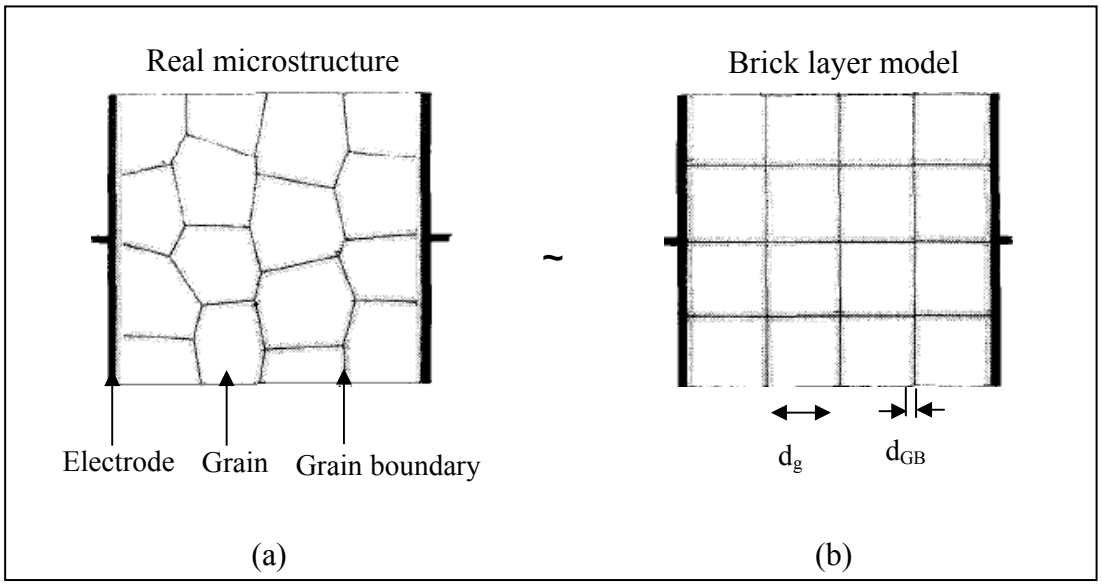

Fig. 2-9 The real structure (a) is approximate by the "brick layer model" (b), which assumes that all grains are similar, cubic, with a size of d_g and are separated by identical grain boundaries of a thickness of d_{GB} [40, 56].

2.5.3.4 Normalization of the data

The conductivity can be determined out of the modelled resistance. It is defined as the inverse of the resistance corrected from the sample geometry according to Eq. 2-4:

$$\sigma = \frac{L}{A}\frac{1}{R} \qquad \text{Eq. 2-4}$$

where L is the sample length, A the electrode surface area, and R the measured resistance.

The above analysis assumes dense specimens. In porous samples, the porosity generally reduces the effective conductivity further. For porous materials, specific values take into account the microstructure. Such specific values can be defined for the bulk and for the grain boundaries. Wang et al. investigated the conductivity of porous specimens [20] and gave an experimental correlation between the apparent bulk conductivity of a porous sample and its specific bulk conductivity, $\sigma_{sp.\ b}$, as described by Eq. 2-5:

$$\sigma_{sp.b} \approx \frac{L}{A}\left(\frac{1}{1-V_V}\right)\frac{1}{R_b} \qquad \text{Eq. 2-5}$$

where V_V is the fraction porosity, L is the sample length, A the electrode surface area, and R_b the bulk resistance.

Assuming that the dielectric constant of the grain boundaries is approximately equal to that of the bulk, a semi-quantitative measure of the specific grain boundary resistance, $\sigma_{sp.\ GB}$, can be obtained from the impedance data without resort to a microstructural examination [40], according to Eq. 2-6:

$$\sigma_{sp.\ GB} = \frac{L}{A}\left(\frac{C_b}{C_{GB}}\right)\frac{1}{R_{GB}} \qquad \text{Eq. 2-6}$$

where L is the sample length, A the electrode surface area, C_b the bulk capacitance, C_{GB} the grain boundary capacitance, and R_{GB} the grain boundary resistance.

2.6 Proton concentration

The proton concentration in the material can be determined by measuring the weight changes induced by the incorporation of water molecules into the vacancies of the perovskite structure. Several studies [57-63] measured already the so-called “water

uptake" by thermogravimetry on powders. Investigations on powders are advantageous since long equilibration times can be avoided. In order to be able to observe the proton loading, the measurements have to be performed in-situ using a differential thermobalance. In the case of dense specimen, long equilibration times due to slow kinetics of the water uptake have to be taken into account. The measurements can be done ex-situ using a precision scale but only on dense specimens. Using dense sample is interesting since the sample can be used to perform conductivity test, XRD and concentration measurements. The measurements were performed only ex-situ on dense specimens in the present work. The experimental process and the data interpretation are described below.

2.6.1 Determination of the water uptake in dense specimens

Degassing or loading the samples with water is achieved by passing dry, or wet gas over the dense samples at a given temperature in a tubular furnace. The "dry" reference state is obtained by heating the samples at 900°C during 14 hours under dry oxygen, $pH_2O < 10$ Pa. The humidification is achieved by passing wet oxygen, $pH_2O = 2200$ Pa, at 600°C during 24 hours. Intermediate partial pressures of water are achieved by adjusting the mixing ratio of dry and wet gases. After the drying or humidifying treatment, the samples are quenched to room temperature by removing them quickly from the furnace and weighed with a precision scale.

2.6.2 Calculation of the proton concentration

The water uptake is determined by comparing the mass of a dried massive specimen, and the mass of the same specimen loaded with protons. The proton content, $[OH^{\bullet}]$, is then obtained from the following relationship (Eq. 2-7), based on the validity of Eq. 1-2:

$$[OH^{\bullet}] = \frac{\Delta m}{m_0}\frac{M_{BZY\ 10}}{0.5 M_{H_2O}} \approx \frac{\Delta m}{m_0} 30.61 \qquad \text{Eq. 2-7}$$

where m_0 is the mass of the dried sample, Δm is the mass uptake after humidification, M_{BZY10} and M_{H_2O} are the molecular weights of BZY10 and H_2O, respectively.

The validity of this equation relies on the dissociation of all water molecules present in the specimen.

2.7 Proton diffusivity

The ability of the protons to move can be evaluated directly by quasi-elastic neutron scattering experiments or indirectly by conductivity measurements. Details on the two approaches are given below.

2.7.1 Diffusivity by quasi-elastic neutron scattering

2.7.1.1 Theory

The diffusion coefficient can be directly measured by quasi-elastic neutron scattering (QENS). Neutron spectroscopy consists of measuring changes in both the energy and the momentum of neutrons, which interacts with the material. As neutrons have wavelengths in the range of the atom spacing and as their energies are in the same order of magnitude as the elementary excitations, the neutron spectroscopy allows studying the interactions of atoms in detail. Fig. 2-10 shows the different interactions between the neutrons and the materials. On the one hand, neutrons scatter elastically. Elastic scattering implies no change in the neutron energy i.e. $\hbar\omega = 0$ (where $\hbar$ is the reduced Planck's constant and ω the frequency). On the other hand, neutrons can also scatter inelastically. The neutron energy changes by inelastic scattering i.e. $\hbar\omega \neq 0$. Thus, QENS refers to a scattering phenomenon which is centred at zero energy, E_0, transfer but which introduces a broadening of the spectral width due to the diffuse motions.

The corresponding wave vector, $\vec{Q}$, is given by Eq. 2-8:

$$\vec{Q}=\vec{k}-\vec{k_0} \qquad \text{Eq. 2-8}$$

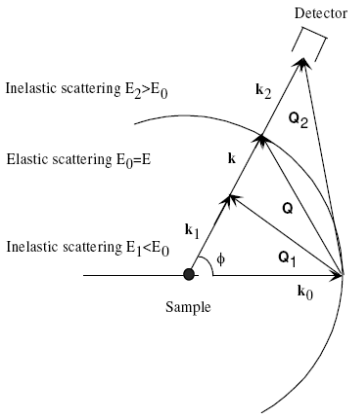

Fig. 2-10 Scattering geometry. The figure is reproduced from [64].

The principle (Fig. 2-10) of QENS is:

- incident neutrons are selected from the white beam of the reactor core in a small range around E_0 and are focused on the sample in the direction k_0,
- the final energy, E, of the scattered neutrons is collected by the detector and analysed to determine the energy changes: $\hbar\omega = E - E_0$,
- the scattering angle with respect to the incident beam and with respect to the sample orientation, evaluated by the wave vector transfer, Q, must be measured to determine the momentum transfer.

2.7.1.2 Experimental

Eight samples of BZY10 with a bar shape of ~ 36 mm length, ~ 6 mm width and ~ 2 mm thickness are prepared (chapter 3). They are exposed to humid atmosphere (pH_2O=2200 Pa and $pO_2=10^5$ Pa) for 24 hours at 600°C in order to load them with water. They are subsequently quenched at room temperature. The samples are then placed along the walls of a platinum container (from *PSI, Laboratory for Neutron Scattering, Villigen (CH)* and *Saarland University, Physical Chemistry, Saarbrücken (D)* [65]). And the container is sealed with a cupper gasket. As gases expand with temperature and as protons are likely to evaporate at high temperatures, an over pressure valve is mounted on the container in order to allow a maximum overpressure of ~ 0.5 Pa.

The QENS experiment is performed at FOCUS (*PSI, Laboratory for Neutron Scattering, Villigen (CH)*) at the Swiss spallation neutron source, SINQ. The instrument used for the neutron spectroscopy is sketched in Fig. 2-11.

In the following, the principle of the instrument is given in brief. FOCUS is a time of flight (TOF)-spectrometer. It is based on the hybrid principle allowing the determination of the final neutron energies through a direct measurement of their velocities. By means of a vertically converging neutron guide the size of the white beam is reduced and then chopped by a pre-selector disc chopper. FOCUS has no chopper monochromator, it makes the beam monochromatic through reflection on a crystal (either graphite or mica) combined with a Fermi chopper. The monochromator selects neutrons of a wavelength of 6 Å, which corresponds to an incident energy of 2.273 meV from the incoming white neutron beam. A Q-range of $0.35\ 1/Å \leq Q \leq 0.85\ 1/Å$ was investigated

Then, the continuous and monochromatic neutron flux is chopped in short bursts to set a time mark t = 0 for the flight time of the neutrons from the chopper to the detectors. The TOF chopper ratio is 1:3. The Fermi chopper is located between the monochromator and the sample at a 0.5 m distance in front of the sample. It is a rotating slit package with a straight collimation of 1°. It achieves the pulsing of the neutron beam. Arrays of 383 detectors are placed in the scattering plane at a distance of 2.5 m to simultaneously collect counts for several wave-vectors. The detectors cover a range of scattering angles between 30° and 130° and are connected with a multichannel analyser to register the total flight time of the neutron burst

Spectra were then recorded from 500 K to 900 K, in steps of 100 K.

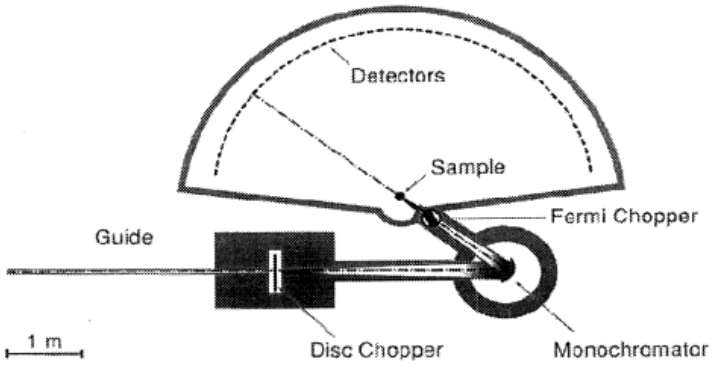

Fig. 2-11 Scheme of the spectrophotometer FOCUS. The figure is reproduced from [66].

2.7.1.3 Data interpretation

The experimentally obtained scattering function, S(Q, ω), are deconvoluted into elastic (gaussian), quasielastic (lorentzian) and linear background scattering contribution [65]. The data obtained at 300 K serve for background subtraction, assuming that protons are virtually immobile at this temperature. The instrument resolution is determined by a separate measurement of a vanadium sample. The deconvolution of the raw data is performed with the DAVE software package (U.S. NIST) [67].

2.7.2 Diffusivity by impedance spectroscopy

The diffusion coefficient can be determined indirectly using the relation between the conductivity, σ, and the diffusivity of proton, D, according to Eq. 2-9:

$$\sigma = \frac{e^2}{k_B T}\frac{[OH^{\bullet}]}{V}D \qquad \text{Eq. 2-9}$$

where $[OH^{\bullet}]$ is the concentration of protons, V the volume per BZY10 unit cell, k_B the Boltzmann constant, T the temperature and e the elementary charge [68, 69].

2.7.3 Arrhenius interpretation

The activation energy can be calculated from these data. In a protonic regime, the activation energy reflects the energy barrier that the proton has to overcome for diffusion. When the concentration of protons remains constant in temperature, the activation energy of the conductivity, E_a, is just the migration energy of protons [70]. It can be determined from the conductivity, σ, but also from the mobility, D as shown in Eq. 2-10:

$$DT = \sigma T = \sigma_0 \exp(-\frac{E_a}{k_B T}) \qquad \text{Eq. 2-10}$$

where k_B is the Boltzmann constant, T the temperature, and σ_0 is the pre-exponential factor.

The pre-exponential factor, σ_0, is a constant built up of the number of possible jump directions, z, jump distance, d, fraction of jump destinations that are vacant, N, vibration frequency, ν_0, and jump entropy, ΔS [5]. In consequence, the pre-exponential factors contain information on the nature of charge carrier, microstructure, crystallography and energy of the sample investigated.

CHAPTER 3

Crystallographic, Microstructural and Electrical Properties of $BaZr_{1-x}Y_xO_{3-\delta}$

The literature data about the conductivity of Y-substituted barium zirconate varies over more than 1 order of magnitude [17, 25, 26, 31]. These differences might arise from different measurement conditions, different proton loadings, but also different sample preparations. Thus, the aim of the present chapter is to give an extended characterisation of Y-substituted barium zirconate synthesised by the standard solid-state reaction method. This synthesis method will serve as a reference for the following chapters.

Furthermore, the details of the proton transport mechanism and the defect chemistry of perovskite proton conductors are not known in details so far. The defect phenomena and atomistic diffusion mechanisms are suspected to underpin the fundamental understanding of the macroscopic behaviour [40]. According to Eq. 1-1 and Eq. 1-2, it is clear that the concentration of protons depends on the yttrium content. Thus, data on the formation and the mobility of protonic charge carriers will be discussed on the basis of structural data for barium zirconate substituted with different amounts of yttrium.

3.1 Crystallography of $BaZr_{1-x}Y_xO_{3-\delta}$ with x = 0, 5, 10, 15 and 20

The X-ray diffraction patterns of $BaZr_{1-x}Y_xO_{3-\delta}$ (BZYx) with x = 0, 5, 10, 15 and 20 after calcination at 1200°C and 1400°C for 10 hours are presented in Fig. 3-1. For all BZYx with x = 0, 5, 10, 15, 20 , the XRD patterns are consistent with a single cubic phase material. All peaks could be indexed to $BaZrO_3$ (JCPDS 01-089-2486).

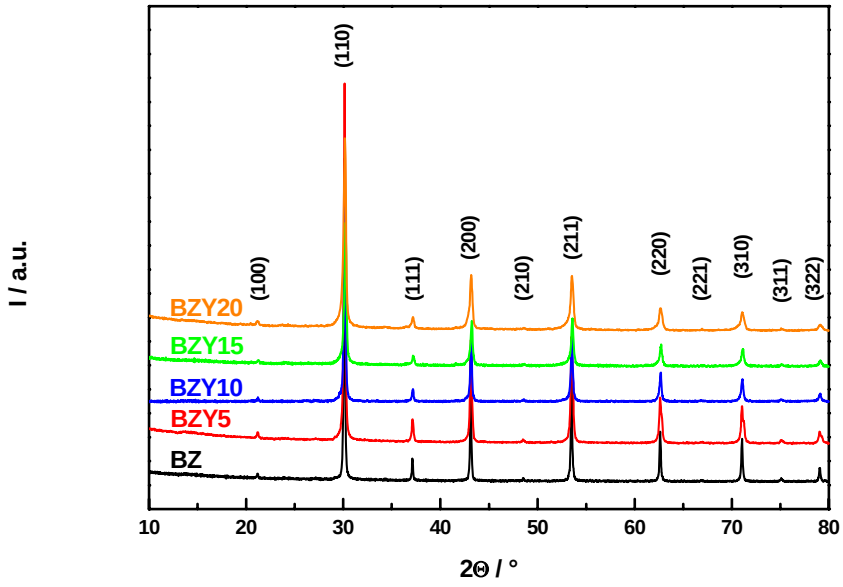

Fig. 3-1 XRD patterns of BZ, BZY5, BZY10, BZY15 and BZY20 calcined powders synthesised by the solid-state reaction method.

The lattice parameters after calcination at 1200°C and after sintering at 1720°C are plotted versus the yttrium content in Fig. 3-2. All lattice parameters are found to be cubic. After calcination, a lattice parameter of a=b=c=0.419(3) nm was found for all specimens independently of the yttrium content. After sintering at 1720°C, the lattice parameter increases linearly with the Y content from a=b=c=0.419(3) nm for BZ to a=b=c=0.423(0) nm for BZY20.

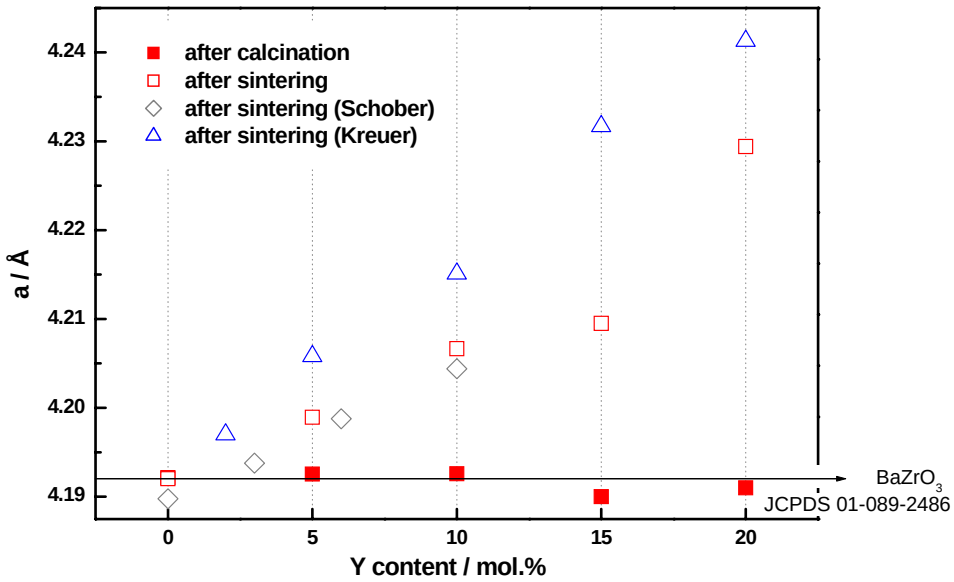

Fig. 3-2 The lattice parameters after calcination at 1200°C and after sintering at 1720°C are plotted versus the yttrium content. The results are compared to values from the literature. Schober et al. [61] and Kreuer et al. [30] find a cubic lattice parameter for $x \leq 5$. For $x \geq 10$, Kreuer et al. find a tetragonal crystallographic structure.

The lattice parameters obtained for BZYx with x = 0, 5, 10, 15, 20 are compared to values from the literature in Fig. 3-2. Schober et al. [61] and Kreuer et al. [30] found a cubic lattice parameter, which is comparable (or slightly lower for [61] and slightly higher for [30]) than the results from this work, for substituted barium zirconate with an Y content between 0 and 10 mol. %. Above 10 mol. % of Y, Kreuer et al. [30] found an increasing tetragonal distortion, whereas, in the present work the lattice parameters remain cubic.

As the Shannon´s radius of Y^{3+} is larger than the one of Zr^{4+} (Table 3-1) and as barium zirconate is a close packed structure, it is expected that incorporation of Y on the B-site of the perovskite enhances the lattice parameter. An increased lattice parameter is indeed observed for increasing Y content after sintering. Hence, it is concluded that Y is dissolved, at least partially, in the B-site of the perovskite according to Eq. 1-1.

Table 3-1 Shannon Ionic radii [71] and electronic configuration of the elements of the studied perovskite.

	Ba	Zr	Y	O
Radii (Å)	1.61	0.72	0.90	1.38
Electronic configuration	$[Xe]6s^2$	$[Kr]4d^25s^2$	$[Kr]4d^15s^2$	$[He]2s^22p^4$

The lattice parameter is surprisingly independent of the Y content after calcinations. It indicates that even if any second phase cannot be identified in the XRD patterns, the reaction may not be completed at 1200°C. Magrez et al. [32] studied by XRD the completion of the reaction of formation of BZY20. They observed that, below 1250°C, $BaCO_3$ is not fully dissolved in the structure leading to a BZY20 with a smaller lattice parameter. In the present work, no additional peak, which would correspond to $BaCO_3$, is visible in the XRD patterns.

The increase of the lattice parameter with the Y content occurs after sintering. It indicates that Y is not dissolved in the Zr-site after calcination. In this case, it seems likely that either Y takes part in the formation of a second phase or substitute in the Ba-site.

3.2 Microstructure of $BaZr_{1-x}Y_xO_{3-\delta}$ with x = 0, 5, 10, 15 and 20

3.2.1 Densification by high pressure compaction

Fig. 3-3 shows the compaction behaviour of BZY10 powders synthesised by the solid-state reaction method. The relative density of BZY10 green body increases with the applied pressure. It could reach ~ 65% when a pressure of ~ 1 GPa is applied. It is about 20% higher than by normal cold isostatic pressure (200 MPa). After sintering, the density of BZY10 is close to the theoretical density. It reaches a maximum, when a pressure of 750 MPa is applied.

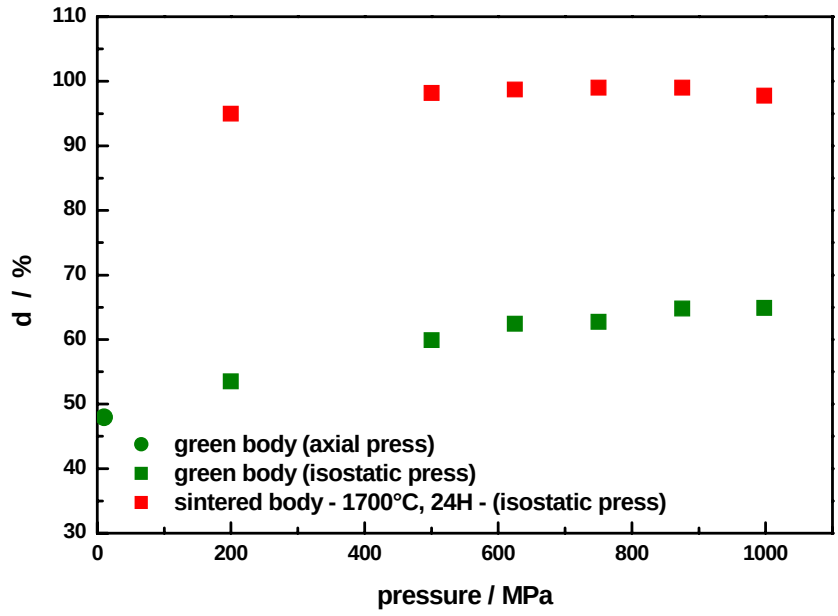

Fig. 3-3 Relative density of the green and sintered bodies of BZY10 pressed with different pressures.

Scanning electron microscope pictures of green bodies and subsequent sintered bodies of BZY10 pressed by applying different pressures are displayed on Fig. 3-4. For the green bodies, the crystallite sizes are very small. No increase of the density and the particle size (if any) with the applied pressure can be observed due to the low resolution.

The grains are found to be much larger after sintering. Moreover different microstructures are obtained depending on the applied pressure. For samples pressed with 200 MPa and 500 MPa, the grains are found to be homogenous and to show intergranular fracture. Samples pressed at 750 MPa clearly show a microstructure dominated by a few very large grains. Intragranular fracture of the bigger grains is observed. When the compaction pressure is further increased up to 998 MPa, the grain sizes tend to become more homogeneous.

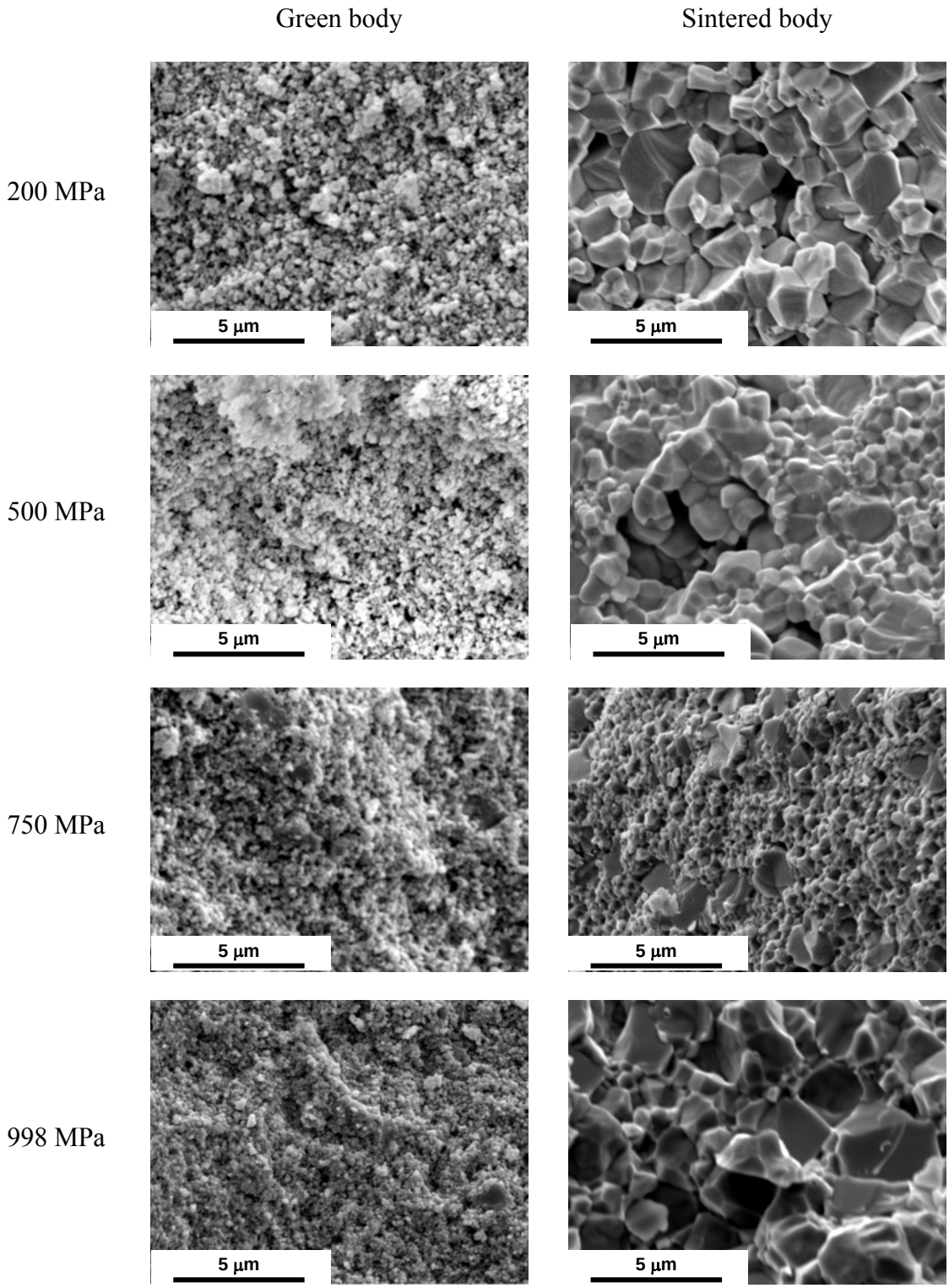

Fig. 3-4 SEM pictures of the green and sintered bodies of BZY10 pressed with different pressures.

The mean grain size after sintering at 1700°C is plotted as a function of the applied pressure in Fig. 3-5. The mean grain size clearly reaches a minimum for an applied pressure of ~ 750 MPa.

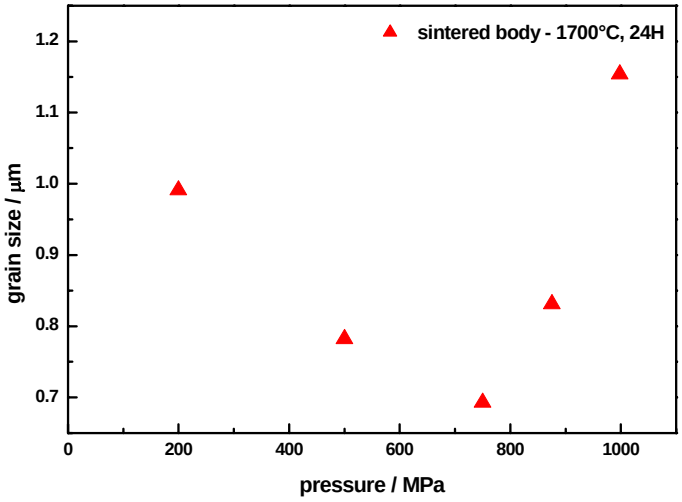

Fig. 3-5 Mean grain size of sintered BZY10 pressed at 200, 500, 750 and 998 MPa.

As shown in Fig. 3-3 and Fig. 3-4, the porosity of BZY10 specimens is nearly eliminated when ~ 750 MPa are applied. For higher applied pressures, some grains grow at a high rate and at the expense of their neighbours (Fig. 3-5). Thus, it suggests a two-step mechanism involving first a normal grain growth for specimens pressed up to 750 MPa followed by an abnormal grain growth. In order to observe an abnormal grain growth, the subset of grains must possess some advantages over their competitors such as a high grain boundary energy, locally high grain boundary mobility, favourable texture or lower local second phase particle density.

3.2.2 Grain and grain boundaries

In the following, the grains and the grain boundaries are analysed in more details for the sample isostatically pressed at 200 MPa and sintered at 1720°C. The

microstructure of BZY10 is illustrated in SEM pictures. Fig. 3-6. a shows the fracture cross section of BZY10. The specimen is dense with a few residual pores. The mean grain size is about 2 μm.

A polished cross section of BZY10 is displayed in Fig. 3-6. b. Except from what corresponds to the pores as identified in the fracture cross-section, no change in contrast is visible. If amorphous phases would be present in the vicinity of the grain boundaries, it would be expected to see grain limitations.

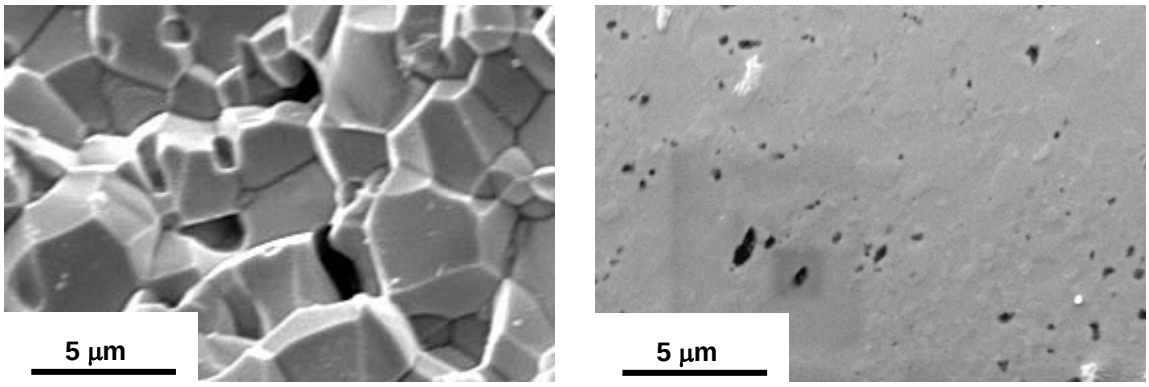

(a) (b)

Fig. 3-6 SEM pictures of a fracture cross section (a) and of a polished cross-section (b) of sintered BZY10.

TEM micrographs of a BZY20 dense specimen are shown in Fig. 3-7 and in Fig. 3-8. In Fig. 3-7, a thin amorphous layer of about 2 nm, which follows the ion-milled hole, is visible on the right side of the specimen. This amorphous part of the specimen results from the ion-milling process and does not reflect the intrinsic microstructure of the BZY20 sample. The visible crystalline zone represents the interior of BZY20 grains. Changes in contrast can be attributed to artefacts due to differences in thickness in the investigated layer. A more remarkable feature is the irregularity of the atom arrangement indicated by the presence of “wavy” fringes (marked by arrows in Fig. 3-7).

In Fig. 3-8, two different crystal orientations are clearly visible. They correspond to two grains of BZY20, which delimit the so-called grain boundary region [72]. Several of these grain boundaries were examined, but no impurities, such as amorphous glassy phases could be identified in their vicinity.

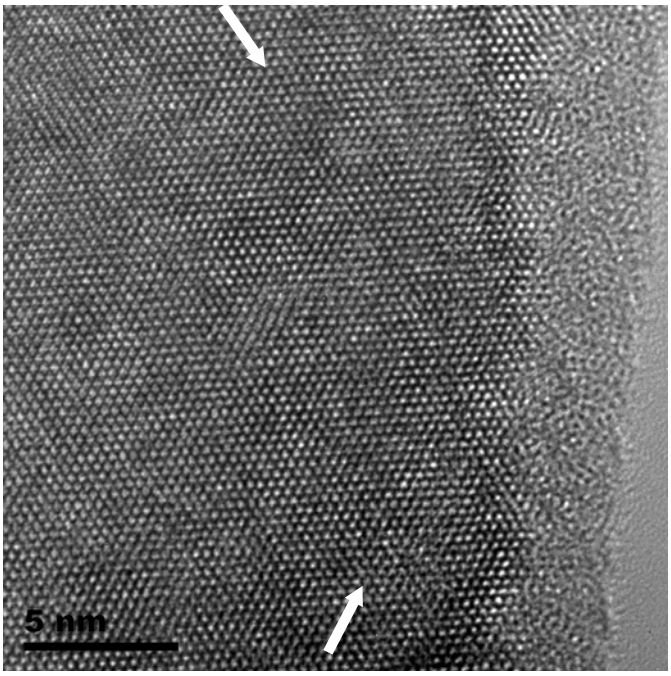

Fig. 3-7 TEM micrograph of a BZY20 grain. The arrows indicate lines of vision along which significant lattice distortion can be observed.

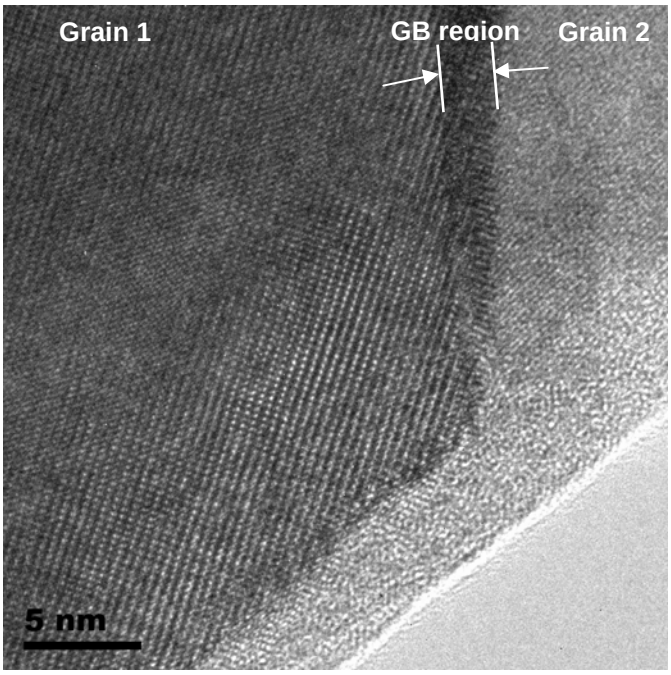

Fig. 3-8 TEM micrograph of a BZY20 specimen. A grain boundary region between two BZY20 grains is marked by an insert.

3.3 Proton concentration of $BaZr_{1-x}Y_xO_{3-\delta}$ with x = 0, 5, 10, 15 and 20

3.3.1 Dependence of the proton concentration on the Y content

Fig. 3-9 presents the equilibrium proton concentration measured at 600°C versus the Y content. For comparison, the theoretically calculated from Eq. 1-2 proton concentration is plotted. The proton content is proportional to the Y content: by doubling the Y content from 10 to 20 mol.%, the proton concentration is also doubled from ~ 3 to ~ 6 mol.%. For BZ, no weight changes are observed. From Eq. 1-1 and Eq. 1-2, the proton concentration of the material depends on the oxygen vacancy concentration and, hence, on the substituant content. The introduction of 1 substituant creates 1/2 vacancy and after humidification 1 protonic defect. The unsubstituted parent composition, $BaZrO_3$, nominally contains no oxygen vacancies. This is consistent with the absence of weight change.

The experimentally obtained values are much smaller than the theoretically possible values and the difference is more and more pronounced when the Y content increases. It suggests either that the concentration of oxygen vacancies is smaller than expected or that oxygen vacancies are trapped and cannot be filled by protons. It must be considered that similarly to the concentration of protons, the lattice parameter is smaller than what is predicted theoretically (Fig. 3-2). This supports the idea that the concentration of oxygen vacancies is smaller than expected.

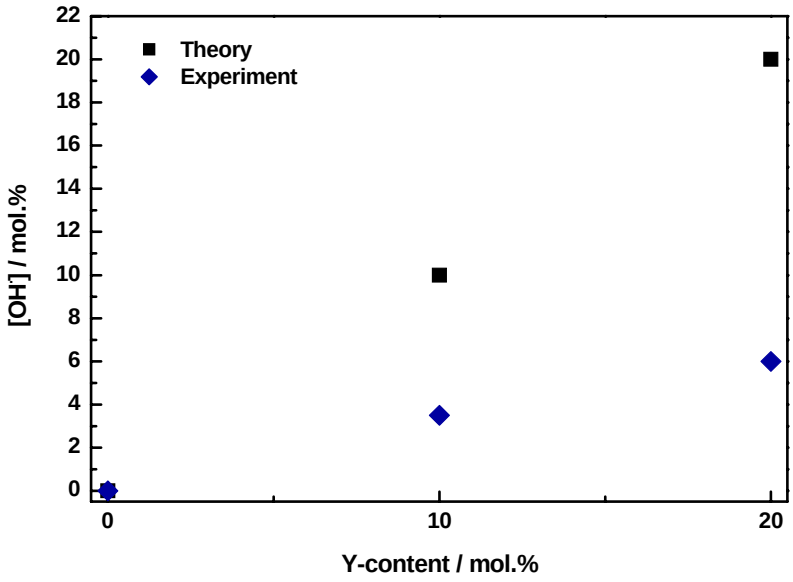

Fig. 3-9 The proton concentration as a function of the yttrium content is given. Protons were loaded at 600°C. For comparison, the theoretically possible proton content is given as well.

3.3.2 Water partial pressure and temperature dependence of the proton concentration

Fig. 3-10 shows the equilibrium proton concentration at 600°C as a function of the partial pressure of water in oxygen. The proton content increases with increasing the water partial pressure in the range 0 to 3000 Pa. Around the usual measurement conditions, i.e. $pH_2O = 2200$ Pa, a variation of 1000 Pa induces a variation of 0.5 mol.% of protons. Groβ et al. [27] showed as well such a high dependence of proton concentration on the water partial pressure. They found that a constant concentration of protons is reached only at very high partial pressure of water ($> 3x10^4$ Pa).

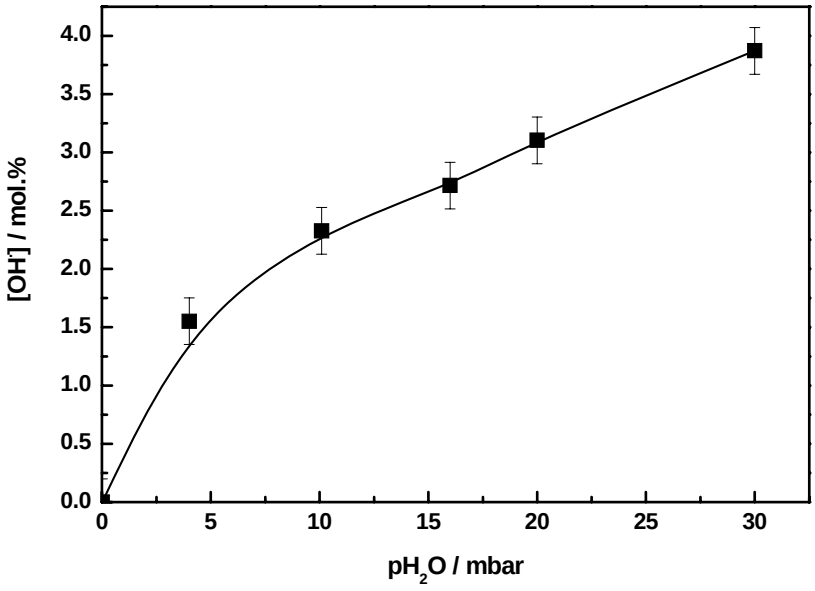

Fig. 3-10 Proton concentration of BZY10 after equilibration at 600°C as a function of the water partial pressure in O_2.

The proton uptake in humidified atmospheres was investigated for dense BZY10 samples as described in chapter 2. Fig. 3-11 presents the concentration of protons as a function of time and temperature of exposure to wet O_2, pH_2O = 2200 Pa. The highest concentration of protons at equilibrium is achieved at the lowest temperature (400°C). In addition, the equilibration concentration is achieved more slowly when the temperature decreases. For instance, the equilibrium proton concentration in BZY10 is about 4 mol.% and is achieved after 10 hours of exposure to humid atmosphere at 500°C.

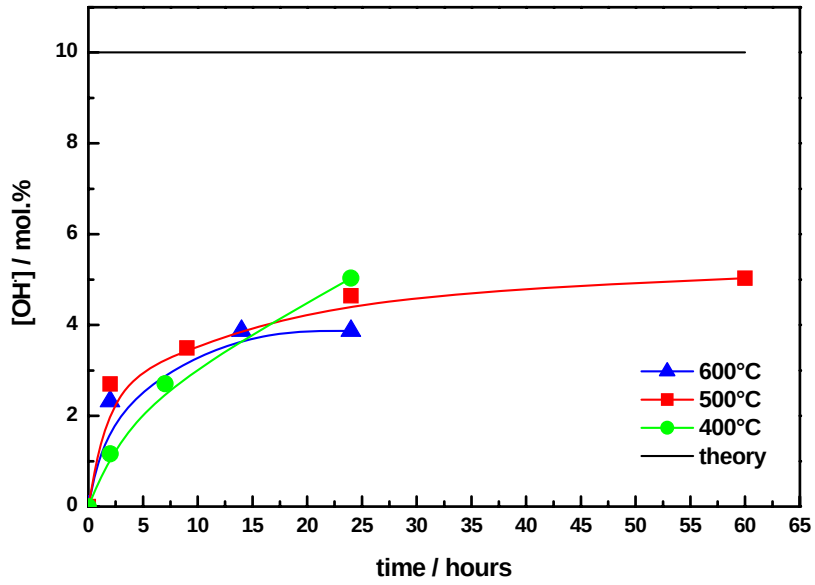

Fig. 3-11 Proton concentration of BZY10 determined at 400°C, 500°C and 600°C versus different equilibration times under wet O_2, pH_2O = 2200 Pa.

The equilibrium concentration measured on a BZY10 dense pellet is presented as a function of the temperature in Fig. 3-12 and is compared to values calculated from a thermodynamic analysis of thermogravimetry data on powders from [30]. The experimentally obtained concentrations are lower on pellets than on powders. This discrepancy is even more pronounced for temperatures below 400°C. A closer inspection of the equilibration time (Fig. 3-11) reveals that even for long exposure times the resulting values remain below the thermodynamic equilibrium values obtained for powders.

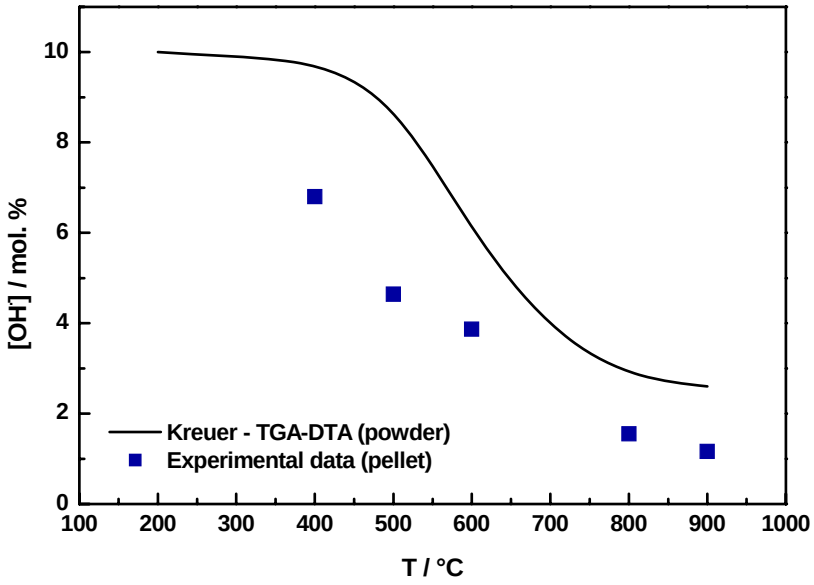

Fig. 3-12 Comparison of the proton concentration in dense specimen at equilibrium to the proton concentration calculated from a thermodynamic analysis of thermogravimetry data for powders by Kreuer et al. [30].

In the following, protons were loaded at 600°C. Subsequently, BZY10 dense specimens were quenched to room temperature. BZY10 dense specimens were then heat treated at either 300°C or 400°C or 500°C or 600°C or 700°C or 900°C under air for 10 hours. The concentration of protons was then determined and is plotted as a function of the temperature of heat treatment in Fig. 3-13. The proton concentration is constant within the experimental uncertainty (~ 2.75 mol. %) up to 500°C. Above 500°C, the proton concentration is drastically decreasing.

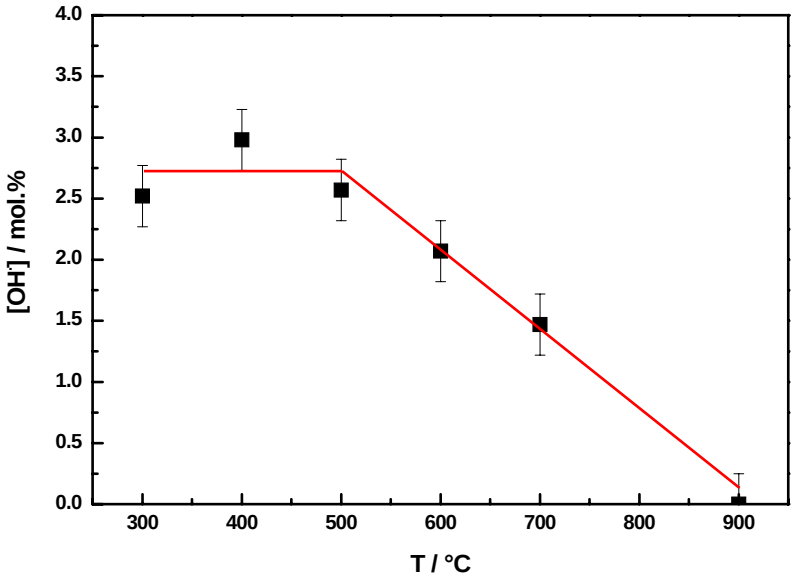

Fig. 3-13 Proton concentration versus the temperature of exposure.

The values of the proton concentration from the different figures shown above appear reasonable and are comparable to those of other prominent proton conductors [57, 59-61, 73-75]. Nevertheless, a closer inspection of the equilibration time (Fig. 3-11) reveals that even for long charging times the resulting values constantly lie below the thermodynamic equilibrium values obtained for powders (Fig. 3-12). Several explanations are likely and are discussed in the following.

First, Eq. 2-7 assumes that the water dissociation is the only reaction and that the water is totally dissociated. Small weight increases have been observed by Schober et al. [61] under dry synthetic air as the temperature was decreased from 800°C to 300°C. This weight change was ascribed to a reversible oxygen uptake at low temperatures and was evaluated to 0.05%. As the present work was performed under pure oxygen, an even smaller weight change is expected. Similarly, it is also possible that part of the water is only adsorbed on the surface or not dissociated and is not taking part in the proton transport.

Secondly, it is very likely that the so-called “drying” step is not sufficient to remove all the protons and/or that some protons are loaded while being quenched. For instance, Nowick et al. already showed by infrared spectroscopy that some residual

protons remain after a drying step of few hours at 900°C [18]. In consequence, the dry reference specimens from our work most probably contain protons.
Thirdly, the conditions of complete protonation/deprotonation have not been met as suggested by Fig. 3-11 and Fig. 3-12. Likewise, full saturation may require a very high partial pressure of water or temperatures too low for practical equilibration.
Finely, it is believed that this is not entirely explicable by kinetics but rather also by slight compositional variations as suggested in Fig. 3-2, by the lattice energy and the basicity of the oxides as suggested in [76] or by a possible influence of elastic stresses as suggested in [77].

The technique used in the present work for the determination of the proton concentration is very easy to carry out. If measuring the water uptake by thermogravimetry on powders [57-63] can avoid long equilibration time, measuring on dense pellets allows to measure specimens under the same conditions than for IS measurements. The conditions for IS measurements are considered in the literature as a crucial issue [57, 59-61, 73-75]. This is confirmed by the tremendous dependence of the proton content on the partial pressure of water in Fig. 3-10. Looking at the water pressure curve, such an increase of partial pressure of water is achieved by an increase of about 6°C of the bubbling water for humidification. It is clear that in case of undefined conditions, the interpretation of the IS results may be drastically affected. Thus, the partial pressure of water used during IS measurements is a parameter that has to be considered to compare different conductivity values from the literature. In the present work, the conditions are considered to be very reproducible. Thus the partial pressure of water could neither explain discrepancies in proton concentration of about several mole percents nor in conductivity values of about several orders of magnitude.
With respect to Eq. 1-2 and considering the results from Fig. 3-11, it is apparent that the kinetics of hydration equilibrium depends on time and temperature of exposure. Hence, at $T \geq 450°C$ (high temperatures), the thermodynamic equilibrium is reached fast. Therefore, the equilibrium is called “true equilibrium”. It is shifted to the left and the concentration of protons is low [78]. On the contrary, at $T < 450°C$ (low temperatures), the kinetics is slow and an apparent equilibrium is reached. In this case,

protons are frozen in or out. There is no exchange with the surrounding atmosphere and the concentration of protons remains constant. Consequently, in order to work with the maximum accuracy, IS measurements are performed with a well-defined proton concentration working: either at constant proton content or at the equilibrium proton concentration.

3.4 Conductivity of $BaZr_{0.9}Y_{0.1}O_{3-\delta}$ and $BaZr_{0.8}Y_{0.2}O_{3-\delta}$

3.4.1 Impedance spectra and data analysis

Fig. 3-14 presents impedance spectra illustrated as Bode plots of BZY10. It shows that over the temperature range 200°C – 600°C up to 3 contributions can be identified. Below 300°C, one contribution appears at high frequencies and a second one at low frequencies. By increasing the temperature, the first contribution cannot be seen anymore in the frequency range 10 Hz to 3 MHz, and the second contribution is clearly shifted to higher frequencies. At 600°C, a third contribution appears at the low frequency end.

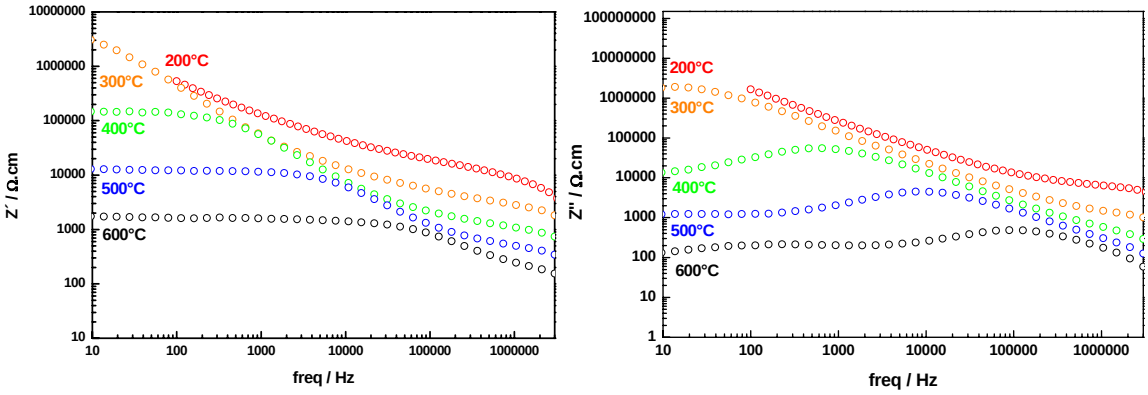

(a) (b)

Fig. 3-14 Bode plots of BZY10 prepared by the solid-state reaction method and sintered at 1720°C, SS1720, presents the real Z´ (a) and the imaginary Z´´ (b) versus the frequency for the temperature range 200°C – 600°C.

One of the first questions to be settled experimentally is: which portion of the Nyquist plot corresponds to the electrode region and what portion corresponds to the electrolyte material? An approach to this question was proposed by Bauerle et al. [79]. It is based on the variation of the geometrical parameter of the sample (either the length of the sample, L, or the electrode surface area, A). The electrolyte equivalent circuit parameters should vary with the factor A/L. In the present work, L was increased by a factor 1.89 while A was kept constant. Fig. 3-15. a and b show the Nyquist plots before and after correction by the geometrical factor. It is apparent that, at 300°C, the two high frequency semicircles depend on the geometrical factor. The resistance and the capacitance of the semicircles at high frequencies are proportional to A/L. In consequence, these contributions to the impedance are attributed to the BZY10 materials. The semicircles at low frequencies appear to be independent to the geometrical factor and are attributed in the following to the electrode contribution.

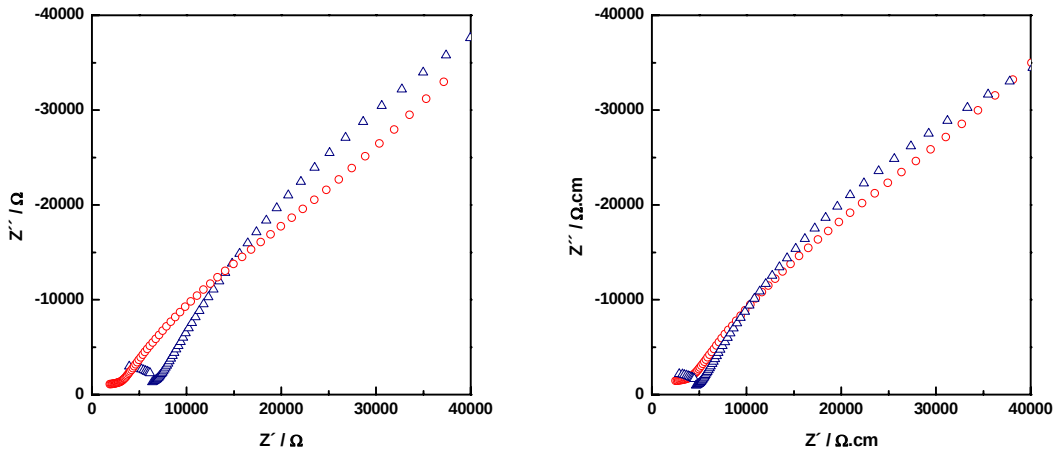

(a) (b)

Fig. 3-15 The Nyquist plots of two specimens annealed at high temperature, ZA2200 (see chapter 6), monitored at 300°C under wet O_2, pH_2O = 2200 Pa, are represented in (a). The same Nyquist plots corrected for the geometrical factor according to Eq. 2-4 are reported in (b).

The modelling of the impedance spectra gives access to the values of the conductivity for the different contributions. The Nyquist representation (Z´´ versus Z´ as parametric functions of the frequency) to be deconvoluted for a BZY10 sample monitored at 300°C under dry conditions is shown in Fig. 3-16. The fitting of the data is illustrated by the red crosses.

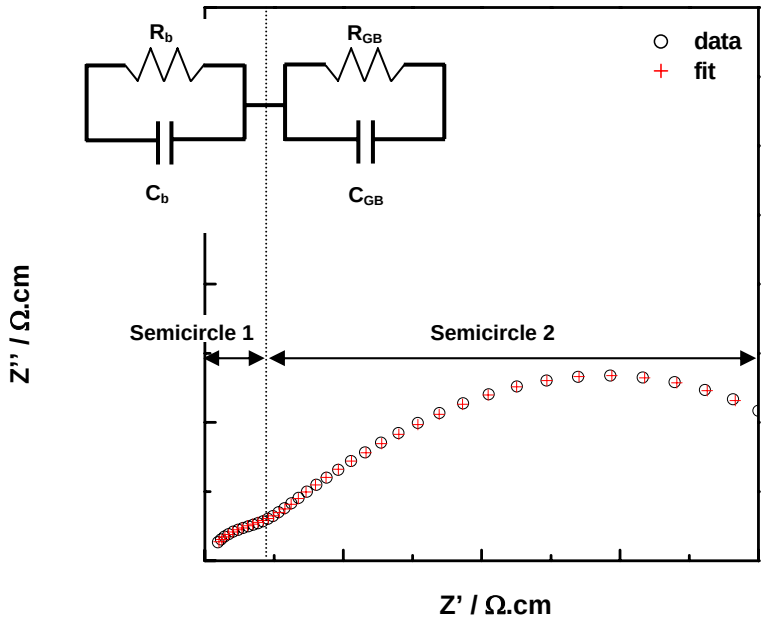

Fig. 3-16 Nyquist plot of BZY10 at 300°C under dry O_2, pH_2O < 10 Pa. The fitting data are represented by red crosses. The equivalent circuit used to fit is $(R_bC_b)(R_{GB}C_{GB})$.

The overall equivalent circuit used in the present work to model the behaviour of the bulk and the grain boundaries corresponds to two RC circuits (a parallel arrangement of resistor and capacitance), one attributed to the bulk and one to the grain boundary contribution to the impedance, in series. In order to attribute the contribution to the bulk and the grain boundaries, the analysis is performed according to the "brick layer model" as described in chapter 2. Based on the order of magnitude of the values for the capacitances, ~ $pF.cm^{-1}$ for the high frequency semicircle and ~ $nF.cm^{-1}$ for the

low frequency semicircle the corresponding resistances can be assigned to the bulk and to the grain boundaries, respectively. The obtained equivalent circuit can be written with the description code : $(R_bC_b)(R_{GB}C_{GB})$

This equivalent circuit fits well (Chi squared ~ 10^{-6}) over the studied temperature range. The Kramers–Kronig data validation is a powerful tool in the deconvolution of impedance data [54]. Fig. 3-17 shows the residuals of a Kramers-Kronig test for the data for BZY10 at 300°C under dry oxygen, pH_2O < 10 Pa. The residuals are randomly distributed around the logarithm of the frequency axis indicating a good match between data and model. This model was also used in previous descriptions in the literature [25, 26, 30, 31].

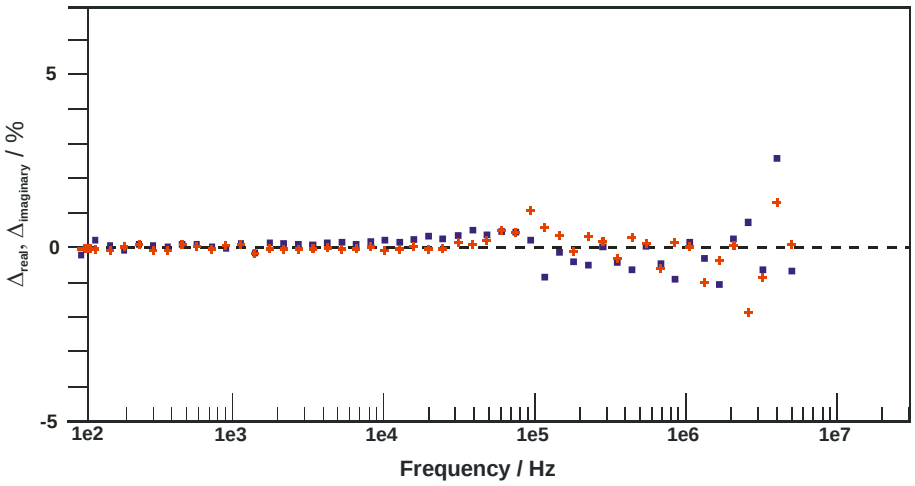

Fig. 3-17 Residuals (red cross: for the real part; blue square: for the imaginary part) of a Kramers-Kronig test for the data on BZY10 at 300°C under dry O_2, pH_2O < 10 Pa.

3.4.2 Temperature dependence of the conductivity

The conductivity of BZY10 was measured isobarically (pH_2O = 2200 Pa, $pO_2 = 10^5$ Pa) over the temperature range 100°C - 900°C. The results are displayed in an Arrhenius plot in Fig. 3-18.

The apparent grain boundary conductivity is about 2 orders of magnitude smaller than the bulk one. The grain boundaries are the limiting contribution at low temperatures

(T < 600°C). At high temperatures (above 600°C), the apparent bulk and grain boundary conductivities become similar.

The bulk conductivity is slightly lower than reported by Schober et al. [25] and Kreuer et al. [30] but about 1 order of magnitude higher than reported by Snijkers et al. [31]. These obvious discrepancies in the bulk conductivity remain unexplained so far.

The apparent grain boundary conductivity found in the present work is similar to the total conductivity of BZY10 reported by Katahira et al. [26]. The specific grain boundary conductivity is even 1 order of magnitude smaller than the apparent grain boundary conductivity, indicating that the amount of grain boundaries may be an important parameter. The grain boundary blocking effect has already been recognized by others [80, 81], but remains not understood so far.

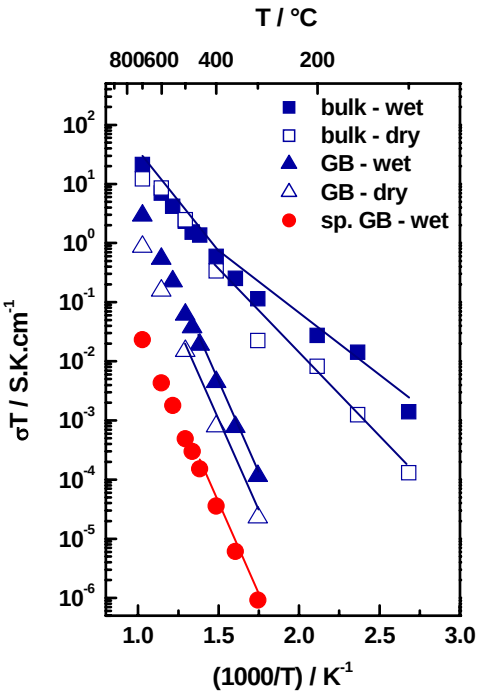

Fig. 3-18 The apparent bulk and grain boundary conductivity and the specific grain boundary conductivity of BZY10 measured under wet O_2, pH_2O = 2200 Pa, and dry O_2, pH_2O < 10 Pa, are plotted in an Arrhenius form.

The conductivity of BZY10 measured under dry conditions is of about 2 orders of magnitude lower for the bulk and about 1 order of magnitude lower for the grain boundary than under wet conditions.

Fig. 3-18 shows that $\ln\sigma T$ is a linear function of 1/T over the temperature ranges 100°C - 400°C and 400°C - 800°C, which indicates an Arrhenius behaviour. An activation energy can then be determined according to Eq. 2-10. The activation energies at temperatures below 400°C are reported in Table 3-2. The activation energy of the bulk conductivity increases from 0.46 eV under wet conditions to 0.60 eV under dry conditions, whereas the activation energy of the grain boundary conductivity is similar for both atmospheres with a value of ~ 1.3 eV.

The pre-exponential factor for the bulk is significantly higher (by a factor 100) under dry conditions than under wet conditions. The pre-exponential factor for the grain boundaries under wet conditions is higher by a factor 1000 than for the bulk and remains constant under dry conditions.

Table 3-2 Activation energy and pre-factor of BZY10 and BZY20 bulk and grain boundary conductivity for temperatures below 400°C.

		Bulk		Grain boundary	
		Ea (eV)	σ_0 (K.S/cm)	Ea (eV)	σ_0 (K.S/cm)
BZY10	Wet O_2	0.46	$2x10^3$	1.21	$5x10^6$
BZY20		0.44	$4x10^3$	0.93	$2x10^5$
BZY10	Dry O_2	0.60	$5x10^4$	1.30	$3x10^6$
BZY20		0.57	$1x10^4$	1.03	$3x10^5$

For comparison, the data for BZY20 are reported in Table 3-2. The activation energies of the conductivity and the pre-exponential factors for BZY10 and BZY20 are similar within the experimental uncertainty under the same conditions.

A difference in conductivity at 300°C for two different Y contents is observed and reported in Table 3-3. The conductivity is found to increase with the yttrium content under both wet conditions, pH_2O = 2200 Pa, and dry conditions, pH_2O < 10 Pa. For the bulk, the difference in conductivity between BZY10 and BZY20 is similar under

both atmospheres (~ 0.44 $S.cm^{-1}$). The theoretically calculated value for the bulk is also reported for comparison in Table 3-3. It is calculated considering the theoretical amount of vacancies and a same mobility for BZY10 and BZY20 (Eq. 1-1 and Eq. 1-2). These experimentally obtained values under wet and dry conditions are higher than the calculated 0.30 $S.cm^{-1}$. The difference in grain boundary conductivities is higher (0.65 $S.cm^{-1}$) under dry conditions than under wet conditions (0.18 $S.cm^{-1}$).

Table 3-3 Difference of the logarithm of the conductivity at 300°C of BZY20 and BZY10 in the bulk and in the grain boundaries.

		Bulk	Grain boundary	Theory
$\log\sigma_{BZY20} - \log\sigma_{BZY10}$	Wet O_2	0.45	0.18	0.30
	Dry O_2	0.43	0.65	

The activation energy of the bulk conductivity is found to be independent of the Y content within the experimental uncertainty. This observation is in agreement with the work from Kreuer et al. [30, 76]. They showed that the enthalpy of the formation and mobility of protonic defects is virtually unchanged by the presence of the substituant. The stability of protonic defects is found to essentially scale with the basicity of the lattice oxygen, which is influenced by both A- and B-site occupations. Despite its significantly higher ionic radius compared to Zr^{4+}, Y^{3+} is found to match perfectly on the Zr-site. Yttrium is an optimal acceptor substituant for $BaZrO_3$, since Mulliken population analysis shows that Y does not change the oxide's basicity [30, 82, 83].

A direct consequence of the dependence of the protonic defect formation on the Y content is that the conductivity increases with the Y content (Table 3-3). This results is consistent with previous results on proton concentration (Fig. 3-9). This observation is also in agreement with the results from Kreuer et al., who found the highest proton conductivities for high Y-dopant concentrations between 15 and 20 mol% [30].

3.4.3 Water partial pressure dependence of the conductivity at the true equilibrium

Fig. 3-19 shows the isothermal dependence of the bulk and grain boundary conductivities on the partial pressure of water for BZY10 at the true equilibrium. For the bulk and the grain boundaries, the conductivity is independent within the experimental uncertainty on the partial pressure of water above 500°C. At 400°C, the conductivities in the bulk and the grain boundaries are significantly lower at pH_2O = 10 Pa than at 2200 Pa.

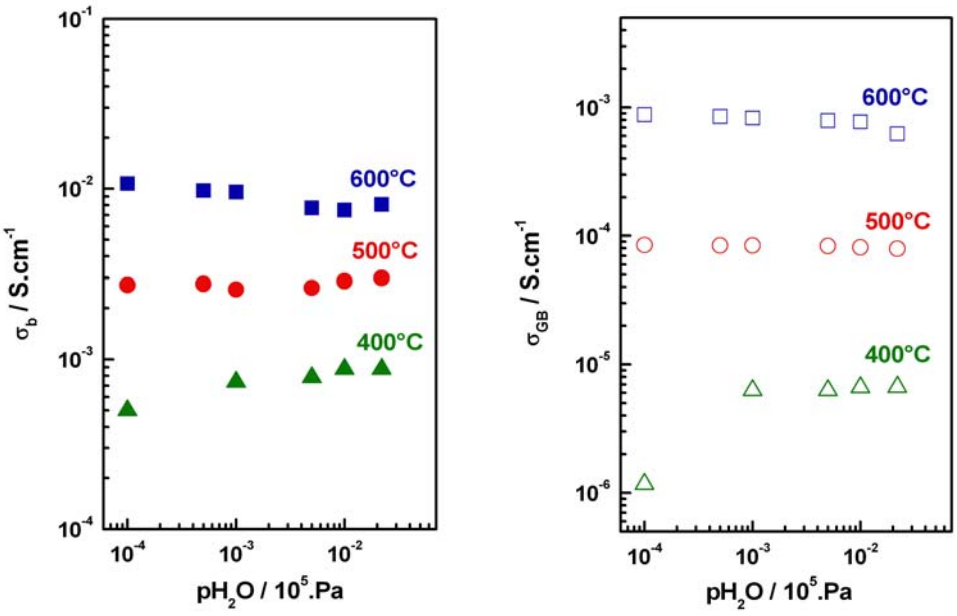

(a) (b)

Fig. 3-19 Dependence of the apparent bulk (a) and grain boundary (b) conductivity on the water partial pressure in O_2 at 400°C, 500°C and 600°C at the true equilibrium for BZY10.

3.4.4 Nature of the bulk conductivity

As shown in Fig. 3-9 to Fig. 3-13, BZY10 dense specimens can be hydrated according to Eq. 1-2. The hydration equilibrium depends on the partial pressure of water, on the concentration of protonic defects and on the concentration of oxygen

vacancies i.e. on the yttrium content (Fig. 3-9). Moreover, the conductivity depends on the partial pressure of water at 400°C as shown in Fig. 3-19. It indicates that the true equilibrium described by Eq. 1-2 is achieved and displaced on the right at low temperatures. In addition, from Fig. 3-18, under an apparent equilibrium, the bulk conductivity of the sample charged with protons is significantly higher than for the dried sample. Furthermore, the activation energy under wet conditions, pH_2O = 2200 Pa, is 0.4 eV, a value typically attributed to proton charge carrier in proton conducting specimens [25, 84]. The increase of the activation energies of the bulk conductivity and the bulk pre-exponential factors between wet and dry conditions is also a direct evidence for proton transport under wet conditions. According to Eq. 1-4, the charge carriers under dry conditions are prominently holes. Finely, the dependency of the conductivity on the Y content is the same under wet and dry conditions (Table 3-2). According to Eq. 1-1, the Y content is a function of the vacancy concentration i.e. the concentration of potential charge carriers. Therefore, it suggests that the bulk conductivity is either dominated by proton charge carriers under wet conditions or dominated by holes under dry conditions. The results from this work indicate proton conductivity in the bulk for T < 450°C. Similar results were already published in the literature [25, 85, 86].

3.4.5 Nature of the grain boundary conductivity

The grain boundaries were found to be blocking (Fig. 3-17). SEM and TEM were performed (Fig. 3-6 and Fig. 3-8, respectively) in order to examine the crystallographic arrangement and potential amorphous phase(s) in the vicinity of the grain boundaries. No evidence of an amorphous phase, which could explain the blocking effect (Fig. 3-18), was found in the grain boundaries. In consequence, it appears more likely that BZY phase itself is responsible for the blocking effect.

In contrast to the bulk, indications of an additional charge carrier to proton arise from the comparison of activation energies. The activation energy depends on the Y content i.e. more Y leads to a reduced activation energy. This result indicates that the nature and/or the mobility of charge carrier are different in the bulk and in the grain boundaries. Moreover, the difference of conductivities between BZY10 and BZY20 is

much smaller under wet than under dry conditions (Table 3-2), whereas it is similar for the bulk under both conditions. According to Eq. 1-4, it indicates that the proton conductivity is not the only charge carrier under wet conditions.

3.5 Proton mobility in $BaZr_{0.9}Y_{0.1}O_{3-\delta}$*

The proton mobility was measured by quasi-elastic neutron scattering (QENS) as described in chapter 2. A representative neutron scattering spectrum versus the energy transfer i.e. S(Q, ω) at 527°C is shown in Fig. 3-20. The fit with a gaussian (elastic), a Lorentzian and linear background scattering contribution is also displayed. It is evident from the spectrum that one single Lorentzian is not sufficient to accurately fit the QENS data. However, only the dominant contribution will be taken into account.

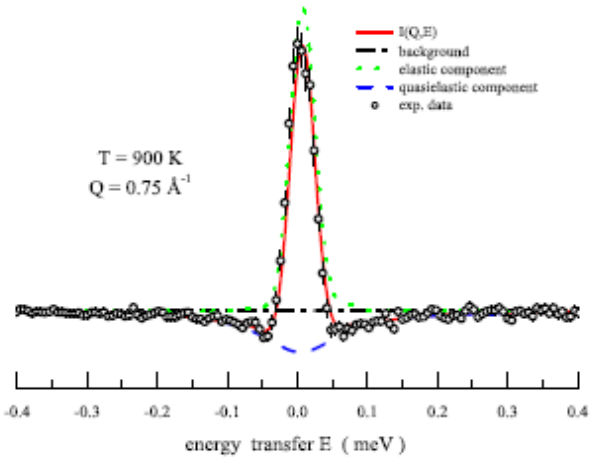

Fig. 3-20 QENS peak with deconvolution in gaussian, lorentzian and linear background.

* *The results are submitted to Journal of Applied Electrochemistry: "Proton diffusivity of $BaZr_{0.9}Y_{0.1}O_{3-\delta}$ proton conductor", A. Braun, S. Duval, P. Ried, J. Embs, F. Juranyi, T. Strässle, U. Stimming, R. Hempelmann, P. Holtappels, T. Graule.*

From the deconvolution of the spectra at different temperatures, Q values and full width at half maximum (FWHM) are determined. We could not unambiguously analyze the QENS data obtained at 227°C and the two data points at $Q^2 = 0.2$ and 0.3 for the data set at 327°C. Fig. 3-21 shows FWHM of the quasielastic peak as a function of Q^2. The FWHM is found to be a linear function of Q^2.

According to the Chudley-Elliott model, the protons move by successive jumps along oxygen ions in the lattice [87]. Proton motion [88] causes an inelastic neutron peak broadening described by Γ(Q), which simplifies for small Q to Eq. 3-1:

$$\Gamma(Q) = 2\hbar DQ^2 \qquad \text{Eq. 3-1}$$

where D is the diffusion constant, Q the scattering angle and ħ the reduced Planck's constant.

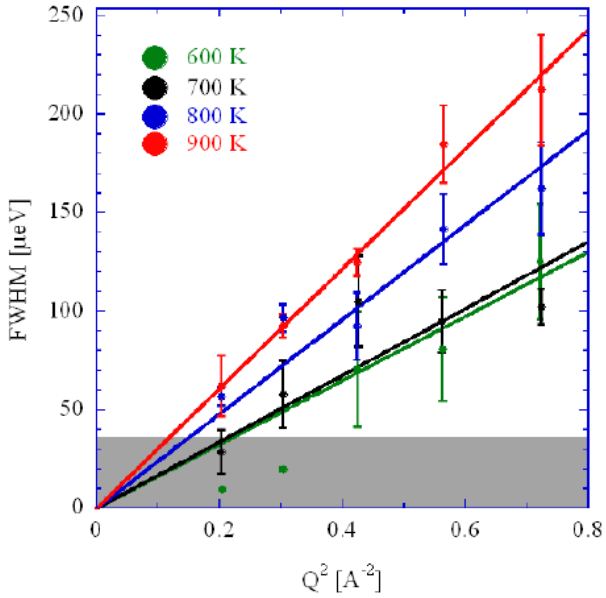

Fig. 3-21 FWHM of the quasi-elastic peak is plotted against Q^2.

According to Eq. 3-1, the slope of the curves is used to determine the diffusion constant. The as obtained diffusion constants are reported in Fig. 3-22. On the same figure, the diffusion constant from IS data and from previous work on $BaZr_{0.9}Y_{0.1}O_{3-\delta}$

[89] are also reported for comparison. The diffusion coefficient from IS data is obtained from Eq. 2-9. It is clearly evident from Fig. 3-22. a that the diffusion constant increases with increasing temperature.

The Arrhenius representation from QENS data in Fig. 3-22. b shows that the proton diffusion between 450°C and 650°C is thermally activated with an energy of Ea = 0.14 eV, whereas below 400°C, the activation energy is only 0.08 eV.

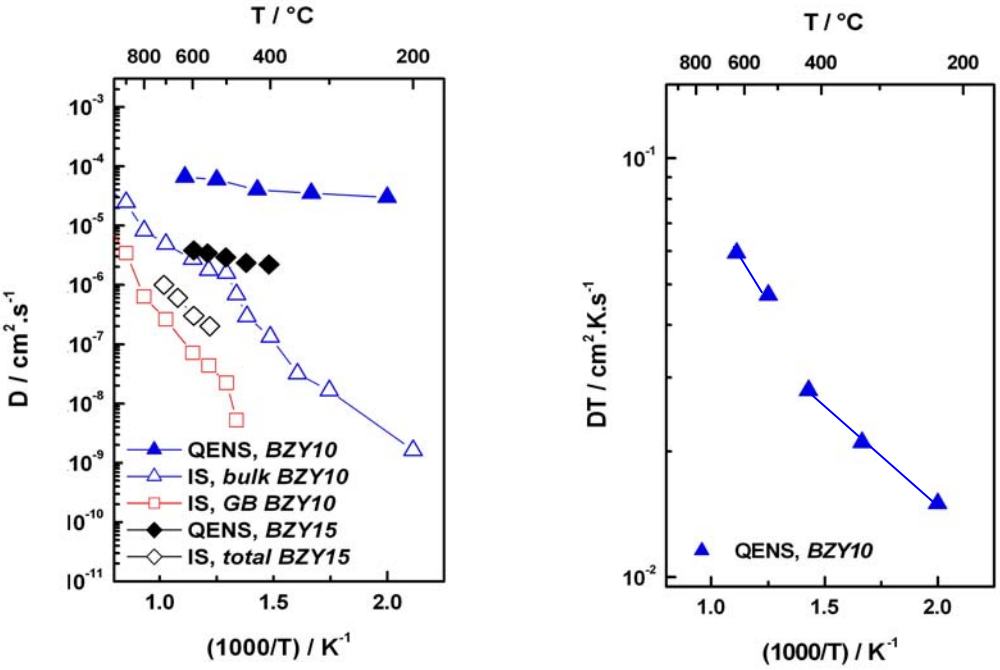

(a) (b)

Fig. 3-22 The diffusion coefficients of BZY10 measured by QENS and by IS are plotted as a function of the temperature (a). Similar results from the literature, [89], on BZY15 are also reported (a). Arrhenius plot of the diffusion coefficient determined by QENS for BZY10 (b).

On a first view the agreement between the diffusivity obtained by QENS and by IS seems to be really poor. The diffusivity measured by QENS reveals more than 100 times faster diffusive processes than obtained by IS. However, IS evaluates an effective diffusion coefficient, whereas QENS detects a chemical one. QENS allows studying the diffusion process simultaneously on a time and space scale on a

microscopic scale. IS is not able to determine such fast processes like strongly localized motions of the protons but only translational long range diffusion.
The QENS diffusion for BZY10 from the present work is about 10 times higher than the results on BZY15 from [89] (Fig. 3-22. a). From the previous results from Table 3-2 and [24], the long range diffusion is independent on the Y content. In contrast, it is likely that on a localized scale, the Y acts as a trap for protons.

3.6 Conclusions

The proton concentration, microstructural, crystallographic and electrical properties were investigated for barium zirconate substituted with different Y content, $BaZr_{1-x}Y_xO_{3-\delta}$ with x = 0, 5, 10, 15 and 20.
Dense (97% of the theoretical density) $BaZr_{1-x}Y_xO_{3-\delta}$ are prepared by compaction of the green body at 200 MPa and sintering at 1720°C. Homogeneous grains with a mean grain size of ~ 1 μm are obtained.
The lattice parameter increases with the Y content after sintering. After calcinations, the lattice parameter is independent of the Y content, suggesting that the degree of reaction can be detected by XRD.
$BaZr_{1-x}Y_xO_{3-\delta}$ samples incorporate protons. A proton content close or slightly lower than the theoretical limit can be achieved. An increasing proton concentration with the Y content is observed for $BaZr_{1-x}Y_xO_{3-\delta}$ dense specimen.
Measurements by impedance spectroscopy were performed with a well-defined proton concentration working either at constant proton content i.e. at low temperatures or at the equilibrium proton concentration i.e. at high temperatures. The bulk and the grain boundary contributions were separated. The bulk conductivity is dominated by proton transport and shows high conductivity values. The grain boundaries are the limiting contribution to the total conductivity. Determining the reasons of their large resistivity and the nature of the charge carriers is a major issue, which is investigated in the following chapters. The Y content affects the bulk conductivity but not the activation energy suggesting that the concentration of proton charge carrier is changed but the proton transport mechanism remains similar.

To conclude with, the properties of $BaZr_{1-x}Y_xO_{3-\delta}$ are consistent for x = 0, 5, 10, 15 and 20. To investigate further the transport mechanism, any $BaZr_{1-x}Y_xO_{3-\delta}$ with x = 0, 5, 10, 15 and 20 could serve. Thus, it was chosen to perform the following investigations on $BaZr_{0.9}Y_{0.1}0_{3-\delta}$.

CHAPTER 4

Influence of the Synthesis Method on the Properties of $BaZr_{0.1}Y_{0.9}O_{3-\delta}$

As shown in chapter 3, BZY10 has a fast bulk proton conductivity. But the very poor grain boundary conductivity of this material is a major problem. The grain growth of ceramics is in general controlled by the sintering temperature. In the case of BZY10 powders synthesised by the solid-state reaction method, even a high sintering temperature (> 1700°C) does not deliver a material with an appropriate morphology to obtain good performances. Another way to control the grain growth is to tune the powder morphology. Since the soft chemistry routes generally provide finer powders compared to the solid-state reaction method, they may offer a way of decreasing the sintering temperature.

In this respect, $BaZrO_3$ substituted with various Y content was synthesised recently by a matrix trapping and decomposition method, and a polyacrylamide gel route [32]. A lot of work [35, 37, 42, 90-95] has also already been done on $BaZrO_3$ in the field of dielectric materials using the spray drying, the oxalate, the acrylamide gelification and the peroxide routes. The incorporation of 10 mol. % Y into this perovskite may have an impact on the powder characteristics and thus may affect the sinterability. In addition, these previous works have never investigated the spray pyrolysis method, which appears to be promising for the fine tuning of the morphology of oxide powders

[39]. Therefore, the preparation of BZY10 by (1) the solid-state reaction method, (2) spray drying, and (3) spray pyrolysis is described in the present chapter. The obtained powders and pellets are characterised and the resulting microstructural, crystallographic and electrical properties of BZY10 are compared in the following.

4.1 Crystallography and microstructure of $BaZr_{0.9}Y_{0.1}O_{3-\delta}$ prepared by the different synthesis routes

4.1.1 Properties of powders

The temperature required for the formation of BZY10 can be deduced from the thermal analyses of the three different powders as shown for the solid-state, spray drying and spray pyrolysis routes in Fig. 4-1, Fig. 4-2 and Fig. 4-4 respectively. The temperature and the mechanism for the formation of a pure BZY10 depend on the nature of the precursors and on the spraying temperature and technique. For the solid-state reaction route, the exothermic DTA peak at 1083°C accompanied with a peak at *m/z* 44 corresponds to the maximum decomposition rate of $BaCO_3$. The simultaneous large one-step weight loss indicates the reaction between the different precursors.

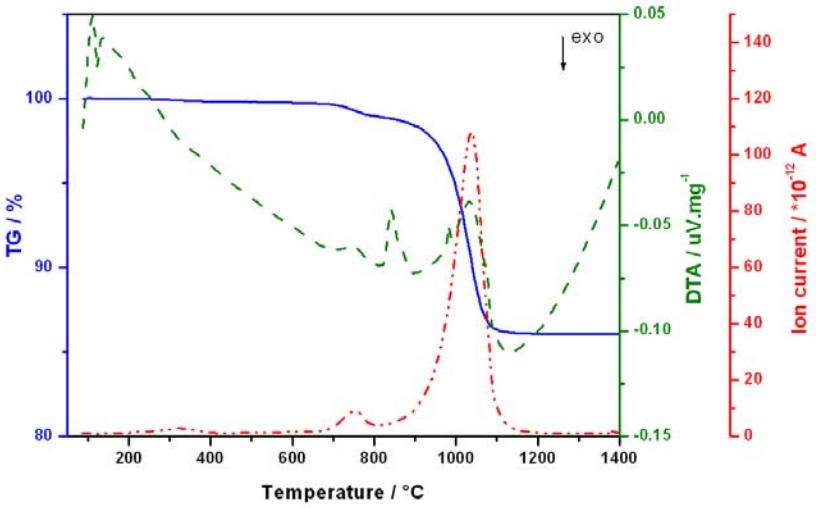

Fig. 4-1 Thermal analysis of the mixed oxides powder: mass loss (full line), energy loss (dash line), and ion current for *m/z* 44 (dash-point line).

For the spray drying route, the continuous weight losses up to 470°C accompanied by exothermic transitions are attributed to the loss of the lattice water of the zirconyl nitrate and the yttrium nitrate. The peak at 598°C typically corresponds to the decomposition of $Ba(NO_3)_2$ (melting point ~ 592°C) [90]. The large weight loss together with a DTA peak between ~ 560°C and ~ 640°C indicates the decomposition and the reaction of the nitrate precursors. A small but significant mass loss (0.1%) is observed between 800°C and 1200°C. This mass loss is accompanied by a peak at *m/z* 44, which corresponds to CO_2. Therefore, the decomposition process of $Ba(NO_3)_2$ might involve partially the formation of $BaCO_3$.

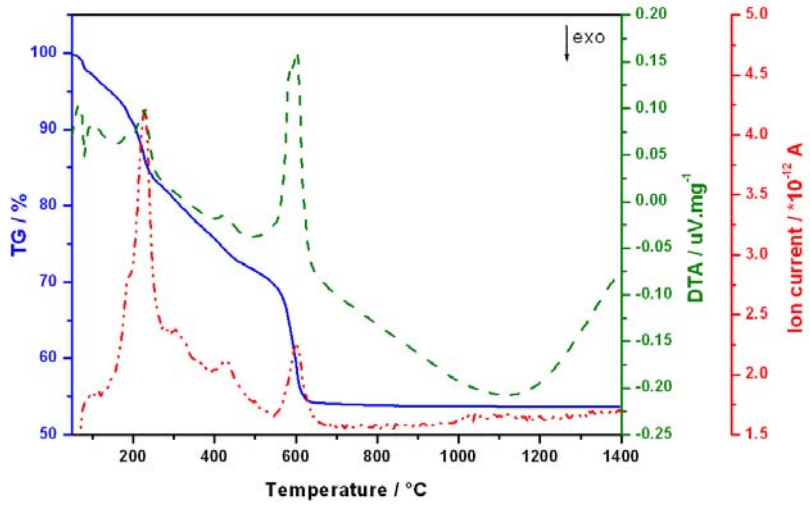

Fig. 4-2 Thermal analysis of the spray dried powder: mass loss (full line), energy loss (dash line), and ion current for *m/z* 44 (dash-point line).

Fig. 4-3 shows the XRD diffractograms of BZY10 synthesised by the spray drying method and calcined at 800°C for 2, 4 and 10 hours. The main peaks are indexed to BZY10. The presence of $BaCO_3$ is also indicated in the all XRD patterns. Additional peaks can be indexed to $Zr_{0.952}O_2$ and BaO_2.

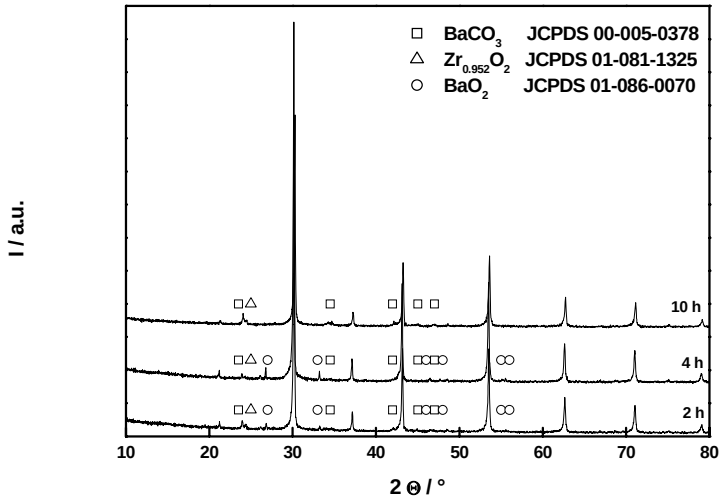

Fig. 4-3 XRD diffractograms of BZY10 synthesised by the spray drying route and calcined at 800°C for 2, 4 and 10 hours.

For the spray pyrolysis route, no mass loss is observed below 550°C (which is the pyrolysis temperature) suggesting that the zirconyl and the yttrium nitrate were partially decomposed in the pyrolysis furnace (Fig. 4-4).

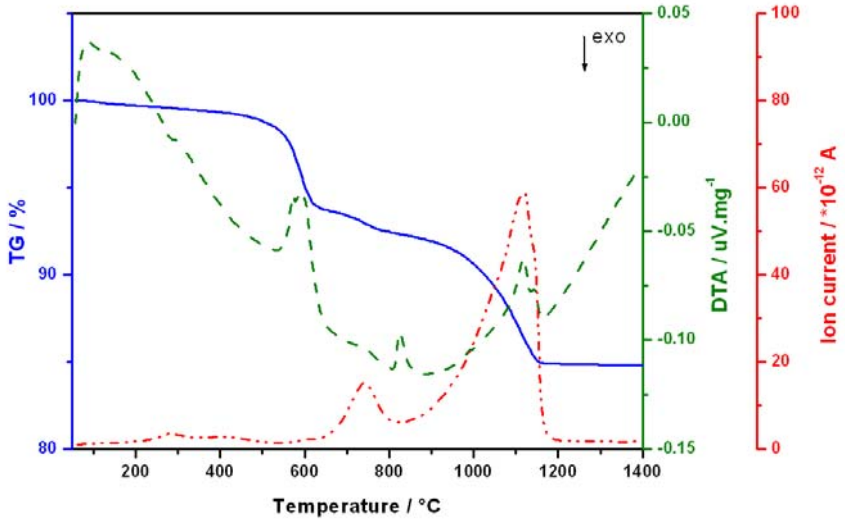

Fig. 4-4 Thermal analysis of the spray pyrolysed powder: mass loss (full line), energy loss (dash line), and ion current for *m/z* 44 (dash-point line).

The decomposition of $Ba(NO_3)_2$ takes place at higher temperatures ($T_{decomp} \sim 598°C$) like for the SD route. The most prominent mass loss occurs at 1117°C and CO_2 is released indicating that $BaCO_3$ is formed before it reacts with ZrO_2.

In the following, all powders were calcined at 1200°C for 10 hours. The XRD patterns from the resulting calcined powders for the different routes are presented in Fig. 4-5. This figure shows that at 1200°C a phase pure BZY10 is obtained for the three synthesis methods.

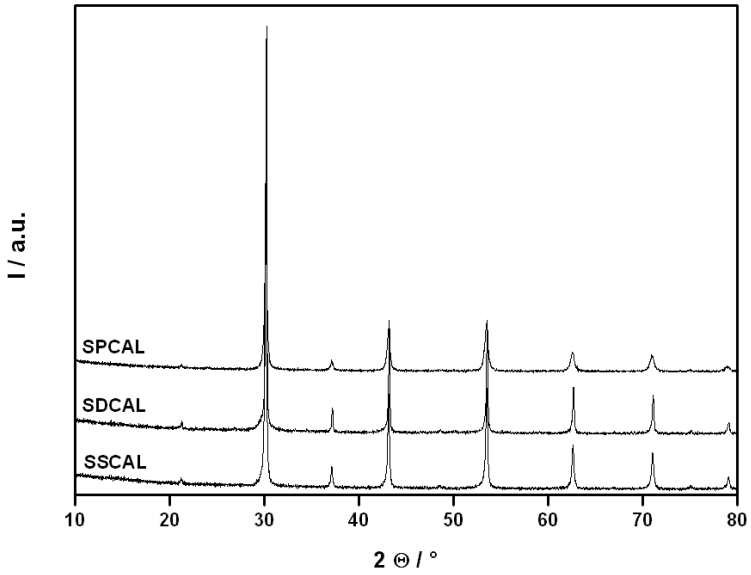

Fig. 4-5 X-ray diffraction patterns of the powder prepared by the solid-state reaction route, SSCAL, the spray drying, SDCAL, and the spray pyrolysis, SPCAL and calcined at 1200°C for 10 hours.

A deeper analysis of the resulting phases with respect to the symmetry group and the lattice parameters was performed. The phase is found to be cubic for all powders. The lattice parameters are presented in Table 4-1. Variations of the lattice parameter around 0.4193 nm are observed depending on the synthesis method.

Table 4-1 Lattice parameter of the calcined powders prepared by the different synthesis methods.

Sample	Method	Calcination (T/°C-t/h)	a (nm)	V_{cell} ($10^{-30}m^3$)
SSCAL	Solid-state reaction	1200-10 + 1400-10	0.4193	73.71
SPCAL	Spray pyrolysis	1200-10	0.4196	73.87
SDCAL	Spray drying	1200-10	0.4189	73.51

It is obvious from SEM pictures shown in Fig. 4-6 that different morphologies (e.g. evaluated apparent grain and the agglomerate sizes presented in Table 4-2) result from the different methods. The calcined solid-state powder shows very small crystallite sizes, whereas the agglomerates are around 24 μm after milling (Fig. 4-6). The surface area measured by BET is 4.8 m^2/g. The spray pyrolysed powder calcined at 1200°C is partially sintered (Fig. 4-6), with a BET surface area of 2.5 m^2/g. An explanation can be that the precursors are intimately mixed during the process and in consequence reaction and crystallite growth is occurring during spraying. The particles of the calcined spray dried powder show a cubic shape after calcination with a grain size of 1 mm (Fig. 4-6). The BET surface area is 3.6 m^2/g, which is consistent with the evaluated grain size.

Table 4-2 Powder morphology of the calcined and milled powders prepared by the different synthesis methods.

Method	Aggregate size (μm)	Grain size (μm)	BET surface area (m^2/g)
SSCAL	24	-	4.8
SPCAL	32	<0.6	2.5
SP	10	<0.6	-
SDCAL	37	<1	3.6
SD	50	<8.5	-

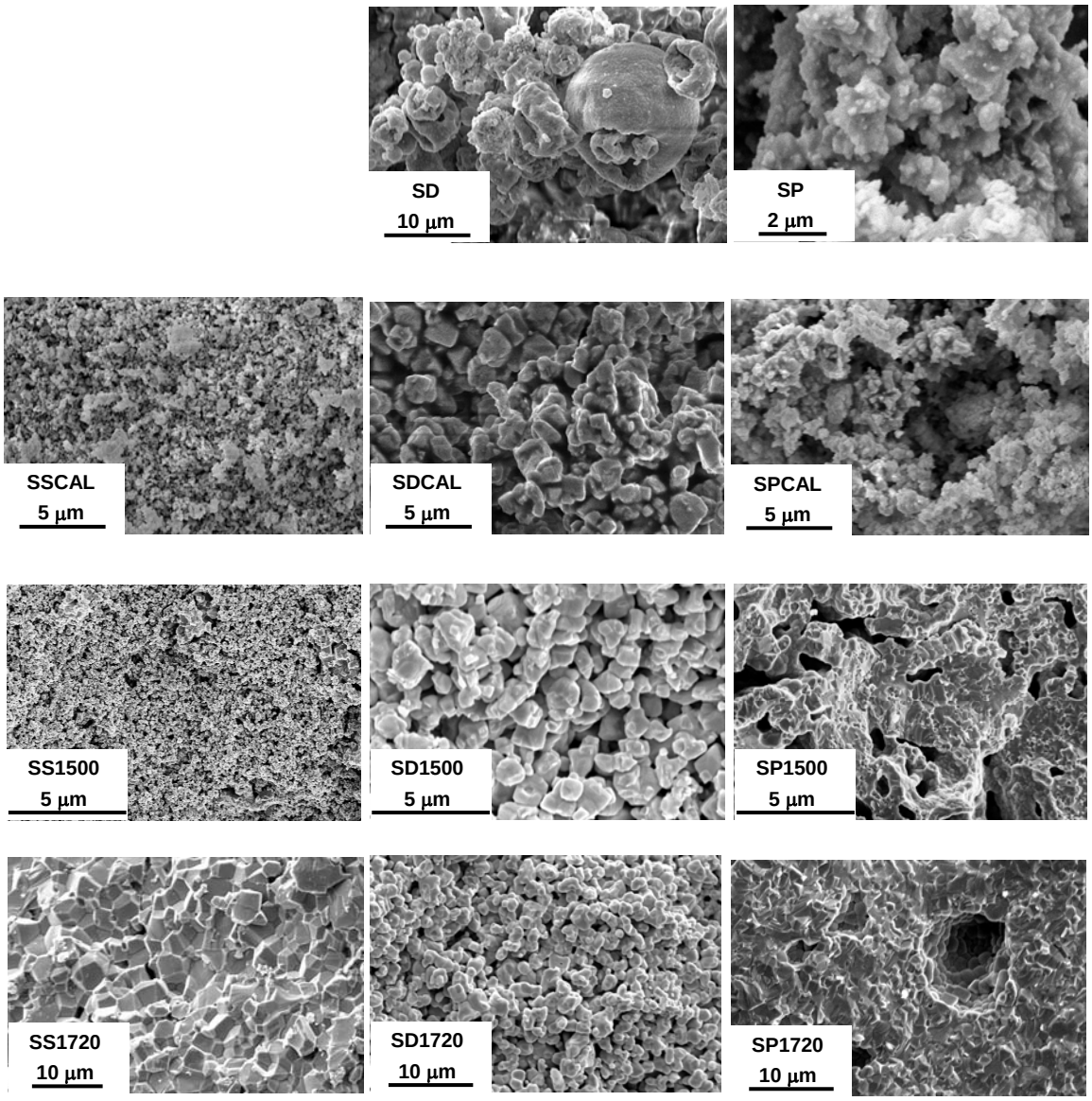

Fig. 4-6 SEM pictures of the differently prepared powders and of the sintered specimens at 1500°C and 1720°C.

4.1.2 Properties of massive specimens

The differently prepared BZY10 powders were sintered at 1500°C and 1720°C, which are the common sintering temperatures reported in the literature [25, 30, 61]. XRD patterns obtained from the sintered bodies show a phase pure BZY10 but also present peak shifts compared to the calcined powders. The lattice parameters for the sintered bodies as a function of the sintering temperatures are presented in Table 4-3. BZY10 prepared by the different methods and sintered at 1500°C and at 1720°C were found to have a cubic structure except the SS1500 sample prepared by the solid-state reaction route and sintered at 1500°C. In this specimen an additional BZY10 phase was identified, which can be described as tetragonal.

Table 4-3 Lattice parameter of the sintered pellets prepared by the different synthesis methods.

Sample	Method	Thermal history		a=b=c (nm)	V_{cell} ($10^{-30}.m^3$)	Theorit. density (g/cm^3)
		Calcination (T/°C-t/h)	Sintering (T/°C-t/h)			
SS1500	Solid-state reaction	1200-10 + 1400-10	1500-10	0.4192 and a=b=0.4202 c=0.4220	73.66 74.58	6.24 6.26
SS1720			1720-24	0.4206	74.34	6.18
SP1500	Spray pyrolysis	1200-10	1500-10	0.4202	74.20	6.18
SP1720			1720-24	0.4192	73.65	6.24
SD1500	Spray drying	1200-10	1500-10	0.4196	73.88	6.22
SD1720			1720-24	0.4197	73.95	6.23

Compared to the calcined powders, the lattice parameters after sintering are increased. The values vary with the powder fabrication method and the sintering temperatures (1500°C and 1720°C). The lattice parameters of the samples prepared by the nitrate routes are smaller (≤0.4202 nm) than the one of the SS1720 sample prepared by the solid-state reaction route sintered at 1720°C (0.4206 nm).

The microstructure of a fracture cross section of the sintered specimens is shown in Fig. 4-6. The sample prepared by the solid-state reaction route sintered at 1720°C,

SS1720, is dense, with a density of about 94% of the theoretical density (Table 4-4). A distinct grain growth and a decreased porosity are observed during sintering between 1500°C and 1720°C. For the samples synthesised by spray pyrolysis and spray drying, an improvement of the density is also observed with an increasing sintering temperature. A limited grain growth as well as an important increase in the pore size occurs for the spray pyrolysed sample. The calcined spray dried powder shows an apparent grain size of 1-2 micrometers, which remains during sintering up to 1720°C. Looking closer to the fracture cross sections, intergranular cracking is indicated for the solid-state and the spray dried samples sintered at 1720°C. For the SP1720 sample, intragranular cracking is likely.

Table 4-4 Grain size, pore size and percentage of the theoretical density of the pellets prepared by the different synthesis methods.

Sample	Grain size (μm)	Pore size (μm)	Percentage of the theoretical density (~ 6.2 g/cm^3)
SS1500	<0.1	<0.2	64 %
SS1720	~ 2	<0.7	94 %
SD1500	<1	<1	50 %
SD1720	<1	<1	59 %
SP1500	<0.7	<0.7	68 %
SP1720	~ 1	<4	73 %

4.2 Conductivity of $BaZr_{0.9}Y_{0.1}O_{3-\delta}$ prepared by different synthesis routes

4.2.1 Temperature dependence of the conductivity

Bode Z′-Z′′ plots at 300°C for specimens synthesised by the different preparation methods are presented in Fig. 4-7. Following the temperature dependence of the impedance, bulk and grain boundary contributions could be separated as described in chapter 3 for all materials investigated.

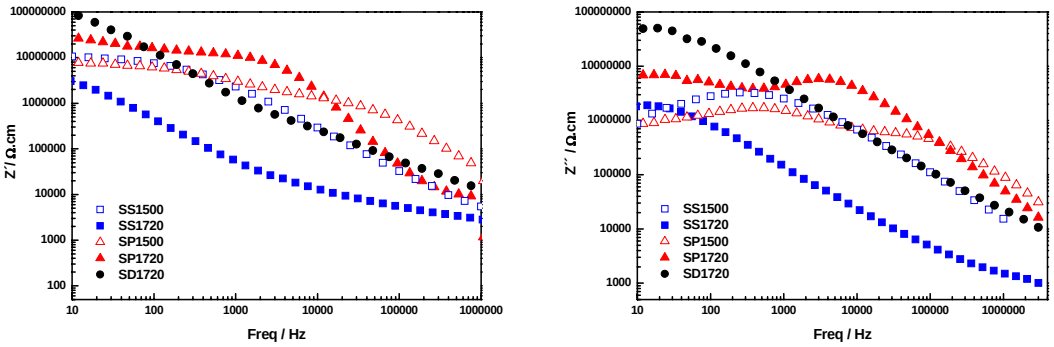

(a) (b)

Fig. 4-7 Bode plots of the real, Z´, (a) and of the imaginary, Z´´, (b) for the specimens prepared by the solid-state reaction method and sintered at 1500°C (SS1500) and 1720°C (SS1720), by the spray pyrolysis at 1500°C (SP1500) and 1720°C (SP1720) and by the spray drying at 1720°C (SD1720). The measurements were performed at 300°C under wet O_2, pH_2O = 2200 Pa.

The temperature dependence in the range 150°C - 700°C of the bulk conductivity of BZY10 under wet oxygen, pH_2O = 2200 Pa, is shown in Fig. 4-8. a. The sample prepared by the solid-state route and sintered at 1720°C, SS1720, has a bulk conductivity, which is more than 1 order of magnitude higher than the one of the specimen sintered at 1500°C, SS1500, and of the samples synthesised by spray pyrolysis and spray drying.

The activation energies and the pre-exponential factors of the bulk conductivities are determined from Fig. 4-8 and reported in Table 4-5 for the different synthesis routes and sintering temperatures. The activation energy is determined for T < 400°C, except for the bulk of the specimen SS1500. The ratio of the capacitances of the bulk and the grain boundaries is used for the calculation of the specific grain boundary conductivity. The activation energy for the solid-state sample sintered at 1720°C, SS1720, is the lowest with 0.46 eV, whereas the pyrolysed sample sintered at 1500°C, SP1500, and the spray dried one sintered at 1720°C, SD1720, result in similar activation energies around 0.60 eV. The spray pyrolysed sample sintered at 1720°C,

SP1720, has the highest activation energy of 0.80 eV. All pre-exponential factors are similar (around $2x10^3$ K.S/cm).

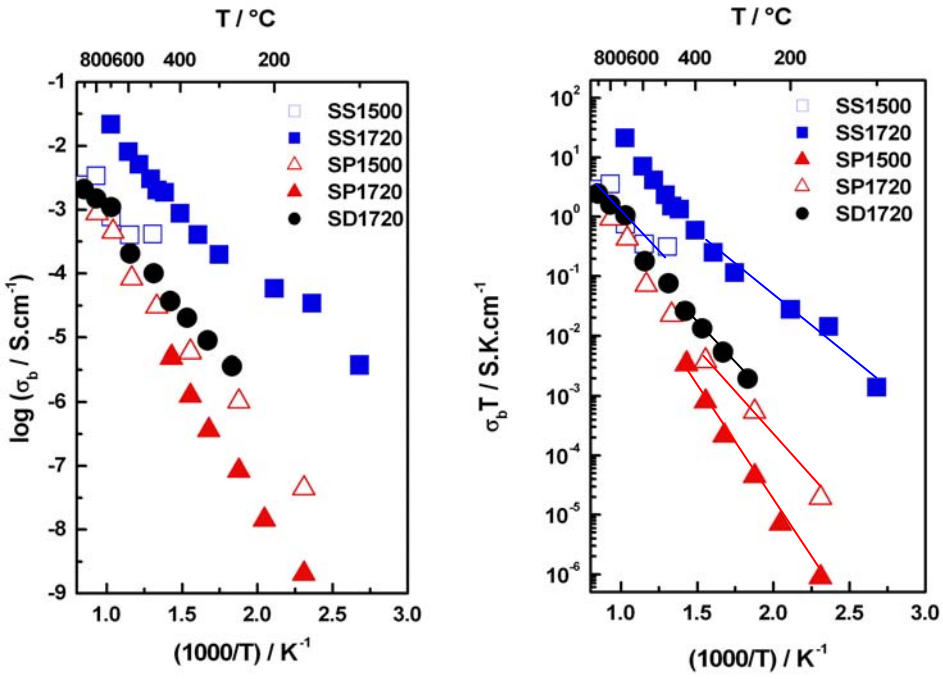

(a) (b)

Fig. 4-8 Bulk conductivity of BZY10 synthesised by the solid-state reaction method and by the spray pyrolysis method, sintered at 1500°C and 1720°C and by the spray drying method sintered at 1500°C (a). The results are presented in $\sigma_b T$ plot (b)

Table 4-5 Activation energies and pre-exponential factors of the bulk and the grain boundary conductivity for BZY10 prepared by the different synthesis methods.

Sample	Bulk		Grain boundary			C_b/C_{GB}
	E_a (eV)	σ_0 (K.S/cm)	E_a (eV)	σ_0 (K.S/cm)	$\sigma_{0\text{-sp. GB}}$ (K.S/cm)	
SS1500	0.64	$2x10^3$	1.19	$5x10^5$	-	-
SS1720	0.46	$2x10^3$	1.21	$5x10^6$	$5x10^4$	$7.8x10^{-3}$
SD1500	-	-	-	-	-	-
SD1720	0.66	$2x10^3$	0.98	$2x10^3$	$1x10^3$	$8.4x10^{-1}$
SP1500	0.60	$1x10^3$	0.75	$1x10^3$	$4x10^1$	$4.2x10^{-2}$
SP1720	0.80	$2x10^3$	0.83	$1x10^3$	$8x10^1$	$1.4x10^{-2}$

The temperature dependence of the apparent grain boundary conductivity is presented in Fig. 4-9. a. The apparent grain boundary conductivity is found to vary over 1 order of magnitude between the different samples. The difference in apparent grain boundary conductivities between the different samples at one temperature is not smaller than for the apparent bulk conductivity.

Using the ratio between the capacitances from Table 4-5, the specific grain boundary conductivity, $\sigma_{sp.\ GB}$ can be calculated according to Eq. 2-6. The specific grain boundary resistances for the differently synthesised and sintered specimens are shown in Fig. 4-9. b. $\sigma_{sp.\ GB}$ varies only over less than 0.5 orders of magnitude (Fig. 4-9. b).

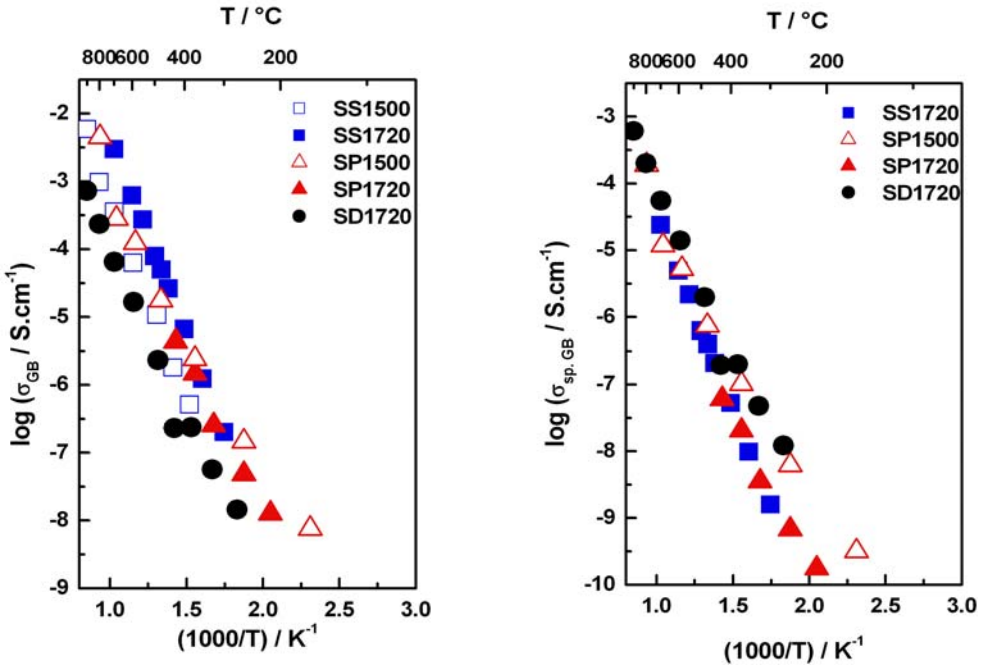

(a) (b)

Fig. 4-9 Apparent (a) and specific (b) grain boundary conductivity of BZY10 synthesised by the solid-state reaction method and by the spray pyrolysis, sintered at 1500°C and 1720°C and by the spray drying sintered at 1500°C.

The temperature dependence of the apparent grain boundary conductivity reveals further differences between the variously prepared samples: the activation energies scatter from 0.84 to 1.21 eV (the data are evaluated from Fig. 4-10 and are reported in Table 4-5). The apparent grain boundary activation energies are similar for the spray pyrolysed and spray dried specimens and amount to ~ 0.9 eV, whereas the activation energies for the solid-state specimens are significantly higher with 1.2 eV. A clearer trend is observed for the pre-exponential factor for the specific grain boundary conductivity, $\sigma_{0\text{-sp. GB}}$: namely the solid-state prepared specimen shows a $\sigma_{0\text{-sp. GB}}$ value around 10^5 K.S/cm, while all other samples show pre-exponentiel factors between 10 and 10^3 K.S/cm.

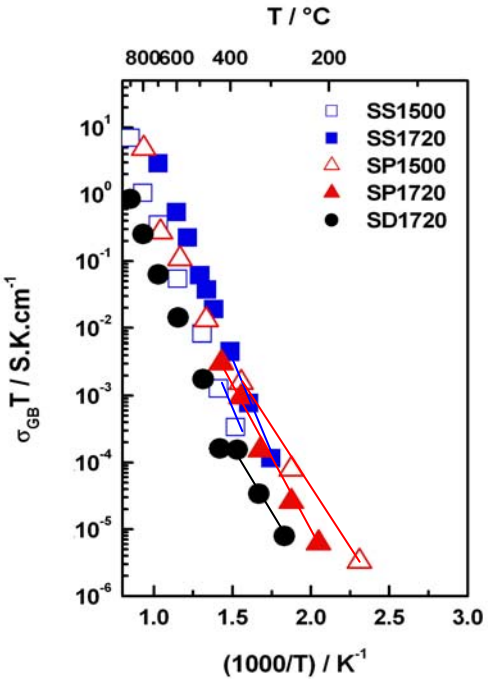

Fig. 4-10 Arrhenius plot the apparent grain boundary conductivity of BZY10 synthesised by the solid-state reaction method and by the spray pyrolysis, sintered at 1500°C and 1720°C and by the spray drying sintered at 1500°C.

4.2.2 Water partial pressure dependence of the conductivity

Fig. 4-11 shows the bulk conductivity at 300°C under wet O_2, $pH_2O = 2200$ Pa, and dry O_2, $pH_2O < 10$ Pa, for the differently prepared specimens. The data plotted here are obtained from isobarical measurements. For all samples, the conductivity under wet conditions is found to be at least half an order of magnitude higher than under dry conditions. The difference in conductivity is found to be the largest for the pyrolysed sample sintered at 1720 °C, SP1720, and the lowest for the pyrolysed sample sintered at 1500°C, SP1500.

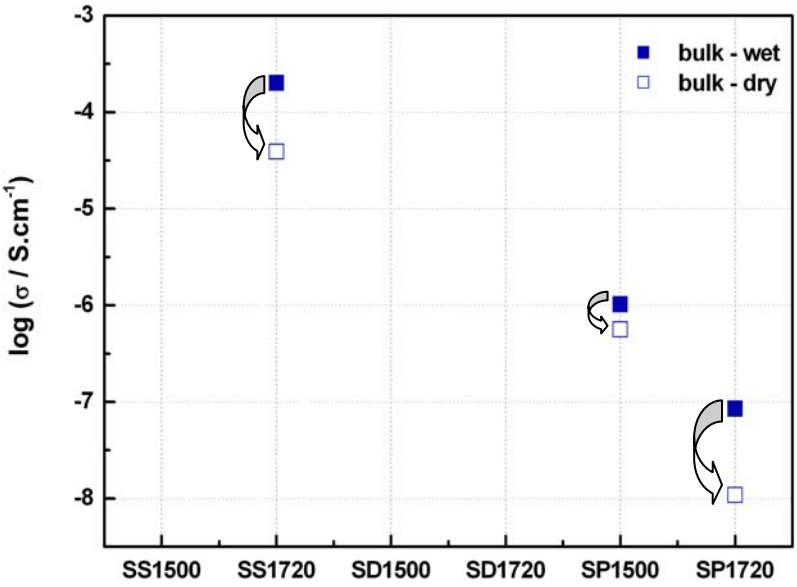

Fig. 4-11 Conductivity of the bulk at 300°C under wet O_2, pH_2O = 2200 Pa, and dry O_2, pH_2O < 10 Pa, for the differently prepared specimens.

4.3 Discussion on the influence of the synthesis route on the crystallography of $BaZr_{0.9}Y_{0.1}O_{3-\delta}$

Regarding the choice of an adequate calcination temperature, the TGA-DTA+MS gives helpful information. DTA and TG curves in Fig. 4-1, Fig. 4-2, and Fig. 4-4 show obvious differences. Thus, it is apparent that the mechanism of formation of BZY10 depends on the precursors used. The intermediate formation of $BaCO_3$ from the nitrate precursors of barium is obvious for the spray drying and spray pyrolysis routes (Fig. 4-2 and Fig. 4-4 respectively). The presence of carbonate species has important implications for the preparation of BZY10 dense bodies. Carbon dioxide, which is released during the decomposition of $BaCO_3$, might induce pores or cracks during sintering and prevent, therefore, from complete densification of the material as demonstrated by Sin et al. [42].

In addition, the asynchronous reaction of barium containing compounds with the other precursors may lead to a non homogeneous stoichiometry. Magrez et al. [32] show for $BaZr_{0.8}Y_{0.2}O_{3-\delta}$ synthesised by the solid-state reaction method that there is an optimal calcination temperature of 1250°C leading to the highest degree of phase purity. It is likely that the powders, all sintered in the present work at 1200°C, remain partly non-homogenous. A direct observation of this effect is the two distinct phases for the sample prepared by the solid-state method and sintered at 1500°C (Table 4-3). Others already suggest the possible co-existence of two phases, with slightly different lattice parameters [30, 96]. Recent neutron diffraction data suggest [97] that there are two cubic phases present in the material. The α-form exhibits a slightly smaller unit cell and the β-form has a larger lattice parameter. The ratio of these two phases depends on the processing (precursors, temperature…). The results indicate that this difference originates from a small degree of cross substitution of the Y atom onto the A-sites leading to the β-form as suggested by Eq. 4-1.

$$Ba_{Ba}^{x}(Zr_{Zr_{(1-x)}}^{x}Y_{Zr_{x}}^{\cdot})(O_{O_3}^{x}V_{O_{x/2}}^{\bullet\bullet}) \Leftrightarrow (Ba_{Ba_{(1-y)}}^{x}Y_{Ba_{y}}^{\bullet})(Zr_{Zr_{(1-x)}}^{x}Y_{Zr_{(x-y)}}^{\cdot})O_{O_3}^{x} + Ba_{y}$$
$$\Leftrightarrow (Ba_{Ba_{(1-y)}}^{x}V_{Ba_{y}}^{\prime\prime})(Zr_{Zr_{(1-x)}}^{x}Y_{Zr_{(x-y)}}^{\cdot})(O_{o_3}^{x}V_{O_{(x/2+y)}}^{\bullet\bullet}) + Ba_{y} \qquad \text{Eq. 4-1}$$

Our initial hypothesis (chapter 3) was that the completion of the BZY10 formation reaction occurs during the sintering, and not during the calcination. However, the phase formation is different depending on the powder fabrication. The specimens prepared by the solid-state reaction method required a high and long thermal treatment, whereas the samples prepared from precursors in solutions are equilibrated at lower temperature. Therefore, these observations suggest rather that the larger lattice parameters are found in better equilibrated samples.

4.4 Discussion on the influence of the synthesis route on the bulk properties of $BaZr_{0.9}Y_{0.1}O_{3-\delta}$

4.4.1 Nature of the charge carrier

It was concluded in chapter 3 that the samples prepared by the solid-state reaction route sintered at 1720°C, SS1720, show proton conductivity in the bulk. As the conductivities for the differently prepared samples vary over more than 1 order of magnitude (Fig. 4-8) and activation energies range from 0.4 eV to 0.8 eV (Table 4-5), the nature of the charge carrier of the specimens prepared by the spray drying method and the spray pyrolysis need to be clarified as well. For all specimens, the conductivity under dry conditions, $pH_2O < 10$ Pa, was found to be lower than under wet conditions, $pH_2O = 2200$ Pa, as illustrated at 300°C in Fig. 4-11. Furthermore, the pre-exponential factors are similar for all samples (Table 4-5). Hence, it reasonable to assume that the bulk conductivity for the different samples is considered dominated by protonic charge carriers. All samples are considered proton conductors.

4.4.2 Influence of the microstructure/crystallography on the conductivity

In general, it is expected that different microstructures (e.g. porosity…) result in different bulk conductivities, since the conductivity depends on the effective volume of the materials (without pores). Therefore, it is expected that differences in density from 54% to 94% affect the conductivity. However, this difference in porosity is not likely to explain the observed difference of the bulk conductivities of more than 1 order of magnitude. According to Eq. 2-5, the different porosities may change the conductivity of about a factor of ~ 0.5 (i.e. a shift in $\log\sigma$ of -0.3), which is much smaller than what is observed in this work.

In order to better understand the correlation between the preparation and the electrical properties, the bulk conductivity and the bulk activation energy were plotted in Fig. 4-12. a and b as a function of the lattice parameter. The increase in the bulk conductivity with the lattice parameter is a striking feature: a change of 0.012 Å

increases the conductivity by 2.5 orders of magnitude. An even better correlation is observed for the bulk activation energy, since the pre-exponential factors remain almost constant for all specimens.

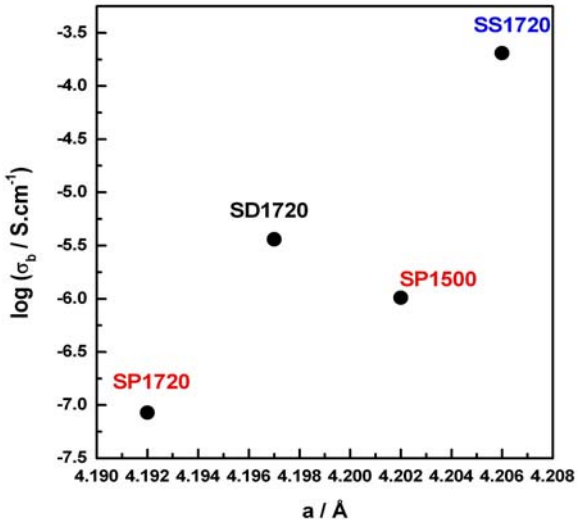

(a)

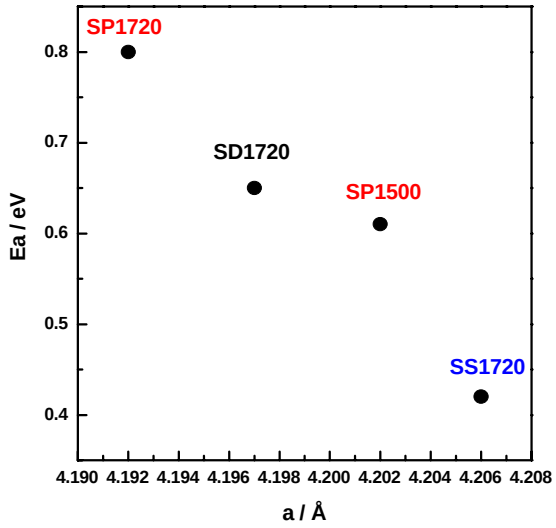

(b)

Fig. 4-12 The lattice parameter of BZY10 as a function of the bulk conductivity at 300°C (a) and as the activation energy of the bulk conductivity (b) for the powders prepared by the spray pyrolysis, the spray drying and the solid-state reaction method sintered at 1720°C and the specimen prepared by the spray pyrolysis and sintered at 1500°C presented.

It is found experimentally that the activation energy decreases with the lattice parameter. This observation was already derived from quantum molecular dynamics simulation by Kreuer [24] and Münch et al. [84]. They show that protonic defects in cubic perovskite-type oxides have typically activation energies varying in the range from 0.4 to 0.8 eV depending on the interaction, which controls the proton transport. According to the transition state theory, the activation energy can be related to an activated complex formed during the proton transfer process. The results indicate that efficient proton jumps are then enabled by large O-O distances i.e. powerful oxygen dynamic.

The presence of a β-phase is clearly correlated with a high bulk conductivity across the sample series as in [97]. Doping of the A-site with a trivalent cation reduces the overall oxygen vacancy content. It replaces negatively charged defects on the B site ($Y_{Zr}^{'}$) with positively charged defects on the A site ($Y_{Ba}^{\bullet}$), decreasing defect association of the proton.

The combined decrease in defect association and lattice expansion would be expected to increase protonic conductivity as is observed for the β-phase.

4.5 Discussion on the influence of the synthesis route on the grain boundary properties of $BaZr_{0.9}Y_{0.1}O_{3-\delta}$

Comparing Fig. 4-9. a and b indicates that the microstructure can at least partly explain the discrepancy in between the grain boundary conductivities of the different specimens. A specimen with big grains i.e. with low density of grain boundaries is expected to show a higher proton conductivity. In consequence, the microstructure needs to be optimised in order to match the performances for practical applications.

Besides the influence of the microstructure on the conductivity, it is not possible to exclude that this region host impurity elements, which would affect the grain boundary conductivity as suggested in the previous chapter. The impurities are likely to influence the space charge region and act as an electronic barrier for the proton transfer [98].

4.6 Conclusions

BZY10 was prepared by three different methods: the solid-state reaction method, the spray drying and the spray pyrolysis. Sintering dense at low temperature was not achieved for the powders synthesised by the spray pyrolysis and the spray drying. The powders obtained by the solid-state reaction method enable to obtain the denser specimen after sintering.

Specimens with different microstructures could be obtained from the three differently prepared powders by conventional sintering. However, no correlation between the microstructure and the bulk conductivity could be identified. In contrast, the dominating parameter affecting the bulk conductivity was found to be the lattice parameter. Specimens with large lattice parameters have a low activation energy. Site exchange is likely to explain the difference in lattice parameters and conductivities. Hence, controlling the lattice parameter of BZY10 during the preparation is crucial in order to tune the conductivity.

The grain boundary conductivity is much smaller than the bulk one and more difficult to understand. It shows a relation to the microstructure in terms of the grain size. The possible presence of impurities segregated in the grain boundaries cannot be excluded and will be investigated in the following chapter 5.

CHAPTER 5

Influence of Minor Element Addition on the Properties of $BaZr_{0.1}Y_{0.9}O_{3-\delta}$*

As shown in chapter 3, BZY10 is dominated by the grain boundary conductivity. Moreover, chapter 4 shows that the grain boundary conductivity is influenced by the microstructure. Thus optimising the microstructure, more precisely the grain boundary density, seems to be a key point. This issue can be addressed by improving the sintering of BZY10. In order to sinter at low temperatures, ceramists commonly add metal ions, also called sintering aids, in a few percentage quantity in their ceramic materials. Sintering is enhanced, when the additive:

- reacts with the material and forms a liquid phase,
- becomes liquid,
- becomes highly or low soluble in the materials.

The first two cases usually lead to classical liquid phase sintering, which is based on the fast diffusion of species in liquids. The third case is also called the solid solution approach, which is based on the diffusion of the additives in the grain or in the grain boundaries.

---

* *The results are accepted for publication in Solid State Ionics: doi:10.1016/j.ssi.2007.11.030, S.B.C. Duval, P. Holtappels, U. Stimming, T. Graule, "Effect of Minor Element Addition on the Electrical Properties of* $BaZr_{0.9}Y_{0.1}O_{3-\delta}$*"*

Using sintering aids to enhance the sintering has only be rarely followed for BZY10 yet [37, 81]. Among a large number of potential sintering aids, only the transition elements in the series Sc to Zn and Al_2O_3, MgO, and Y_2O_3 have been screened yet. The resulting improvement of the densification at low temperatures is still marginal. Another aspect is that theses elements are suspected to have an influence on the electrical behaviour of the material.

The idea of using additional metal ions for tuning the electrical properties was described by Avila-Paredes et al. for yttria stabilized zirconia [98]. Yttria stabilized zirconia shows a similar blocking effect in the grain boundaries as BZY10. However, the influence of minor element addition on the conductivity of BZY10 has never been investigated so far.

Therefore, this chapter aims to study the crystallographic, microstructural and conductivity of BZY10 prepared by adding metal ions in little amount as sintering aids.

5.1 Density of $BaZr_{0.9}Y_{0.1}O_{3-\delta}$ samples containing metal ions

Fig. 5-1 presents the density of BZY10 pellets prepared with the sintering aids in different concentrations as defined in Table 2-3. It is found that the density after sintering at 1500°C for 10 hours:

- is worsened using $BaMo_{0.33}Y_{0.67}O_3$ (1 mol.%), $BaMoO_4$ (1 mol.%), Mo (0.1 w.%), AlO_4P (0.1 w.%) and $Ba(NO_3)_2$ (1 mol.%),
- does not change significantly using MoO_3 (1 mol.% and 4 mol.%), Bi_2O_3 (1 w.%), $MgAl_2O_4$ (1 mol.% and 4 mol.%), $MgAl_2O_4$ calcined (4 mol.%), SiO_2 (1 mol.%), TiO_2 (1 mol.%), MgO (0.05 mol.%), $La(OH)_3$ (0.2 w.%), $Ba_2Zr_{0.8}Y_{0.2}O_3$, and $Ba(NO_3)_2$ (10 mol.%),
- improves of about 15% using $BaCe_{0.9}Y_{0.1}O_{3-a}$ (1 mol.%), $BaMo_{0.33}Y_{0.67}O_3$ (10 mol.%), MgO (1 mol.% and 2 mol.%), and Al_2O_3 (4 mol.%).

The density of BZY10 increases when the concentration of $BaMo_{0.33}Y_{0.67}O_{3-\delta}$, MgO, and $Ba(NO_3)_2$ increases. On the contrary, the densification of BZY10 decreases when the concentration of MoO_3 and $MgAl_2O_4$ increases.

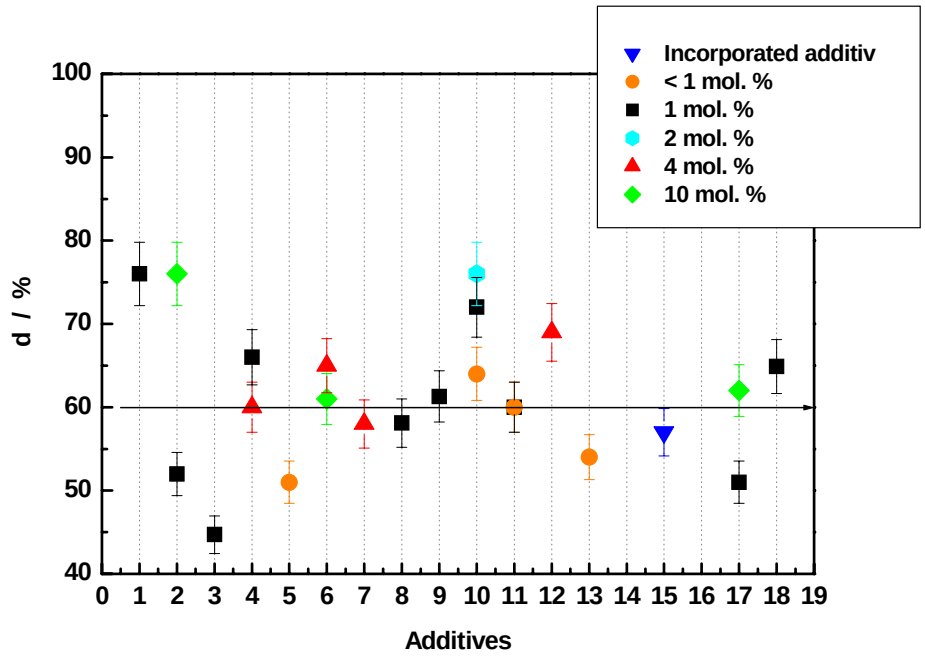

Fig. 5-1 Relative density of BZY10 containing 18 additives in different concentrations as defined in Table 2-3 after sintering at 1500°C for 10 hours.

Fig. 5-2 shows the densification of pure BZY10 and with addition of Bi_2O_3 (1 mol.%), TiO_2 (1 mol.%), Al_2O_3 (4 mol.%) and Mo (0.3 mol.%) for sintering either at 1500°C or at 1720°C. All additional elements tested in here are detrimental to the densification of BZY10. After sintering at 1720°C, the different additives led to a variety of different densities (from 67 to 94% of the theoretical density as reported in Table 5-1). For all specimens, higher densification was achieved at higher temperature (1720°C). Therefore, the following experiments will focus on MgO (1 mol.%), Bi_2O_3 (1 mol.%), TiO_2 (1 mol.%), Al_2O_3 (4 mol.%) and Mo (0.3 mol.%) sintered at 1720°C.

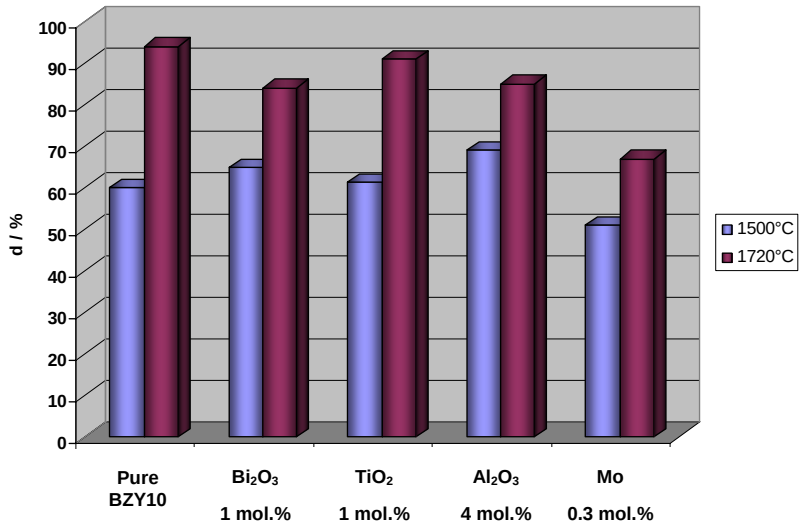

Fig. 5-2 Density after sintering at 1500°C and 1720°C of the pure BZY10, and with addition of Bi_2O_3 (1 mol.%), TiO_2 (1 mol.%), Al_2O_3 (4 mol.%) and Mo (0.3 mol.%).

Table 5-1 Proton concentration, density, lattice parameter of the sintered pellets containing different metal ions.

Sample	[OH.] (mol.%)	Density (%)	a=b=c (Å)	V_{cell} ($10^{-30}m^3$)	Presence of a 2nd phase
Without additive	3.87	94	4.206	74.34	No
+ [Al_2O_3]	0.88	85	4.198	73.99	Yes
+ [MgO]	1.07	79	4.200	74.10	No
+ [TiO_2]	1.69	91	4.182	73.13	Yes
+ [Mo]	0.28	67	4.199	74.03	Yes
+ [Bi_2O_3]	1.55	84	4.205	74.30	No

5.2 Proton concentration of $BaZr_{0.9}Y_{0.1}O_{3-\delta}$ samples containing metal ions

The concentration of protons calculated according to Eq. 2-7 and assuming that the mass change can be entirely attributed to the formation of protonic defect, is reported in Table 5-1. The concentration of protons in BZY10 varies from ~ 0.3 mol.%

for the addition of Mo to ~ 3.9 mol.% for the pure BZY10. In addition, Table 5-1 shows that the proton concentration increases with the density.

5.3 Crystallography of $BaZr_{0.9}Y_{0.1}O_{3-\delta}$ containing metal ions

The XRD patterns, shown in Fig. 5-3, confirm that all specimens are predominantly corresponding to BZY10. Weak intensity peaks are additionally present in the sample with additions of Al_2O_3, Mo, and TiO_2. These peaks cannot be indexed easily to the metal oxide as added to BZY10 or to any likely compound.

The crystallographic structure of BZY10 is found to be cubic for all specimens with significantly different lattice parameters as reported in Table 5-1. The bigger lattice parameter (4.206 Å) is found for a pure BZY10, whereas any addition decreases the lattice parameter up to 4.182 Å for the TiO_2 addition.

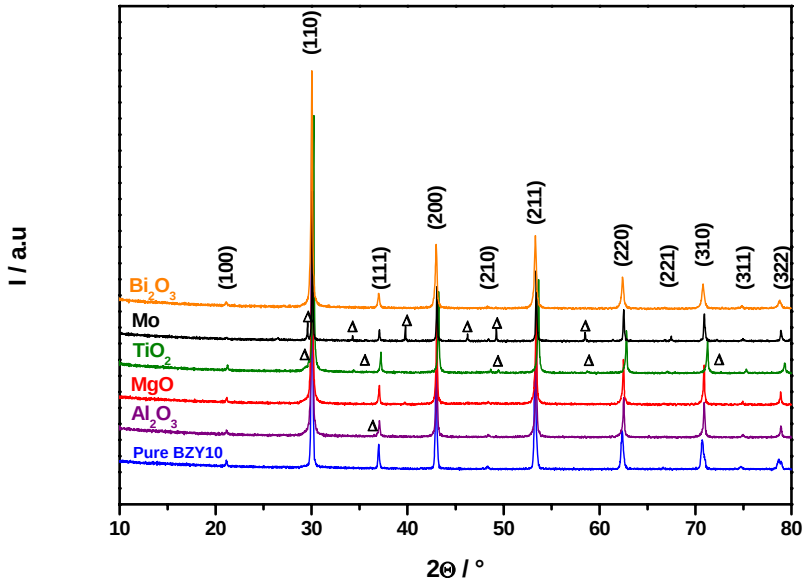

Fig. 5-3 The XRD patterns of BZY10 with minor element additions are compared to the diffraction pattern of pure BZY10. Additional peaks are indicated by the triangulate sign.

5.4 Conductivity of $BaZr_{0.9}Y_{0.1}O_{3-\delta}$ containing metal ions

5.4.1 Temperature dependence of the conductivity

The Nyquist plots of the different samples obtained at 300°C under wet O_2, pH_2O = 2200 Pa, are displayed in Fig. 5-4. Following the procedure described in chapter 3, the bulk and the grain boundary contributions could be separated and fitted with the model $(R_bC_b)(R_{GB}C_{GB})$.

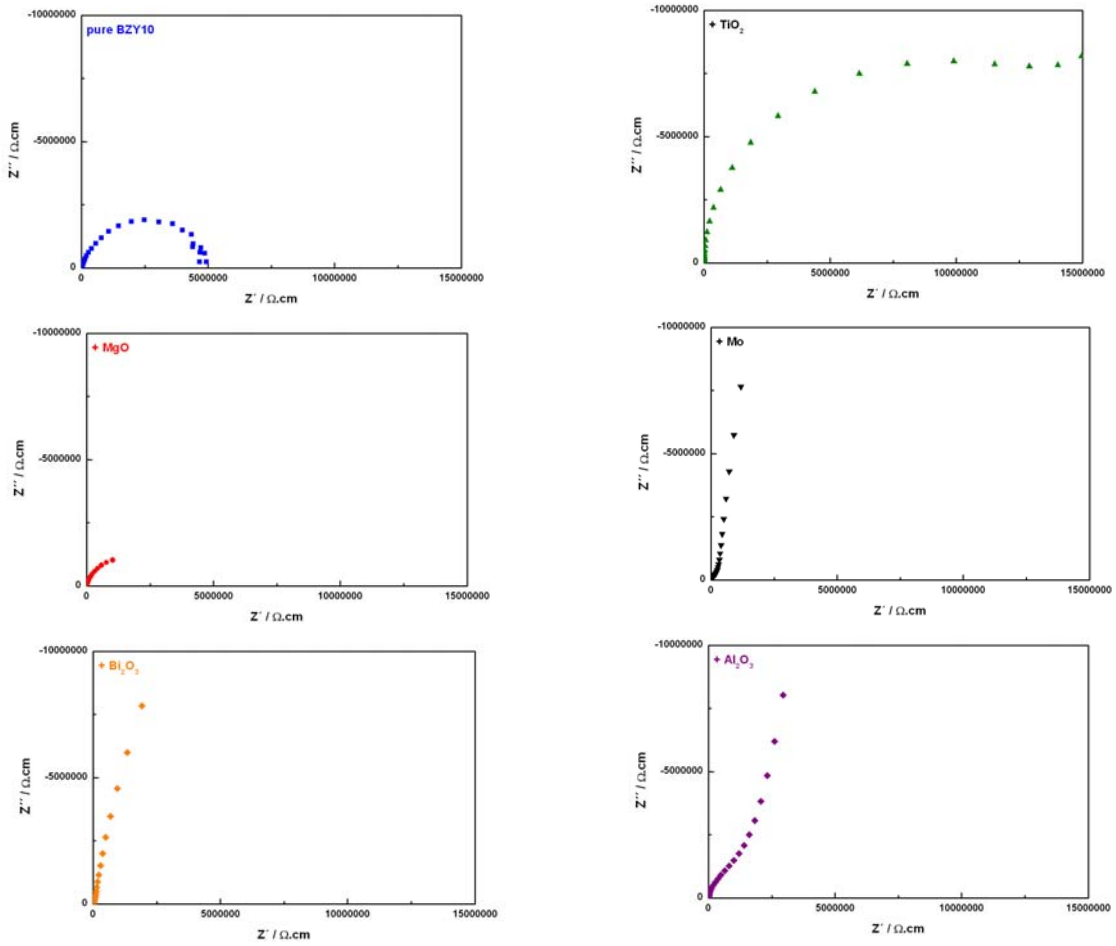

Fig. 5-4 Nyquist plots of the specimens with the different additives obtained at 300°C under wet O_2, pH_2O = 2200 Pa.

The temperature dependence of the apparent bulk and grain boundary conductivity is shown in Fig. 5-5. a and b, respectively. From these figures, it is obvious that the total conductivity is dominated by the highly resistive grain boundaries. Both apparent bulk and grain boundary conductivities are decreased by the addition of metal ions. The apparent bulk conductivity of BZY10 containing 1 mol.% of TiO_2 is the smallest: 3 orders of magnitude lower compared to pure BZY10 at 300°C. The specimens containing TiO_2, Al_2O_3, or Mo show similar apparent grain boundary conductivities. Their conductivities at 300°C are smaller by 1 order of magnitude compared to pure BZY10.

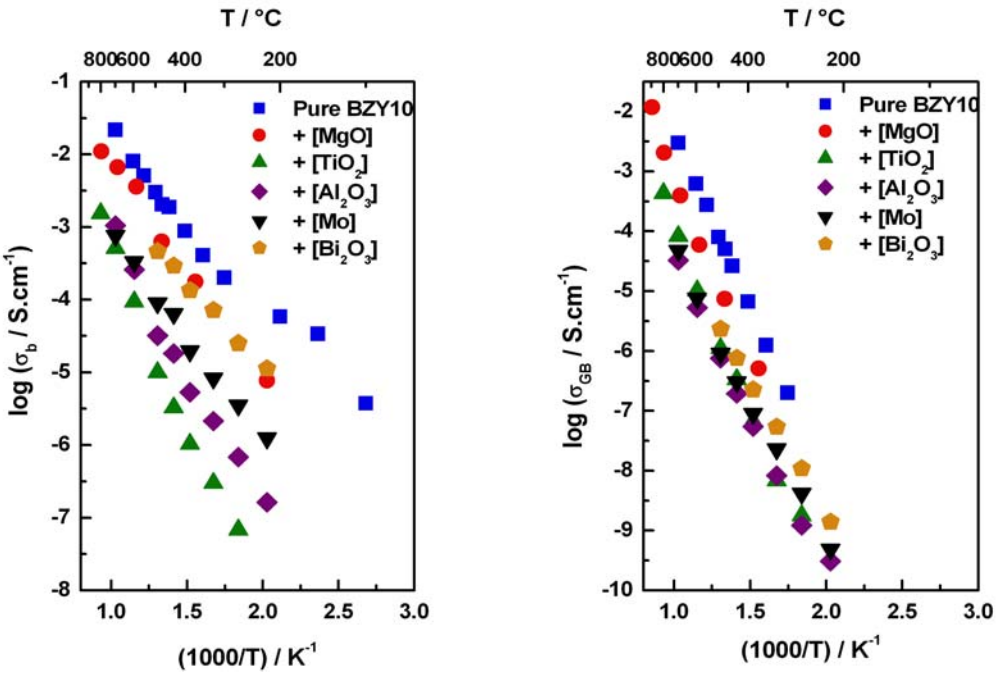

(a) (b)

Fig. 5-5 Temperature dependence of the apparent bulk (a) and grain boundary (b) conductivity.

The apparent grain boundary conductivity is corrected for the microstructure by Eq. 2-6 (the ratios of the capacitances are given in Table 5-2). The obtained specific grain boundary conductivity, $\sigma_{sp.\ GB}$, is plotted as a function of the reciprocal temperature in Fig. 5-6. The specific grain boundary conductivity is about 1 order of magnitude smaller than the apparent one.

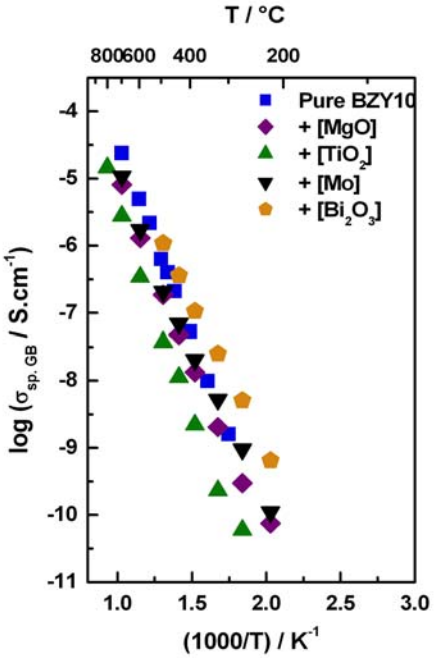

Fig. 5-6 Temperature dependence of the specific grain boundary conductivity.

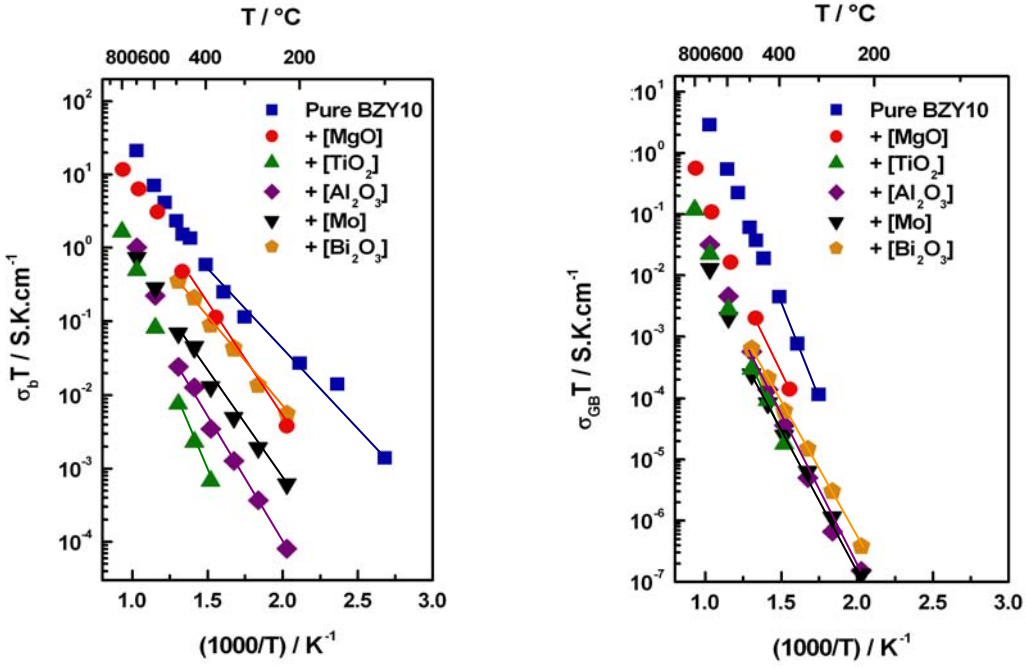

(a) (b)

Fig. 5-7 Arrhenius plots of the conductivity of the bulk (a) and the grain boundaries (b).

Table 5-2 Activation energies and pre-exponential factors of the bulk and the grain boundary conductivity of BZY10 without and with sintering aids.

Sample	Bulk		Grain boundary			C_b/C_{GB}
	E_a (eV)	σ_0 (K.S/cm)	E_a (eV)	σ_0 (K.S/cm)	$\sigma_{0\text{-sp. GB}}$ (K.S/cm)	
Without additive	0.46	$2x10^3$	1.21	$5x10^6$	$5x10^4$	$7.8x10^{-3}$
+ [Al_2O_3]	0.69	$8x10^2$	0.95	$3x10^2$	$5x10^2$	$2.46x10^{-1}$
+ [MgO]	0.60	$5x10^3$	1.04	$2x10^4$	-	-
+ [TiO_2]	0.86	$3x10^3$	1.08	$4x10^3$	$9x10^2$	$3.36x10^{-2}$
+ [Mo]	0.58	$4x10^2$	0.88	$1x10^2$	$2x10^2$	$2.28x10^{-1}$
+ [Bi_2O_3]	0.50	$7x10^2$	0.88	$4x10^2$	$1x10^3$	$4.68x10^{-1}$

The activation energies of the bulk conductivity are determined from Fig. 5-7 a. A linear behaviour is observed for T < 450°C. Arrhenius parameters are thus obtained for this temperature range and are reported in Table 5-2. They vary from 0.46 eV for the pure BZY10 up to 0.86 eV, when TiO_2 is added. The corresponding bulk pre-exponential factors remain similar for all samples ($1x10^3$ K.S.cm^{-1}).

The activation energies of the grain boundary conductivity, determined from Fig. 5-7. b for the same temperature range (200 – 450°C) are reported in Table 5-2, and vary from 0.88 eV to 1.21 eV. The grain boundary pre-exponential factors of pure BZY10 and BZY10 with MgO addition are about 1000 times bigger than the ones of the other specimens and the bulk ones for all samples.

5.4.2 Water partial pressure dependence of the conductivity

The conductivity was measured isobarically under wet O_2, pH_2O = 2200 Pa, and dry O_2, pH_2O < 10 Pa. The results for all specimens at 300°C are reported in Fig. 5-8. For all specimens containing additives as well as for pure BZY10, the conductivity is found to be higher under wet conditions than under dry ones. The pure BZY10 and BZY10 with addition of MgO and Bi_2O_3 show a significantly better (> 0.5 orders of magnitude) conductivity under wet O_2, pH_2O = 2200 Pa. BZY10 with addition of TiO_2 and Al_2O_3 shows a weaker influence of the partial pressure of water on the conductivity.

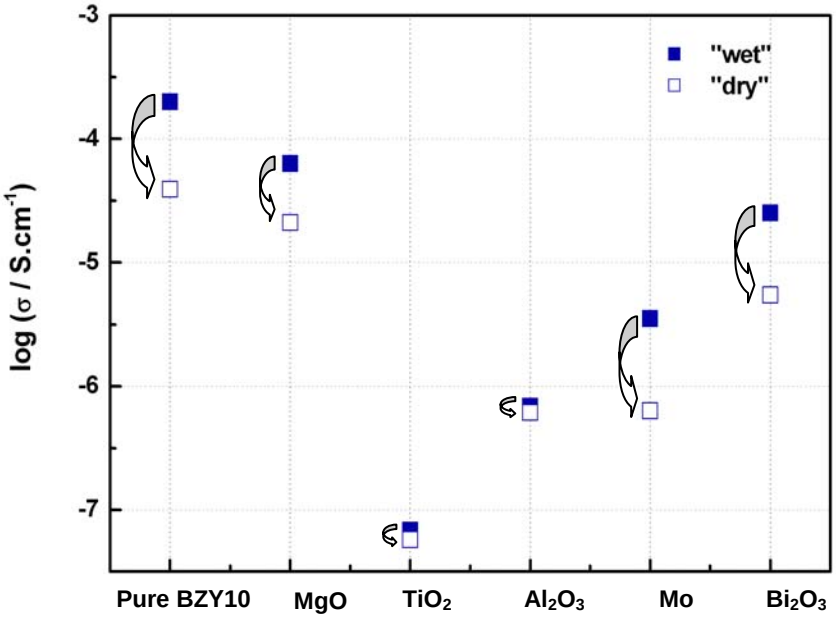

Fig. 5-8 Bulk conductivity at 300°C under wet oxygen, pH_2O = 2200 Pa, and dry oxygen, pH_2O < 10 Pa, for BZY10 and BZY10 with additives.

5.5 Discussion on the influence of metal ion additions on the density of $BaZr_{0.9}Y_{0.1}O_{3-\delta}$

In general, none of the sintering aids tested enhance the densification at low temperature. Only a long (about 24 hours) heat treatment at high temperature (1720°C) enables it as shown in chapter 3.

$BaCe_{0.9}Y_{0.1}O_{3-\delta}$, $BaMo_{0.33}Y_{0.67}O_3$, $BaMoO_4$, AlO_4P, BO_4P and Bi_2O_3 were selected for their low melting point (< 1400°C). Mo and TiO_2 were chosen because they may become liquid by a eutectic reaction with BZY10. The obtained low densification indicates that these compounds did not facilitate liquid phase sintering.

Another observation can be derived on the role of MgO, SiO_2 and Al_2O_3 additions in BZY10. It is found to be similar than what is described in [37]. Densification due to MgO addition has been explained as the cause of reduction in grain growth by

suppressing/eliminating continuous grain growth via slower boundary migration during the sintering process.

However, knowing if the additives either diffuse within BZY10 or react with BZY10 cannot be fully derived from the observations of this work. An inhomogeneous distribution of the additives is also to be considered and is very likely. This information is essential in order to consider the influence of additives on the electrical behaviour of BZY10 and should be further investigated.

5.6 Discussion on the influence of metal ion additions on the bulk properties of $BaZr_{0.9}Y_{0.1}O_{3-\delta}$

5.6.1 Nature of the charge carrier

Previous works show also a decreased bulk conductivity for BZY10 containing metal ions [81, 99]. These decreases are either attributed to a change in the nature or in the concentration of the charge carrier. All samples show a higher conductivity under humid atmosphere (Fig. 5-8). In addition, the bulk pre-exponential factors of BZY10 with metal ion additions are similar and similar to the one of pure BZY10 (Table 5-2). BZY10 is found to be purely protonic in chapter 3. Therefore, it seems unlikely that the bulk conductivity of specimen containing metal ions turns out to be dominated by an electronic contribution. The conductivity is considered to be dominated by the protons transport.

5.6.2 Influence of the microstructure and the crystallographic structure on the bulk conductivity

As the change of conductivity cannot be attributed to different charge carriers, it is interesting to consider the bulk conductivity as a function of the proton concentration. The concentration of protons was found to scale with the density (Table 5-2). However, no clear correlation can be found between the

density/concentration of protons and the conductivity at 300°C as illustrated in Fig. 5-10. In consequence, the microstructure i.e. porosity does not influence the conductivity.

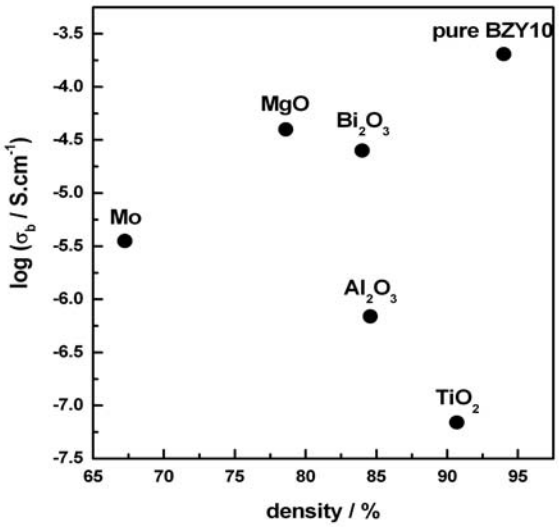

Fig. 5-9 The conductivity at 300°C under wet oxygen, pH_2O = 2200 Pa, is plotted as a function of the density.

Adding metal ions drastically affect both the lattice parameter of BZY10 (Table 5-3) and the conductivity (Fig. 5-6). The general feature of unpredictably scattering lattice parameter is observed like in chapter 4. In this chapter, Fig. 5-3 indicates that metal ions are likely to react with Ba, Zr or Y. Metal ions may substitute either A- or B- site of the BZY10 perovskite and a solid solution is obtained. The metal ions can also limit the possibility of having cross substituted β-phase as suggested already in chapter 4 and in Eq. 4-1 [97]. Considering Shannon´s radii [71], all trivalent cations with six coordinations are smaller than Y^{3+} and are added in a few percentage amount. In consequence, a reaction would in any case result in a decrease of the lattice parameter.

As observed for the pure BZY10 (chapter 4), the bulk conductivity of BZY10 with metal addition is sensitive to the interatomic distance (Fig. 5-10. a). An even better correlation is obtained for the bulk activation energy (Fig. 5-10. c) as the pre-

exponential factor appears to be similar for all specimens (Fig. 5-10. b and Table 5-2). BZY10 specimens with metal ion addition with the larger lattice parameters have the smaller bulk activation energies. These results are in line with results from chapter 4.

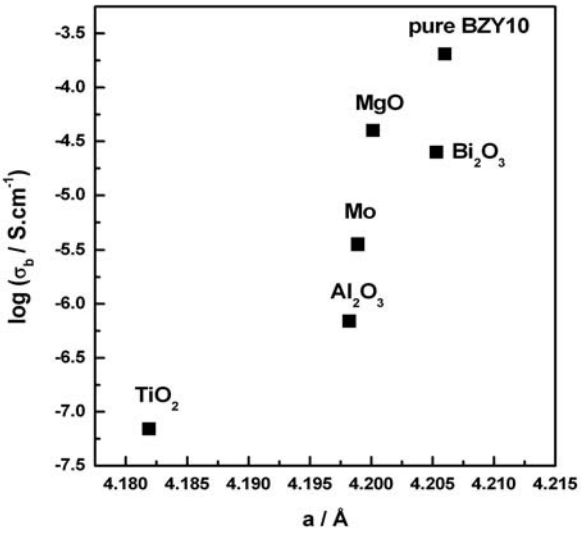

(a)

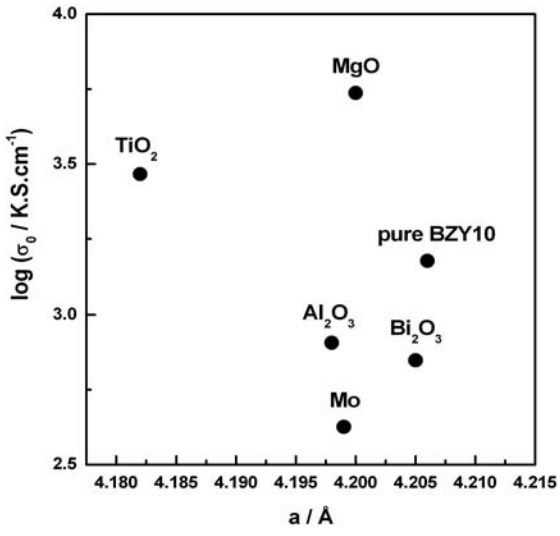

(b)

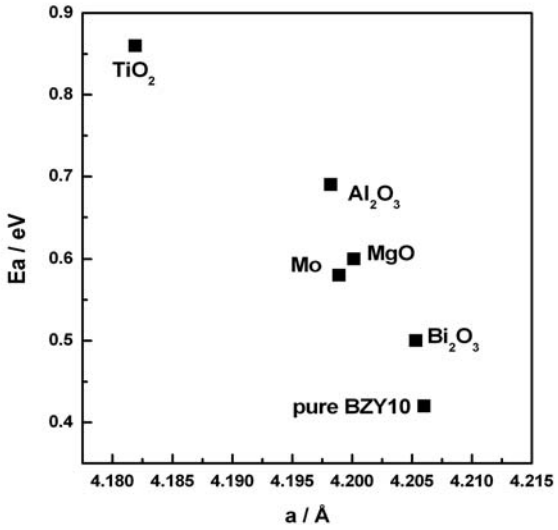

(c)

Fig. 5-10 Dependence of the bulk conductivity at 300°C under wet O_2, pH_2O = 2200 Pa (a), the bulk pre-exponential factor (b) and the bulk activation energy (c) on the lattice parameter of BZY10.

5.7 Discussion on the influence of metal ion additions on the grain boundary properties of $BaZr_{0.9}Y_{0.1}O_{3-\delta}$

The conductivity varies over ~ 2.5 orders of magnitude for the bulk and over ~ 1 order of magnitude for the specific grain boundary conductivity. This result suggests that metal ion additions affect differently the bulk and the grain boundaries.

In comparison to the apparent grain boundary conductivity, the specific grain boundary conductivity is 1 order of magnitude smaller (Fig. 5-6). More interesting is that the apparent grain boundary conductivity varies over more than 1.5 orders of magnitude as the specific grain boundary conductivity varies only over 1 order of magnitude. The normalisation for grain boundaries only partly explains the differences in the grain boundary conductivity of the samples. Another factor need to be taken into account. Furthermore, the scatter of the specific grain boundary conductivity is larger for BZY10 with metal ions (Fig. 5-6) compare to pure BZY10 prepared by different methods (Fig. 4-9), the microstructures being similar. It cannot be excluded that the metal ions partially or entirely segregate in the grain boundaries. As the grain boundary

conductivity of pure BZY10 is dominated by hole transport (chapter 3), it is very likely that the additives affect the electronic conductivity.

5.8 Conclusions

Potential sintering aids were tested. Addition of TiO_2, MgO, Mo, Al_2O_3 and Bi_2O_3 in a mole percent range is detrimental to the densification of $BaZr_{0.9}Y_{0.1}O_{3-\delta}$. The denser samples are obtained by using $BaCe_{0.9}Y_{0.1}O_{3-\delta}$ (1 mol.%), $Ba(NO_3)_2$ (10 mol.%) and MgO (2 mol.%) and have around 80% of the theoretical density after sintering at 1500°C for 10 hours. The results are still far from the target.

As observed in previous chapter, wide lattices favour low activation energies of the proton conductivity. No additional effect of additives on the activation energy of the bulk conductivity is observed. For the grain boundaries, we cannot exclude that the differences in the grain boundary conductivities arise from the particular element additions.

CHAPTER 6

Influence of a High Annealing Temperature on the Properties of $BaZr_{0.1}Y_{0.9}O_{3-\delta}$*

Porous and dense polycrystalline specimens have been synthesised by different methods in the previous chapter 3, 4, and 5. One common issue is found for all specimens: the grain boundaries are found to be highly resistive and to limit the overall conductivity of BZY10. Thus, it prevents from considering BZY10 as an electrolyte for fuel cell for example. In consequence, one would ideally use a single crystal for practical applications in electrochemical devices.

A single crystal is a crystal with only one crystalline orientation i.e. with no grain boundaries. Among the proton conducting perovskites, $BaCeO_3$, $SrCeO_3$ and $SrZrO_3$ were already prepared as single crystals and characterised [57, 100, 101]. Due to the extremely high melting point of $BaZrO_3$, any single crystal of this composition has never been grown so far.

The floating zone method is an advantageous method to grow perovskite single crystals. It enables to grow cylinder of ~ 5 mm diameter, which can be characterised

* *The results are published: S.B.C. Duval, P. Holtappels, U.F. Vogt, E. Pomjakushina, K. Conder, U. Stimming, T. Graule, "Electrical Conductivity of the Proton Conductor of $BaZr_{0.9}Y_{0.1}O_{3-\delta}$ Obtained by High Temperature Annealing", Solid State Ionics, 178 (2007) 1437-1441.*

further with respect to their conductivity. Another advantage is that no crucible is required and thus no contamination is expected [102].

Therefore, BZY10 was annealed by the optical floating zone method at the highest possible temperature. The crystallographic, microstructural and electrical properties of the resulting specimens were studied and compared to BZY10 synthesised by the standard solid-state reaction route and sintered at 1720°C.

6.1 Crystallography, microstructure and proton content of $BaZr_{0.9}Y_{0.1}O_{3-\delta}$ annealed at high temperature

The X-ray diffraction patterns of the standard BZY10 sample sintered at 1720°C, SS1720 and the BZY10 specimen annealed at high temperature, ZA2200 are presented in Fig. 6-1. The comparison shows that the zone annealed sample, ZA2200, gives a single cubic phase corresponding to BZY10 as stated in chapter 3. The cubic lattice parameters of the solid-state specimen, SS1720, and the rod annealed at high temperature, ZA2200, are 0.4206 and 0.4212 nm, respectively.

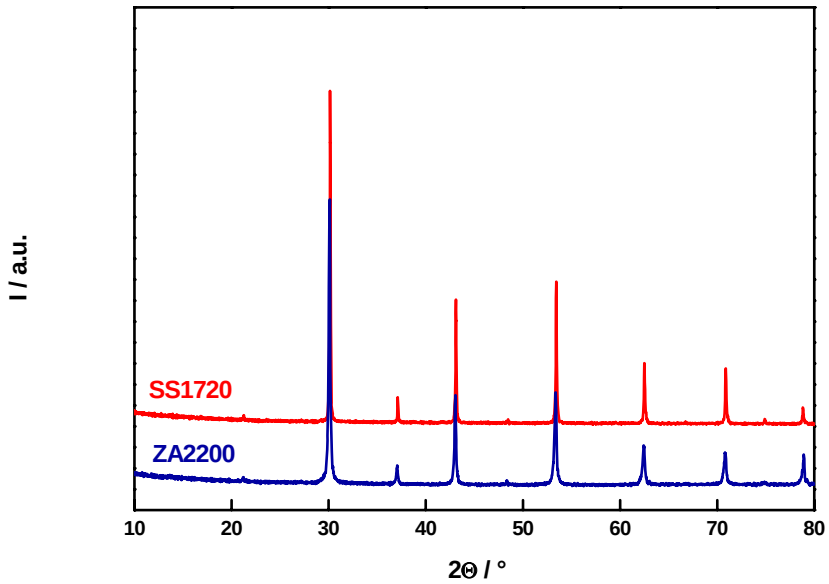

Fig. 6-1 XRD patterns of the specimen synthesised in a standard way, SS1720, and the one annealed at high temperature, ZA2200.

The microstructures of the standard specimen, SS1720, and the annealed specimen, ZA2200, presented in Fig. 6-2 are relatively homogeneous with grain sizes of about 2 and 5 μm, respectively. The density increases from 91% of the theoretical density for SS1720 to 98% for ZA2200.

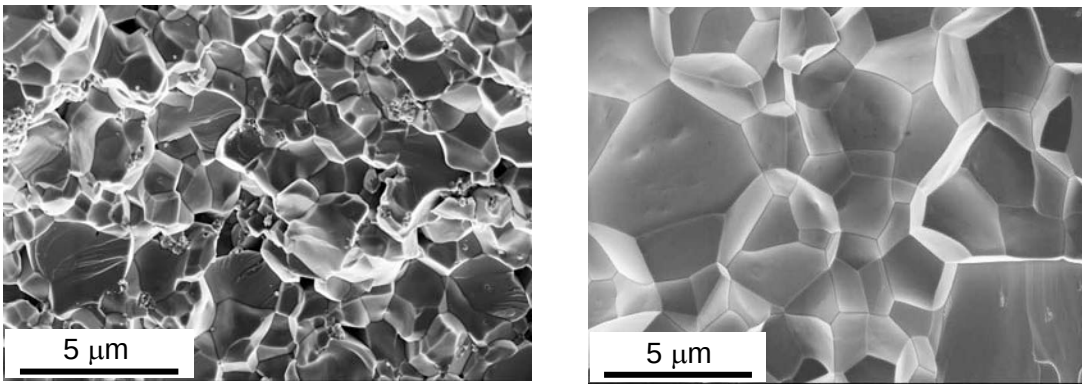

(a) (b)

Fig. 6-2 SEM pictures of the specimen synthesised in a standard way, SS1720 (a), and the one annealed at high temperature, ZA2200 (b).

The proton concentration is found to be ~ 7 mol.% and the deuteron concentration is ~ 8 mol.% for the rod annealed at high temperature, ZA2200, which is twice as much as what was found for the solid-state sample, SS1720, as stated in chapter 3.

6.2 Conductivity of $BaZr_{0.9}Y_{0.1}O_{3-\delta}$ annealed at high temperature

6.2.1 Temperature dependence of the conductivity

The Nyquist plots of the standard specimen, SS1720, and of the annealed rod, ZA2200 at 100°C and 300°C under wet O_2, pH_2O = 2200 Pa, are reported in Fig. 6-3. Two semicircles are clearly seen for both samples at 100°C. A third semicircle appears above 300°C at the low frequencies end for the ZA2200 sample. The interpretation of

the impedance data is performed as described in chapter 2 and 3 using the equivalent circuit $(R_bC_b)(R_{GB}C_{GB})$.

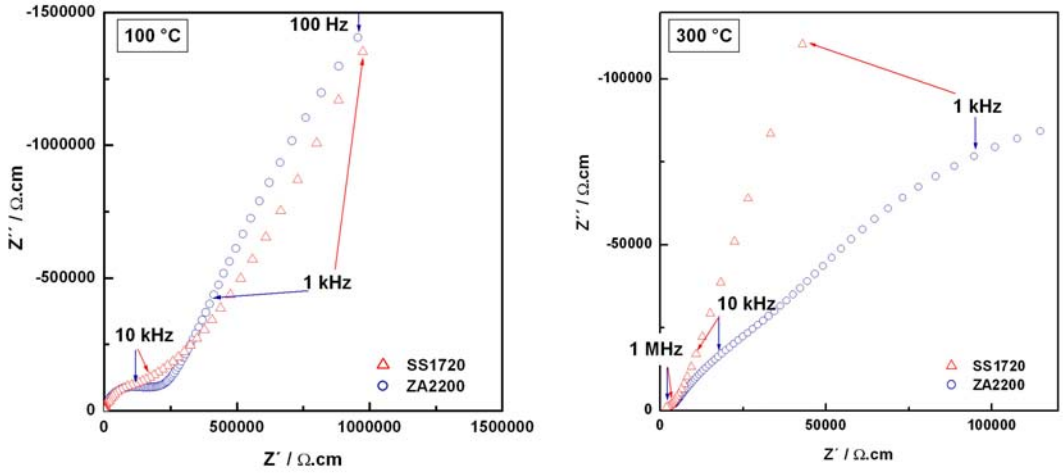

(a) (b)

Fig. 6-3 The Nyquist plots of the specimen synthesised by a standard way, SS1720 and the rod annealed at high temperature, ZA2200 monitored at 100°C (a) and at 300°C (b) under wet O_2, pH_2O = 2200 Pa.

The temperature dependence of the apparent bulk and grain boundary conductivity for the standard specimen, SS1720, and the annealed rod, ZA2200, are presented in Fig. 6-4. The bulk conductivity of both samples under wet conditions is comparable within the experimental uncertainty, whereas the apparent grain boundary conductivity for SS1720 is approximately 2 orders of magnitude lower than for ZA2200.

Fig. 6-4 also shows the temperature dependence of the specific grain boundary conductivity, obtained by using $C_{Bulk}/C_{GB}= 7.96x10^{-3}$ for SS1720 and $2.84x10^{-3}$ for ZA2200. The specific grain boundary conductivity of both samples is approximately 2 orders of magnitude lower than their respective apparent grain boundary conductivity over the temperature range 100°C – 500°C. However, the discrepancies between the two samples remain.

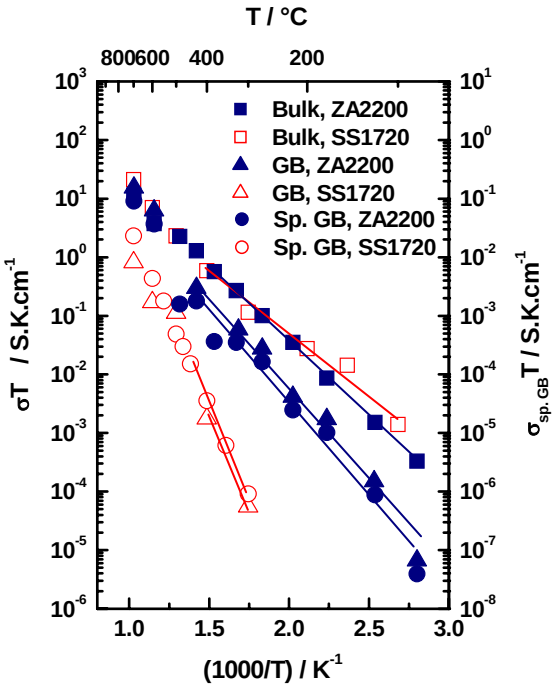

Fig. 6-4 Arrhenius plot of the apparent bulk and the apparent grain boundary conductivity and the specific grain boundary conductivity of the standard specimen, SS1720, and the annealed rod, ZA2200.

Table 6-1 shows the activation energies, E_a, of the bulk and the grain boundary conductivity for the standard solid-state specimen, SS1720, and the annealed one, ZA2200, under wet oxygen, pH_2O=2200 Pa, and dry oxygen, pH_2O < 10 Pa. The pre-exponential factors, σ_0, and the specific grain boundary pre-exponential factors, $\sigma_{0\text{-sp. GB}}$, are also reported.

The bulk activation energy under wet conditions is ~ 0.45 eV and is similar for the standard and the annealed specimens. For both specimens, the activation energy increases under dry conditions up to 0.53 eV for the standard solid-state sample, SS1720, and up to 0.80 eV for the annealed sample, ZA2200. The same observations can be made for the bulk pre-exponential factors. Under wet conditions, the bulk pre-exponential factors are ~ 10^3 S.K.cm^{-1}. Under dry conditions, the grain boundary pre-exponential factors are ~ 10^4 S.K.cm^{-1} for the standard solid-state specimen and ~ 10^6 S.K.cm^{-1} for the annealed one.

For the grain boundaries, the activation energy is in general found to be higher than for the bulk. The activation energy of the grain boundary conductivity of the standard sample, SS1720, under wet and dry conditions and the one of the annealed specimen under dry conditions are similar with values around 1 eV. The activation energy of the grain boundaries of the annealed specimen, ZA2200, is 0.55 eV. A similar value was obtained for the bulk under the same conditions. As well, the grain boundary pre-exponential factor of the annealed specimen is ~ 10^3 S.K.cm^{-1}, which is of the same order of magnitude than the bulk pre-exponential factor under wet conditions. The values for the grain boundary pre-exponential factors of the standard specimen under wet conditions are found to be much higher of ~ 10^6 S.K.cm^{-1} and rather comparable to values obtained for the bulk under dry conditions.

Table 6-1 Comparison of the activation energies and the pre-exponential factors of the bulk and the grain boundary conductivity of the standard specimen, SS1720 and the annealed specimen, ZA2200, in wet and dry oxygen below 400°C.

	Sample	Bulk		Grain boundary		
		E_a (eV)	σ_0 (K.S/cm)	E_a (eV)	σ_0 (K.S/cm)	$\sigma_{0\text{-sp. GB}}$ (K.S/cm)
Wet	SS1720	0.46	$2x10^3$	1.21	$5x10^6$	$5x10^4$
pH_2O=2200 Pa	ZA2200	0.44	$5x10^3$	0.55	$8x10^3$	$6x10^1$
Dry	SS1720	0.53	$5x10^4$	1.30	$3x10^6$	
pH_2O < 10 Pa	ZA2200	0.80	$1x10^6$	0.90	$2x10^6$	

6.2.2 Water partial pressure dependence of the conductivity

The conductivity of the annealed specimen, ZA2200, measured at 300°C under wet oxygen, pH_2O = 2200 Pa, and dry oxygen, pH_2O < 10 Pa, is shown in Fig. 6-5. For comparison the data for the standard solid-state sample, SS1720, are also reported.
Regarding both the bulk and the grain boundaries, the conductivities under dry conditions are found to be lower by 0.5 orders of magnitude or more compared to the conductivity under wet atmosphere for both specimens. The difference in the conductivities under wet and dry conditions is found to be the largest for the bulk conductivities of the annealed sample, ZA2200. In contrast, the bulk and the grain

boundary conductivities of the standard sample and the grain boundary conductivity of the annealed sample show the same trend under wet and dry atmosphere.

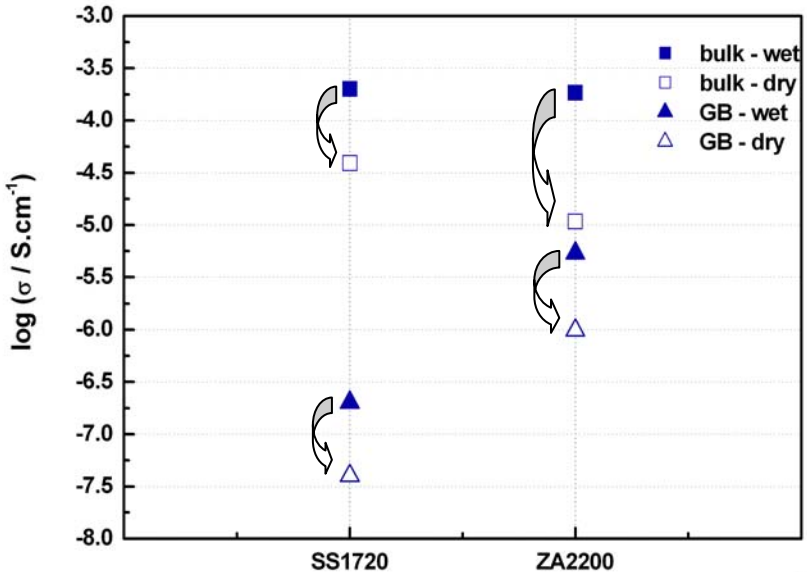

Fig. 6-5 Conductivity of the apparent bulk and grain boundary under wet O_2, pH_2O = 2200 Pa, and dry O_2, pH_20 < 10 Pa, for the specimen annealed at high temperature, ZA2200. For comparison, the data of the standard sample, SS1720, are also reported.

6.2.3 Oxygen partial pressure dependence for the specimen annealed at high temperature

The equilibrium conductivity at 400°C, 500°C, and 600°C for a wide range of oxygen partial pressures is presented for the specimen annealed at high temperature, ZA2200, in Fig. 6-6. Under wet conditions, pH_2O = 2200 Pa, the bulk conductivity (Fig. 6-6. a) is independent of the partial pressure of oxygen for all temperatures. In contrast, under dry conditions, pH_2O < 10 Pa, the conductivity decreases of about 1 order of magnitude changing the atmosphere from oxygen ($pO_2 = 10^5$ Pa) and to argon ($pO_2 = 2.10^{-6}$ Pa).

For the grain boundaries (Fig. 6-6. b), the conductivity values reach a minimum at around pO_2 = 0.2 Pa under both wet and dry atmospheres.

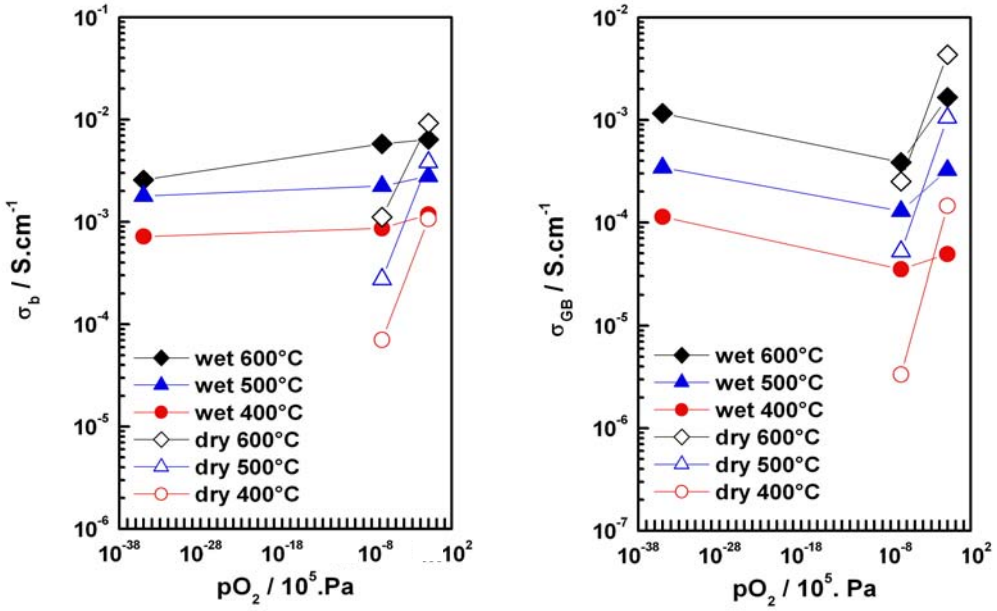

(a) (b)

Fig. 6-6 Oxygen partial pressure dependence of the apparent bulk (a) and grain boundary (b) conductivity under wet conditions, pH_2O = 2200 Pa, and dry conditions, pH_2O < 10 Pa, for the sample annealed at high temperature, ZA2200.

6.2.4 Hydrogen and deuterium partial pressure dependence on the conductivity for the specimen annealed at high temperature

Fig. 6-7 shows the total conductivity of the annealed specimen under protonated, deuterated and proton/deuteron free atmosphere as a function of the reciprocal temperature. The conductivity under protonated conditions is found to exceed all others in the temperature range 150°C – 500°C. The conductivity under deuterated atmosphere is found to be at least 0.5 orders of magnitude smaller than under protonated conditions, but still higher by about 1 order of magnitude than under dry atmosphere.

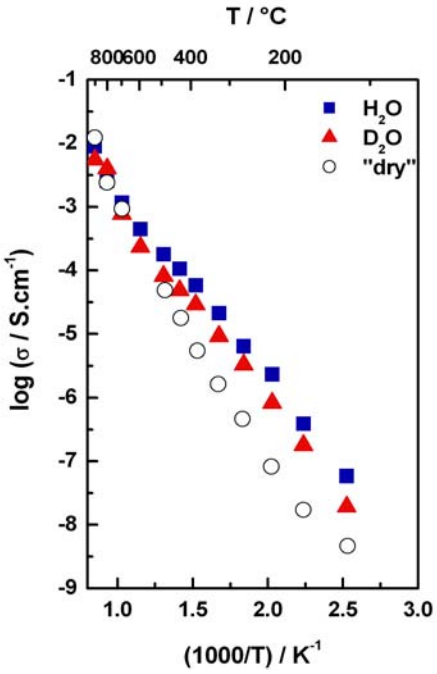

Fig. 6-7 Temperature dependence of the total conductivity for BZY10 under Ar passed through H_2O or D_2O and under dry O_2 for the specimen annealed at high temperature, ZA2200.

In Fig. 6-8. a, the contributions of the bulk and the grain boundary conductivities for the rod annealed at high temperature, ZA2200, are reported. Under H_2O atmosphere, the grain boundary conductivity is around 0.5 orders of magnitude lower than under D_2O atmosphere. The variations in the bulk conductivity between H_2O and D_2O atmosphere are about 1 order of magnitude.

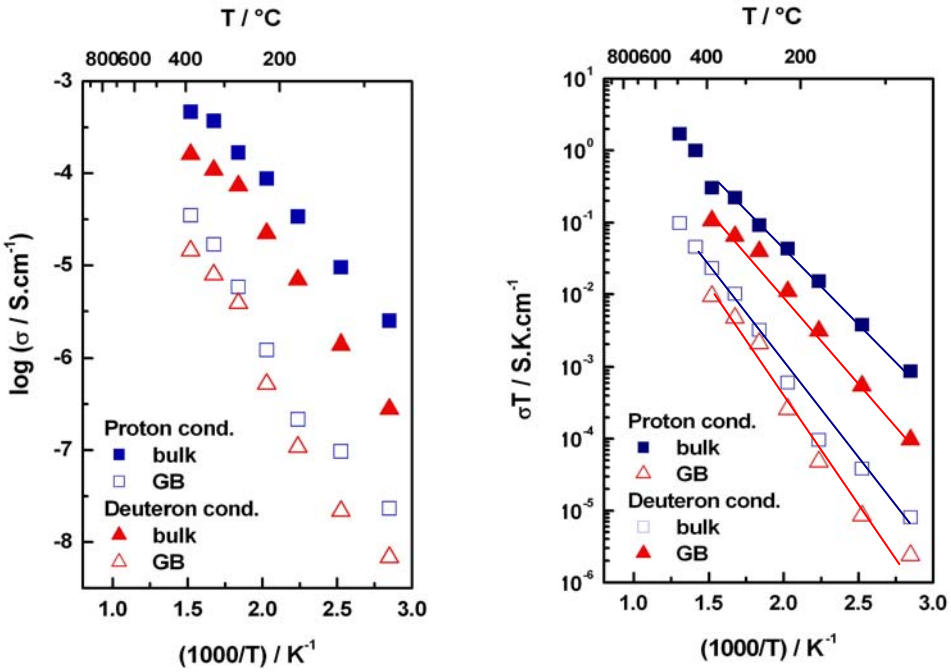

(a) (b)

Fig. 6-8 Temperature dependence of the bulk and the grain boundary conductivity under Ar passed through H_2O or D_2O for the specimen annealed at high temperature, ZA2200 (a). Arrhenius plot of the bulk and the grain boundary conductivity (b).

Table 6-2 presents the activation energies and the pre-exponential factors of the conductivities for the deuterated and protonated BZY10, which are determined from Fig. 6-8. b. The bulk activation energy under protonated conditions is 0.40 eV. Under deuterated conditions, it increases slightly up to 0.47 eV. The activation energy of the grain boundary conductivity under deuterated conditions is about 0.61 eV, which is also higher than 0.55 eV under protonated conditions. All pre-exponential factors for the bulk and the grain boundary conductivity are similar and are ~ $5x10^2$ $K.S.cm^{-1}$.

Table 6-2 Activation energies, and pre-exponential factors for the bulk and grain boundary conductivity of the sample annealed at 2200°C, ZA2200, under Ar passed through H_2O or D_2O.

	Proton conduction		Deuteron conduction	
	E_H (eV)	$\sigma_{0\text{-}H}$ (K.S/cm)	E_D (eV)	$\sigma_{0\text{-}D}$ (K.S/cm)
Bulk	0.40 ± 0.01	$5.60x10^2 \pm 1$	0.47 ± 0.02	$6.26x10^2 \pm 2$
Grain boundaries	0.55 ± 0.03	$3.20x10^2 \pm 2$	0.61 ± 0.04	$5.28x10^2 \pm 2$

Table 6-3 shows the ratio of the conductivities, the difference of activation energies and the ratio of the pre-exponential factors under protonated and deuterated conductivity for the bulk and the grain boundaries. The ratio of the pre-exponential factors is found to be of 0.4 for the bulk and of 0.6 for the grain boundary. The difference of activation energy is about 0.06 eV. The ratio of the conductivity at 300°C if of 2.3 for the bulk and 1.5 for the grain boundaries.

Table 6-3 Comparison of the conductivities at 300°C under Ar passed through H_2O or D_2O, of the activation energies and the pre-exponential factors of the bulk and grain boundary conductivity for the specimen annealed at 2200°C, ZA2200.

	Ratio		
	σ_H/σ_D (at 300°C)	$E_D - E_H$ (eV)	$\sigma_{0\text{-}H}/\sigma_{0\text{-}D}$
Bulk	2.3	0.07	0.42
Grain boundaries	1.5	0.06	0.60

6.3 Discussion on the preparation of $BaZr_{0.9}Y_{0.1}O_{3-\delta}$

The maximal temperature (~ 2200°C) allowed by the optical floating zone furnace is far below the melting temperature of BZY10 (~ 2600°C). In consequence, the optical floating zone is not used for its standard purpose (i.e. growing single crystal), but in the present work it serves for annealing the BZY10 sample.

The obtained ZA2200 sample is polycrystalline, certainly, but it has a more homogeneous microstructure, an increased density and grains about twice as large, without any visible changes in the XRD pattern. In addition, the obtained specimen after annealing is dense. In consequence, the influence of the porosity can be neglected (which was not the case in the previous chapters 4 and 5).

6.4 Discussion on the influence of a high annealing temperature on the bulk properties of $BaZr_{0.9}Y_{0.1}O_{3-\delta}$

6.4.1 Nature of charge carrier

The nature of the conductivity of the specimen annealed at high temperature will be discussed in the following. The bulk conductivity is independent of the partial pressure of oxygen, as shown in Fig. 6-6. Moreover, the conductivity depends clearly on the hydrogen isotope (Fig. 6-8). In addition, the dependence on the partial pressure of water indicates that the conductivity is higher in presence of protons. Similarly, the significant increase of the activation energy of the bulk conductivity of ZA2200 under dry conditions compared to wet conditions indicates clearly that the nature of the charge carrier changes with the atmosphere. Furthermore, the activation energy of the bulk conductivity for the specimen annealed at high temperature is similar to the one for the specimen sintered at 1720°C (chapter 3) and the one from Bohn et al. [25]. Therefore, the bulk conductivity of the annealed rod is dominated by the proton transport as described by Eq. 1-2.

6.4.2 Mechanism of the proton transport

H/D exchange experiments (Fig. 6-8) give indication about the proton transport mechanism in the bulk of BZY10. Since the mass ratio OH^-/OD^- is smaller than H/D, a vehicle mechanism, which would consist of the motion of OH^- is not favoured. Such a mechanism would give rise to a much smaller difference in conductivities than

observed (Table 6-3). These results are rather consistent with a Grotthus mechanism, which consists of a simple proton hopping.

The ratio of the pre-exponential factors (Table 6-3) is found to be of 0.4 for the bulk, which is much smaller than the expected ratio $\sqrt{2}$. This ratio corresponds to the inversed ratio of the reduced mass of the O-H oscillator, which is considered in classical statistical mechanics [103]. Under the experimental conditions and assuming that the isotope exchange is completed, the proton concentration is found to be ~ 7 mol.% and the deuteron concentration is ~ 8 mol.% which leads to a higher pre-exponential factor in the case of D [104].

However, the bulk activation energy for proton jumps is lower by about 0.06 eV (Table 6-3) than for the deuteron jumps i.e. the activation energy appears to be strongly dependent on the migrating species H^+ or D^+. Indeed, it was found that the activation energy depends on the zero-point energy in a semi-classical approach [5, 6]. Due to the low mass and high stretching frequency associated with the hopping of H or D atom, quantum effects manifest themselves in the zero-point energy. In fact, it was found that this ground state is not at the bottom of the potential but at a level equal to $(1/2)h\nu_{H\text{-}D}$ [105]. The calculation of the stretching vibration frequencies of the OH and OD bands from infrared data shows that theoretical values falls in the same range than observed in the present work. In addition, the ratio of conductivities is considerably greater than the classical ratio $\sqrt{2}$. One might anticipate that the frequency for an active jump would be slightly lower (by a factor of ~ $\sqrt{2}$) for D than for H, a consequence of the higher mass of D. In consequence, a purely classical theory is not obeyed and a semi-classical theory is rather consistent. These results are very similar to previous isotope effect results for substituted $BaCeO_3$ [103, 106, 107].

6.4.3 Influence of the crystallography on the conductivity

The evaporation of Ba at high temperatures is often pointed out in the literature [31, 40] as a reason for discrepancies in the bulk conductivity values. In the present work, neither visible changes in the XRD patterns nor significant differences in the bulk conductivity are observed. Therefore, no further Ba evaporation took place while

annealing at 2200°C and the composition, crystal structure and bulk conductivity is not affected by the high temperature treatment.

6.5 Discussion on the influence of a high annealing temperature on the grain boundary properties of $BaZr_{0.9}Y_{0.1}O_{3-\delta}$

6.5.1 Nature of the charge carrier

As shown in Fig. 6-6, the grain boundary conductivity of the annealed rod increases with the partial pressure of oxygen under wet and dry conditions. Even if the scarcity of data does not allow for a test of the exponent, it is indication for hole conduction as predicted by Eq. 1-4. Nevertheless, the conductivity is higher under higher water partial pressure (Fig. 6-5). Also, the activation energy of the grain boundary conductivity of the annealed specimen is coming closer to the activation energy of the bulk conductivity. As well the pre-exponential factor is found to be similar. In addition, the conductivity under deuterated atmosphere is, at least, 0.5 orders of magnitude lower than the conductivity under protonated atmosphere (Fig. 6-7 and Fig. 6-8). A clear isotope effect is observed for the total conductivity as well as for the bulk and the grain boundaries. Therefore, it is concluded that the annealing at high temperature the grain boundary conductivity turns out to be dominated by protons under wet conditions.

6.5.2 Influence of the microstructure/crystallography on the conductivity

The grain boundary conductivity is tremendously increased after annealing at high temperature. Additionally, grain growth is observed during the high temperature annealing. In the following, we analyse if the increase of the grain boundary conductivity after annealing can be attributed to a lower grain boundary density. As the specific grain boundary conductivity of annealed specimen is still approximately

2 orders of magnitude higher than the one of the standard specimen, the lower resistance attributed to the grain boundaries for the annealed specimen is hardly be explained by an improved microstructure alone (i.e. the grain growth during annealing at high temperature). In addition, the change in the nature of the charge carrier indicates that the observations are not related to the microstructure. Therefore, the observed increase after annealing at high temperature for ZA2200 is likely to be caused by another effect than the optimisation of the microstructure. The increase of the grain boundary conductivity and the change from hole to proton conduction after annealing at high temperatures is tentatively attributed to changes in the crystallographic structure and/or in the composition in the ppm range in the vicinity of the grain boundaries as discussed below.

On the one hand, such local changes in the grain boundary region may be indicated by changes in the fracture behaviour (Fig. 6-2) from inter- to intra-granular cracking for ZA2200 and SS1720 respectively. We presume that intrinsic crystallographic failures are present in the sintered sample, but are overcome by extreme heat treatment as observed from the sample annealed at 2200°C. On the other hand, changes in composition in the ppm range were already discussed by Babilo et al. for the case of Zn addition [81].

In the present work, the influence of the annealing temperature can be discussed towards two main arguments. First, the specific optical system in the floating zone furnace is considered. A narrow hot zone of about a few millimetres is moved back-and-forth along the sample. Diffusion of impurities could occur in the grain boundaries following the hot zone. The zone melting technique is often used for materials´ purification, but segregation of impurities occurs generally in a melted state. In the present work, the sample was kept at ~ 2200°C, which is far away from the melting temperature (~ 2600°C). However, in order to prove systematically this hypothesis, the temperature dependence of the bulk and the grain boundary conductivity of ZA2200 was measured for two samples cut from the middle part of the annealed rod, for one from the upper part and one from the bottom part, where a pronounced segregation of impurities would be expected. The conductivity values for the bulk and for the grain boundaries differ less then 20% and are independent on the sample's position in the original rod. This small variation can hardly explain the 2 orders of magnitude

difference between the grain boundary conductivity of SS1720 and ZA2200. The variation is rather attributed to the uncertainty in determining the bulk contribution from the impedance spectra. In conclusion, the optical zone annealing technique is not likely to cause the increase in the apparent grain boundary conductivity after high temperature annealing.

Secondly, Snijkers et al. suggested the presence of a "Y-Zr-O" phase in the grain boundary [31]. In our work neither SEM nor TEM investigations on SS1720 and ZA2200 indicate a second phase, like a "Y-Zr-O" phase in the grain boundary region (chapter 3). Nevertheless, we cannot exclude that some impurities are present in the grain boundaries and could be irreversibly dissolved into the bulk during the annealing process changing thus the space charge region [108]. Presuming that the transport of protons across the grain boundaries is sensitive to space charge effects, such -even small- compositional changes occurring during annealing may accelerate significantly the grain boundary transport. In contrast, the bulk conductivity is not likely to be affected.

6.6 Conclusions

High temperature annealing (at ~ 2200°C) results in a polycrystalline material (ZA2200 sample), which presents a more homogeneous microstructure with larger grains and higher density than with the standard sample sintered at 1720°C (SS1720).

The grain boundary conductivity increases of approximately 2 orders of magnitude, whereas the bulk conductivity does not undergo any changes. The grain boundaries turn out also to be dominated by proton transport instead of holes, which were found to dominate in the grain boundaries of samples prepared by conventional sintering. The different microstructures, in particular the grain size, cannot explain these differences in the grain boundary conductivities. More likely, local crystallographic changes in the vicinity of the grain boundaries, which are beyond the resolution of XRD, SEM and TEM, are responsible for this increase.

CHAPTER 7

Proton Transport in $BaZr_{0.9}Y_{0.1}O_{3-\delta}$

Neither the proton diffusion mechanism is described in details in the literature [7], nor the blocking effect of the grain boundaries is understood [30]. Based on the results from the present work, these features are discussed for BZY10 in here.

7.1 Transport of protons in a $BaZr_{0.9}Y_{0.1}O_{3-\delta}$ crystal

A mass increase is observed, when switching from dry to wet atmosphere (chapter 3-4-5). It can be (at least partially) attributed to the formation of protonic defects. Further evidence for the presence of protons into the crystal structure of BZY10 is given by the dependence of the conductivity on the oxygen and water partial pressure (chapter 3) and on the isotope effect (chapter 6). Impedance spectroscopy and quasi-elastic neutron scattering (chapter 3) indicate high proton mobility in BZY10 bulk. Concomitant high bulk conductivity is observed, leading to a proton conductivity of $2x10^{-4}$ S/cm at 300°C under wet O_2, pH_2O = 2200 Pa.

Conductivity values varying over more than 2 orders of magnitude are observed for specimens synthesised by different routes (i.e. solid-state reaction, spray drying, spray pyrolysing) (chapter 4) and containing metal ions (i.e. TiO_2, MgO, Al_2O_3, Mo and Bi_2O_3) (chapter 5). Similarly to the conductivity, the proton migration is also affected. The activation energies are found to range from below 0.4 eV to 0.8 eV. Furthermore, a variation of the lattice parameter is also observed. A striking dependence of the lattice parameter on the activation energy is found for all samples as summarized in Fig. 7-1. The larger lattice parameters correspond to the smaller activation energies.

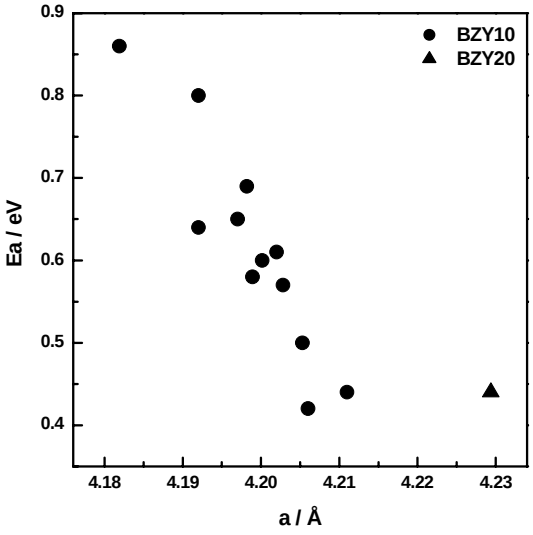

Fig. 7-1 The activation energy of the bulk conductivity is plotted as a function of the lattice parameter for the differently prepared BZY10 and for BZY20, measured under wet oxygen, pH_2O = 2200 Pa.

A possible explanation for this correlation between the activation energy and the lattice parameter is the occurrence of two polymorphs. The so-called α-phase with a low conductivity and a high activation energy has a small unit cell volume. This phase is thermodynamically stable. The so-called β-phase is the fast conducting phase with low activation energy. This phase has a larger unit cell volume and can be presumed to be metastable. Large unit cells seem to originate from a limited cross-site substitution,

which leads to restricted defect associations (chapter 4). The combined decrease in defect association and lattice expansion increases the protonic conductivity and decreases the activation energy as observed for the β-phase. A continuous change in the ratio of the α- and the β-phase leads to the observed variation of activation energy as sketched in Fig. 7-2.

A minimum for the activation energy seems to be reach at ~ 0.4 eV, since no further decrease of the activation energy is observed below 0.421 nm (chapter 3) (Fig. 7-1). Probably the increase of Y content plays a role in increasing the H-Y total interaction reducing the probability of effective jumps.

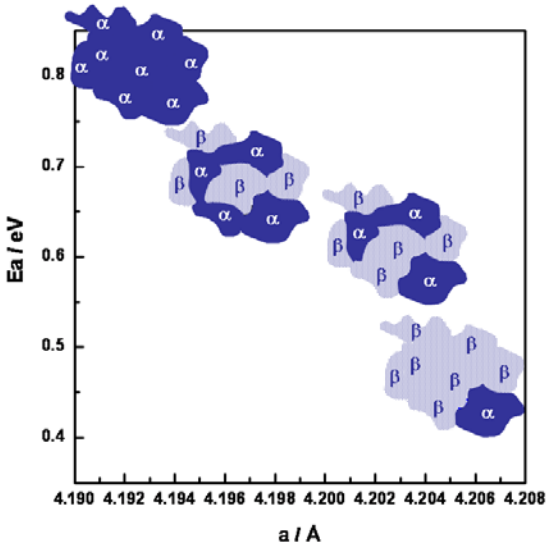

Fig. 7-2 Estimated variation of the α- and β-phases ratio depending on the lattice parameter and the activation energy.

H/D isotope exchange, QENS, and IS experiments provide data on the mechanism of proton transport across BZY10. The ratio of the conductivities under protonated and deuterated atmosphere gives values, which correspond to the mass transport of H or D charge carriers rather than to OH and OD species (chapter 6). Therefore, a vehicle mechanism, where hydroxyl groups are loosely bonded, cannot describe the charge transport across BZY10. In addition, the spectra obtained by QENS measurements (chapter 3) can be deconvoluted following a Chudley-Elliott model, which assumes a Grotthus mechanism. According to the model, the proton is the

mobile species. It moves by successive jumps along the oxygen lattice forming an activated complex as sketched in Fig. 7-3 [24]. The results from this work are in agreement with this model. A classical statistical mechanics approach cannot be followed to interpret fully the results (Chapter 6). The proton transport was rather found to obey a semi-classical theory. Quantum mechanics is required to interpret the effect according to which the zero-point energy is not at the bottom of the potential curve.

Moreover, the local diffusion evaluated by QENS was found to be very fast with a low energy barrier. The small diffusion constants obtained by QENS indicate that protons spend most of the time rotating with very low activation energy around their host oxygen ion (chapter 3). It can be sketched as in Fig. 7-4 [109]. The difference between the diffusion constants obtained by QENS and IS indicates that only rarely protons make actual jumps to the neighbouring oxygen ion.

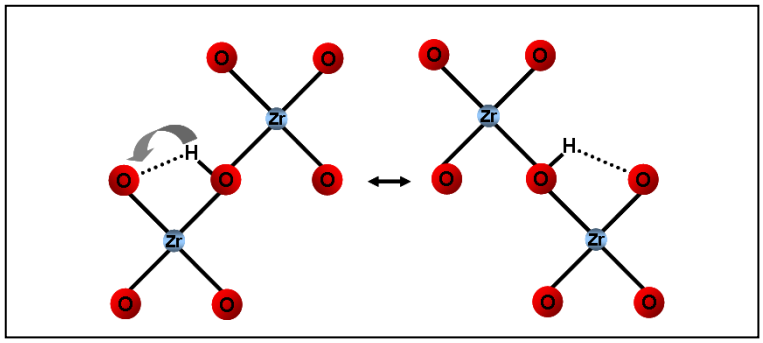

Fig. 7-3 Sketch of a Grotthus mechanism. The proton is transported through jumping from one lattice oxygen to another.

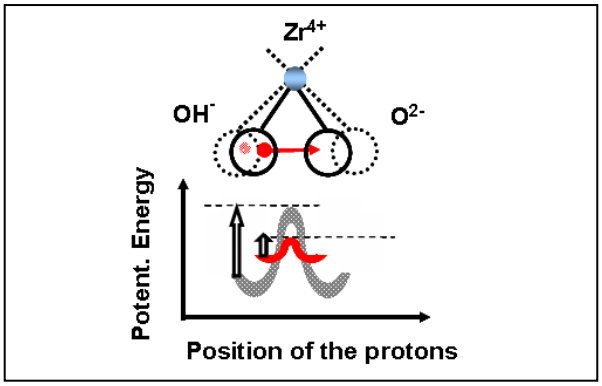

Fig. 7-4 Proton jumps are assisted by the oxygen dynamics. It decreases the potential energy for a jump.

Considering a Grotthus mechanism, the activation energies can be attributed to different interactions of the activated complex. Proton jump process cannot be viewed as a single oxygen-to-oxygen transition without taking into account the interaction with the lattice. As the proton cannot easily break the O-H bond on its own, it needs the dynamics of the host oxygen ion sublattice. The protons make only effective jumps to the neighbouring oxygen ion when the $OH^{\cdots}O$ distance is momentarily shorten as illustrated in Fig. 7-4. Big, polarisable cations and wide lattices provide powerful oxygen dynamics, while small cations and dense, stiff oxygen sublattices do not. These considerations indicate that the observed variations of the lattice parameter are in agreement with the model for a Grotthus mechanism.

7.2 Transport of protons across the grain boundaries of $BaZr_{0.9}Y_{0.1}O_{3-\delta}$

The grain boundary contribution was evaluated for the differently prepared BZY10. The grain boundaries are found to be much more resistive (> 1 order of magnitude) than the bulk and thus limiting the total conductivity. Neither the density of the grain boundaries, nor the grain boundary microstructure (chapter 4-5), nor a secondary phase in the grain boundaries (from which TEM and SEM do not give evidence in chapter 4) could explain the high grain boundary resistance.

The reduced influence of different yttrium contents under wet conditions, pH_2O = 2200 Pa, and of the partial pressure of oxygen and water dependencies on the grain boundary conductivity (chapter 3) indicates that, in conventionally sintered samples (up to 1720°C), the grain boundary conductivity is dominated by the hole transport. After annealing with an optical floating zone furnace at ~ 2200°C (chapter 6), the grain boundary conductivity increases of about 2 orders of magnitude. In addition, the grain boundary conductivity turns out to be dominated by the proton transport after additional temperature treatment.

There are several factors known to contribute to the blocking effect of the grain boundaries. In the case of materials of low purity, insulating amorphous layers of impurities filling the grain boundaries can be considered to be the main factor. This is not the case here since no insulating amorphous layer filling the grain boundaries could

be identified (chapter 3). Considering the case of high purity materials, different modes of charge transport across the grain boundaries have to be considered in order to interpret the low conductivity across the grain boundaries. First, a depletion of hydroxyl groups can occur in the space charge region (Fig. 7-5. a). In order to compensate the charge, a smaller decrease of the concentration of the hole charge carriers occurs in the space charge region. Secondly, an increase of the proton charge carrier in the space charge region could alternatively be considered (Fig. 7-5. b). In this case, the low conductivity is explained by the low mobility of proton charge carriers, the high concentration preventing from a high mobility. Finely, it should be considered that the charge carriers are purely holes, which moves along the grain boundaries (Fig. 7-5. c). However, the high grain boundary resistance excludes fast hole conduction along the grain boundaries.

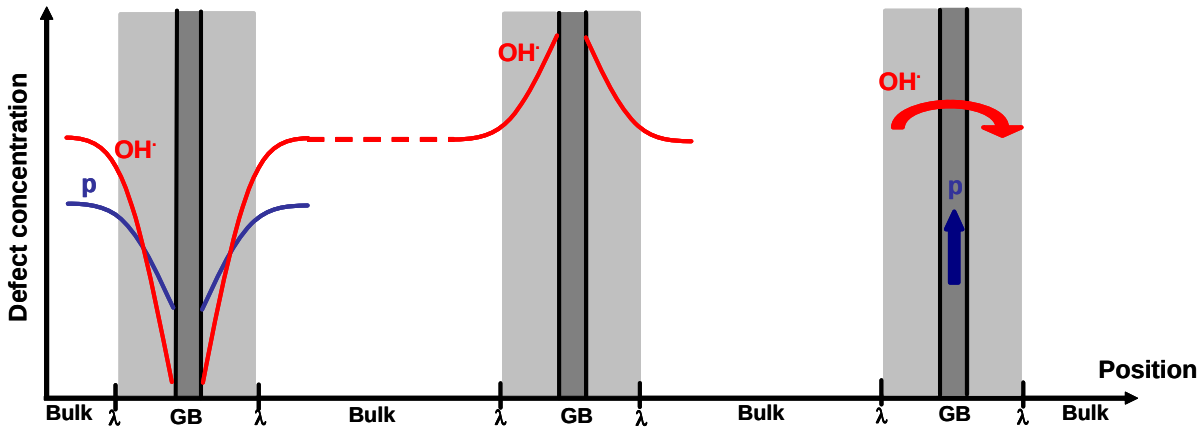

(a) (b) (c)

Fig. 7-5 Space charge model for grain boundary: charge carrier depletion in the space charge zone (a), charge carrier increase in the space charge zone (b), two pathways for conductions: ionic along the grains and electronic in the grain boundaries (c).

It is observed that the fracture behaviour changed from inter- to intra-granular cracking after annealing at high temperature (chapter 6). Additionally, an increase of the grain boundary conductivity and the change from hole to proton charge carriers occur.

Therefore, such intrinsic crystallographic failure at the grain boundaries can realistically explain the blocking effect like a Schottky barrier. Due to the change of average coordination number and bond length of the atoms in the grain boundary region compared to the regular bulk, there is an excess of free energy, which leads to accumulation or depletion of defects. Upon polarisation of the grain boundaries, a space charge layer can be built up, which might affect the concentration and the mobility of the charge carriers. Therefore, the blocking effect of the grain boundaries can be discussed towards a low mobility of protons (Fig. 7-5. b) or a low concentration of protons stemming from the space charge region (Fig. 7-5. a). The space charge layer interpretation is also consistent with the influence (however very small) of metal addition on the grain boundary conductivity (chapter 5).

CHAPTER 8

Concluding Remarks

8.1 Summary and conclusions

The aim of the thesis was to process and characterise $BaZr_{1-x}Y_xO_{3-\delta}$, an electrolyte known as a proton conductor.

First, the fabrication of BZY10 dense samples is a challenge and leads to inconsistent bulk conductivity results. A high sintering temperature (T > 1720°C) is required to sinter dense BZY10 prepared by the solid-state reaction method (chapter 3-4). Densification at lower temperature is not achieved by using neither nitrate precursors (chapter 4) nor sintering aids (chapter 5). The preparation method is found to influence not only the densification, but also the lattice parameter and the conductivity. A trend correlating the lattice parameter and the activation energy can be established. The specimens with the biggest lattice parameters have the highest conductivities and the lowest activation energies (chapter 4-5). These results can be explained by a Grotthus mechanism. Evidence from such a mechanism is given in H/D isotope exchange experiments (chapter 6) and QENS investigations (chapter 3).

Secondly, the most prominent limitation in the proton conductivity of BZY10 is clearly identified to be the grain boundaries (chapter 3). The mobile charges are most likely not protons in specimens prepared by a conventional solid-state reaction method. Instead, holes are transported across such samples (chapter 3). It was found that an exceptional thermal treatment at 2200°C leads to an improvement of the grain boundary

conductivity, which, in addition, turns out to be dominated by proton transport (chapter 6).

8.2 Outlook

In order to implement BZY10 as electrolyte into fuel cells, controlling the synthesis is technologically and scientifically challenging. The high grain boundary resistance of BZY10 has to be overcome and is still THE persisting problem. Neither the different processing routes investigated here nor the use of sintering aids lead to an improvement of the grain boundary conductivity. Only a high annealing temperature achieved by a costly time-consuming laboratory process increases the performances. The use of BZY10 as electrolyte for practical applications in fuel cells is therefore subject to new processing developments.

Alternatively, BZY10 appears to be a good material candidate for applications in sensors (classical concepts e.g. potentiometric sensors based on the Nernst potential) since a porous material i.e. a material with a low grain boundary density would be required for operation. The resistive grain boundaries could also be interesting by being sensitive to some other conditions (e.g. different atmosphere…) and allow operation as amperometric sensors.

The development of new proton conducting electrolytes for energy conversion devices remains a wide open field [110]. Investigating if and how the findings about BZY10 can help understanding the behaviour of other proton conductors and defining criteria for the selection *a priori* of compositions and structures of proton conducting electrolytes should be pursued.

8.3 Further work

Further work on BZY10 is suggested on the following topics:

- Densification of BZY10 at low temperature should be improved. Using sophisticated milling techniques can be beneficial and is an interesting approach.
- The lattice parameter was found to vary significantly depending on the calcination and sintering temperatures and on the preparation method. The present work suspected cross substitution of Y on the Ba-site. Systematic variation of the Ba content and the Zr-Y content should be followed by XRD and conductivity measurements. QENS or neutron diffusion would also be very helpful refining the structure of BZY10 and describing the site exchange equilibrium.
- QENS appears also to be a very useful tool to describe the proton mechanism. Many details are still so far unknown.
- The blocking effect of the grain boundaries was observed and could be extrinsically modified in the case of substituted ceria by Avila-Parades et al. [98]. In the present work, several additives were tentatively used. But many others can give interesting results.
- A controlled growth of thin films could also be a promising approach, which is expected to reduce the grain boundary blocking effect. Such investigations open a totally new area for investigations.
- Obtaining a specimen with one grain boundary would enable to study better the contribution of the grain boundaries. Growing two single crystals together is a possible approach.
- The performances of BZY10 operating in fuel cells have never been tested so far. It would be of main interest. Therefore, adequate electrodes have to be developed.

References

[1] H. Iwahara, T. Esaka, H. Uchida and N. Maeda, Solid State Ionics, 3-4 (1981) 359-363.

[2] W. G. Coors, J. Electrochem. Soc., 7 (2004) A994-A997.

[3] E. Traversa, Sens. Actuators B Chem., 23 **2-3** (1995) 135-156.

[4] W. G. Coors, J. Power Sources, 118 **1-2** (2003) 150-156.

[5] T. Norby, Solid State Ionics, 40-41 (1990) 857-862.

[6] N. Bonanos, Solid State Ionics, 53-56 (1992) 967-974.

[7] H. Iwahara, Solid State Ionics, 77 (1995) 289-298.

[8] L. Carrette, K. A. Friedrich and U. Stimming, Fuel Cells, 1 (2001) 5-39.

[9] P. Holtappels and U. Stimming, Handbook of Fuel Cells - Fundamentals, Technology and Applications, *Solid Oxide Fuel Cells (SOFC)*, 1 (2003) 335-354.

[10] T. Norby, Solid State Ionics, 125 (1999) 1-11.

[11] S. Stotz and C. Wagner, Ber. Bunsenges. Phys. Chem., 70 (1966) 781.

[12] D. A. Shores and R. A. Rapp, J. Electrochem. Soc., 119 (1972) 300.

[13] T. Takahashi, S. Tanase and O. Yamamoto, Electrochim. Acta, 23 **4** (1978) 369-373.

[14] S. M. Haile, Acta Mater., 51 **19** (2003) 5981-6000.

[15] W. G. Coors and D. W. Readey, J. Am. Ceram. Soc., 85 **11** (2002) 2637-2640.

[16] K. H. Ryu and S. M. Haile, Solid State Ionics, 125 (1999) 355-367.

[17] H. Iwahara, T. Yajima, T. Hibino, K. Ozaki and H. Suzuki, Solid State Ionics, 61 (1993) 65-69.

[18] A. S. Nowick and Y. Du, Solid State Ionics, 77 (1995) 137-146.

[19] H. G. Bohn, T. Schober, T. Mono and W. Schilling, Solid State Ionics, 117 **3-4** (1999) 219-228.

[20] W. Wang and A. V. Virkar, J. Electrochem. Soc., 151 **10** (2004) A1565-A1571.

[21] P. Murugaraj, K. D. Kreuer, T. He, T. Schober and J. Maier, Solid State Ionics, 98 **1-2** (1997) 1-6.

[22] N. Bonanos, Solid State Ionics, 145 (2001) 265-274.

[23] H. Iwahara, Solid State Ionics, 86-88 (1996) 9-15.

[24] K. D. Kreuer, Annu. Rev. Mater. Res., 33 (2003) 333-359.

[25] H. G. Bohn and T. Schober, J. Am. Ceram. Soc., 83 **4** (2000) 768-772.

[26] K. Katahira, Y. Kohchi, T. Shimura and H. Iwahara, Solid State Ionics, 138 **1-2** (2000) 91-98.

[27] B. Gross, J. Engeldinger, D. Grambole, F. Herrmann and R. Hempelmann, Phys. Chem. Chem. Phys., **2** (1999) 297-301.

[28] R. C. T. Slade, S. D. Flint and N. Singh, Solid State Ionics, 82 **3-4** (1995) 135-141.

[29] K.-D. Kreuer, Solid State Ionics, 125 (1999) 285-302.

[30] K.-D. Kreuer, S. Adams, W. Munch, A. Fuchs, U. Klock and J. Maier, Solid State Ionics, 145 **1-4** (2001) 295-306.

[31] F. M. M. Snijkers, A. Buekenhoudt, J. Cooymans and J. J. Luyten, Scripta Mater., 50 **5** (2004) 655-659.

[32] A. Magrez and T. Schober, Solid State Ionics, 175 (2004) 585-588.

[33] S. Valkenberg, H. G. Bohn and W. Schilling, Solid State Ionics, 97 (1997) 511-515.

[34] C. Pascual and P. Duran, J. Am. Ceram. Soc., 66 **1** (1983) 23-27.

[35] A. Ubaldini, V. Buscaglia, C. Uliana, G. Costa and M. Ferretti, J. Am. Ceram. Soc., 86 **1** (2003) 19-25.

[36] J. L. Zhang and J. E. Evetts, J. Mater. Sci., 29 (1994) 778-785.

[37] A.-M. Azad, S. Subramaniam and T. W. Dung, J. Alloy Compd., 334 **1-2** (2002) 118-130.

[38] G. L. Messing, S.-C. Zhang and G. V. Jayanthi, J. Am. Ceram. Soc., 76 **11** (1993) 2707-2726.

[39] P. Holtappels, U. Vogt and T. Graule, Adv. Eng. Mat., 7 (2005) 292.

[40] S. M. Haile and D. L. West, J. Mater. Res., 13 **6** (1998) 1576-1595.

[41] *Materials Science and Technology - A Comprehensive Treatment*, Wiley-VCH, R. J. Brook (1996).

[42] A. Sin, B. E. Montaser, P. Odier and F. Weiss, J. Am. Ceram. Soc., 85 **8** (2002) 1928-1932.

[43] P. Holtappels, U. Vogt, H. Schindler and B. Gut, *Perovskite Synthesis by Spray Pyrolysis*, Fifth European Solid Oxide Fuel Cell Forum, J. Huijsmans, Lucerne, Switzerland, 1 (2002) 103-107.

[44] E. Barsoukov and J. R. Macdonald, *Impedance Spectroscopy: Theory, Experiment, and Application*, John Wiley & Sons, 2nd edition (2005).

[45] S. Duval, LOG & SOP Probostat SOP N° 4481 (2005).

[46] Probostat, Manual Version A-4, (29 September 2004).

[47] T. Norby, Solid State Ionics, 28-30 (1988) 1586-1591.

[48] T. Norby and P. Kofstad, J. Am. Ceram. Soc., 67 **12** (1984).

[49] T. Norby and P. Kofstad, J. Am. Ceram. Soc., 69 **11** (1986) 784-789.

[50] D. P. Sutija, T. Norby and P. Bjornbom, Solid State Ionics, 77 (1995) 167-174.

[51] *Handbook of Chemistry and Physics*, CRC Press, D. R. Lide 83rd Edition (2002-2003) 6.105.

[52] N. Sammes, R. Phillips and A. Smirnova, J. Power Sources, 134 **2** (2004) 153-159.

[53] R. Haugsrud and T. Norby, Solid State Ionics, 177 **13-14** (2006) 1129-1135.

[54] B. A. Boukamp, Solid State Ionics, 169 **1-4** (2004) 65-73.

[55] S. M. Haile, J. Mater. Sci., 36 (2001) 1149-1160.

[56] R. Waser, Solid State Ionics, 75 (1995) 89-99.

[57] K. D. Kreuer, T. Dippel, Y. M. Baikov and J. Maier, Solid State Ionics, 86-88 (1996) 613-620.

[58] Y. Larring and T. Norby, Solid State Ionics, 97 **1-4** (1997) 523-528.

[59] T. Schober, Solid State Ionics, 145 **1-4** (2001) 319-324.

[60] A. Kruth and J. T. S. Irvine, Solid State Ionics, 162-163 (2003) 83-91.

[61] T. Schober and H. G. Bohn, Solid State Ionics, 127 **3-4** (2000) 351-360.

[62] T. Schober and J. Friedrich, Solid State Ionics, 125 **1-4** (1999) 319-323.

[63] F. Krug and T. Schober, Solid State Ionics, 92 **3-4** (1996) 297-302.

[64] E. Mashkina, Thesis, *Structures, Ionics Conductivity and Atomic Diffusion*, Friedrich-Alexander-Universität Erlangen-Nürnberg (2005).

[65] T. Matzke, Thesis, *Keramische Protonleiter mit Perovskitartiger Struktur*, Jülich : Forschungszentrum Jülich GmbH (1995).

[66] C. Beck, S. Janssen, B. Gro and R. Hempelmann, Scripta. Mater., 44 **8-9** (2001) 2309-2313.

[67] www.ncnr.nist.gov/dave.

[68] M. Pionke, T. Mono, W. Schweika, T. Springer and H. Schober, Solid State Ionics, 97 (1997) 497-504.

[69] C. Karmonik, R. Hempelmann, T. Matzke and T. Springer, Z. Naturforsch., 50a (1995) 539-548.

[70] A. S. Nowick, Solid State Ionics, 136-137 (2000) 1307-1314.

[71] R. D. Shannon, Acta Cryst., A32 (1976) 751-767.

[72] R. Waser and R. Hagenbeck, Acta Mater., 48 (2000) 797-825.

[73] I. Animitsa, T. Norby, S. Marion, R. Glockner and A. Neiman, Solid State Ionics, 145 **1-4** (2001) 357-364.

[74] T. Omata, K. Okuda, S. Tsugimoto and S. Otsuka-Matsuo-Yao, Solid State Ionics, 104 **3-4** (1997) 249-258.

[75] T. Schober and W. G. Coors, Solid State Ionics, 176 (2005) 357-362.

[76] K.-D. Kreuer, W. Munch, T. Ise, T. He, A. Fuchs, U. Traub and J. Maier, Ber. Bunsenges. Phys. Chem., 101 (1997) 1344-1350.

[77] T. Schober, J. Friedrich, D. Triefenbach and F. Tietz, Solid State Ionics, 100 **3-4** (1997) 173-181.

[78] H. Uchida, H. Yoshikawa and H. Iwahara, Solid State Ionics, 35 (1989) 229-234.

[79] J. E. Bauerle, J. Phys. Chem. Solids, 30 (1969) 2657-2670.

[80] K.-D. Kreuer, E. Schonherr and J. Maier, Solid State Ionics, 70-71 (1994) 278-284.

[81] P. Babilo and S. M. Haile, J. Am. Ceram. Soc., 88 **9** (2005) 2362-2368.

[82] M. S. Islam, P. R. Slater, J. R. Tolchard and T. Dinges, Dalton Trans., **19** (2004) 3061-3066.

[83] R. A. Davies, M. S. Islam and J. D. Gale, Solid State Ionics, 126 **3-4** (1999) 323-335.

[84] W. Münch, K.-D. Kreuer, G. Seifert and J. Maier, Solid State Ionics, 136-137 (2000) 183-189.

[85] W. Wang and A. V. Virkar, J. Power Sources, 142 (2005) 1-9.

[86] S.-J. Song, E. D. Wachsman, S. E. Dorris and U. Balachandran, Solid State Ionics, 149 **1-2** (2002) 1-10.

[87] R. Hempelmann, C. Karmonik, T. Matzke, M. Cappadonia, U. Stimming, T. Springer and M. A. Adams, Solid State Ionics, 77 (1995) 152-156.

[88] R. Hempelmann and C. Karmonik, Phase Trans., 58 (1996) 175-184.

[89] B. Gross, C. Beck, F. Meyer, T. Krajewski, R. Hempelmann and H. Altgeld, Solid State Ionics, 145 **1-4** (2001) 325-331.

[90] A.-M. Azad and S. Subramaniam, Mater. Res. Bull., 37 **1** (2002) 85-97.

[91] B. Guillaume, F. Boschini, I. Garcia-Cano, A. Rulmont, R. Cloots and M. Ausloos, J. Eur. Ceram. Soc., 25 **16** (2005) 3593-3604.

[92] Z. Lu, Y. Tang, L. Chen and Y. Li, J. Crys. Growth, 266 **4** (2004) 539-544.

[93] S. Maschio, A. Bachiorrini, E. Lucchini and S. Brückner, J. Eur. Ceram. Soc., 24 (2004) 2241-2246.

[94] B. Robertz, F. Boschini, R. Cloots and A. Rulmont, Int. J. Inorg. Mater., 3 **8** (2001) 1185-1187.

[95] S. J. Skinner and J. A. Kilner, Materials Today, 6 **3** (2003) 30-37.

[96] J. T. S. Irvine, University of St Andrews, personal communication (2006).

[97] A. Azad, C. Savaniu, S. Tao, S. Duval, P. Holtappels, R. M. Ibberson and J. T. S. Irvine, in preparation.

[98] H. J. Avila-Paredes and S. Kim, Solid State Ionics, 177 **35-36** (2006) 3075-3080.

[99] V. Gil, J. Tartaj, C. Moure and P. Duran, Ceram. Int., 33 **3** (2007) 471-475.

[100] T. He, K.-D. Kreuer, Y. M. Baikov and J. Maier, Solid State Ionics, 95 (1997) 301-308.

[101] S. Shin, H. H. Huang, M. Ishigame and H. Iwahara, Solid State Ionics, 40/41 (1990) 910-913.

[102] J. D. Pless, N. Erdman, D. Ko, L. D. Marks, P. C. Stair and K. R. Poeppelmeier, Crystal Growth & Design, 3 **4** (2003) 615-619.

[103] A. S. Nowick and A. V. Vaysleyb, Solid State Ionics, 97 **1-4** (1997) 17-26.

[104] R. C. T. Slade and N. Singh, J. Mater. Chem., 1 **3** (1991) 441-445.

[105] K. D. Kreuer, A. Fuchs and J. Maier, Solid State Ionics, 77 (1995) 157-162.

[106] J. F. Liu and A. S. Nowick, Solid State Ionics, 50 **1-2** (1992) 131-138.

[107] T. Scherban, Y. M. Baikov and E. K. Shalkova, Solid State Ionics, 66 **1-2** (1993) 159-164.

[108] S. Kim and J. Maier, J. Eur. Ceram. Soc., 24 (2004) 1919-1923.

[109] *Vorlesungsmanuskripte des 26. IFF-Ferienkurses vom 6. März bis 17 März 1995 im Forschungzentrum Jülich - Elektrokeramische Materialien - Grundlagen und Anwendungen*, (1995).

[110] T. Norby, Nature, 410 (2001) 877-878.